Impact Characterization of Earth Entry Vehicle for Terminal Landing on Soil

Daniel Calvert Shorts

Thesis submitted to the faculty of the Virginia Polytechnic Institute and State University in partial fulfillment of the requirements for the degree of

Master of Science
In
Mechanical Engineering

Javid Bayandor, Committee Chair
Francine Battaglia
Scott Perino

July 25th, 2017
Blacksburg, VA

Keywords: Mars Sample Return, Earth Entry Vehicle, Soil Impact, Finite Element Analysis
Impact Characterization of Earth Entry Vehicle for Terminal Landing on Soil

Impact Characterization of Earth Entry Vehicle for Terminal Landing on Soil

Daniel Calvert Shorts

Abstract

In order to more accurately predict loads subjected to the EEV (Earth Entry Vehicle) upon impact with a variety of materials, finite element simulations of soil/EEV impact were created using the program LS-DYNA. Various modeling techniques were analyzed for accuracy through comparison with physical test data when available. Through variation of numerical methods, mesh density, and material definition, an accurate and numerically efficient representation of physical data has been created. The numerical methods, Lagrangian, arbitrary Lagrangian-Eulerian (ALE), and spherical particle hydrodynamics (SPH) are compared to determine their relative accuracy in modeling soil deformation and EEV acceleration. Experimentally validated soil material parameters and element formulations were then used in parametric studies to gain a perspective on effects of EEV mass and geometry on its maximum acceleration across varying soil moisture content. Additionally, the effects of EEV orientation, velocity, and impact material were explored.

Multi-material arbitrary Lagrangian-Eulerian (MMALE) formulation possess the most effective compromise between its ability to: accurately display qualitative soil behavior, accurately recreate empirical test data, be easily utilized in parametric studies, and to maintain simulation stability. EEV acceleration can be minimized through increase of EEV mass (with constant geometry), allowing for maximum penetration depth, and longest deceleration time. A critical orientation was discovered at 30º from normal, such that maximum EEV surface area impacts the soil surface instantaneously, resulting in maximum acceleration. Off-nominal impact with concrete is predicted to increase acceleration by up to 630% from impact with soil.

Impact Characterization of Earth Entry Vehicle for Terminal Landing on Soil

Daniel Calvert Shorts

General Audience Abstract

As part of a larger effort to return Martian soil samples to Earth, the creation of a vehicle (Earth Entry Vehicle, EEV) to carry those samples from Mars, to the surface of Earth is underway. The EEV is designed to enter Earth's atmosphere and decelerate using its geometry to slow itself during descent, and the crushing of the soil to absorb impact energy upon collision with Earth. Paramount in concern is the containment of the soil samples during the EEV's impact. As part of the design process with respect to this concern, computer simulations are built in this work which are compared to collected physical test data, and used to predict impact forces on the EEV under various impact conditions. Impact conditions considered are the variation of the mass, orientation relative to vertical, geometry of the EEV, the moisture content of the soil, and the impact material. Through the testing of a variety of different numerical techniques, the optimal method for each case is determined based on the ability of each technique to accurately predict EEV acceleration, its ability to maintain computational stability during simulation, and its ease of use between various testing scenarios. It was determined through this process that more massive EEVs show a lower peak acceleration during impact due to their ability to penetrate the surface of the soil, extending the time of impact, and lowering the force applied by the soil per unit time. There was found to be a critical EEV orientation at 30º from vertical such that the largest possible surface area of the EEV impacts the soil at one instant, resulting in a large spike in acceleration upon impact. Additionally, it was predicted that more massive EEVs be made into smaller, more sharply pointed geometries and less massive EEVs use larger geometries in order to minimize peak acceleration. Impact with concrete was estimated to increase acceleration by up to 650% when compared to soil impact acceleration. This work is intended to serve as an exploratory study into the validity of various impact simulation techniques, to be used in future in higher fidelity impact models.

Acknowledgements

Thank you to my advisor, Dr. Javid Bayandor for his support and encouragement during my time at Virginia Tech, without which I would not have been able to accomplish all that I have. The same can be said of my lab mates and friends that I have made in *CRASH* Lab and at Virginia Tech, who have been invaluable, taking time from their own work to spend time with me, and help to solve some of the more difficult obstacles that I have encountered. Thank you for the generosity and kindness that you have showed me.

Thank you to Professor Francine Battaglia, Dr. Scott Perino and Dr. Jamshid Samareh for taking time from your schedules to devote time to my work, make suggestions, and offer guidance. In the case of Dr. Perino and Dr. Samareh, thank you for taking the time out of your work day to devote to the numerous conference phone calls, and for contributing an extremely valuable perspective to my work. The opportunity to intern for two summers at JPL offered to me by Dr. Perino, Dr. Bayandor, Peyman Mohasseb, and Tom Komarek has been greatly appreciated. The experience and perspective that it has given me has been transforming to my educational career. Without this opportunity, and continued support of Dr. Perino, Dr. Samareh, and JPL, my thesis would not have been possible. I must also thank Aaron Siddens and Velibor Cormarkovic for offering their time to help me when I have asked, and providing valuable advice and experience during my time at JPL.

Thank you to the Virginia Tech Physics Department for allowing me the opportunity to be a teaching assistant for the three semesters that I was at Virginia Tech. This assistantship enabled me continue my education, earn my Master's degree, and without which I would not have been able to reach my goals. It gave me new experience and skills which I hope to one day again have the chance to use in the classroom.

Finally, thank you to my family, whose love, support and inspiration over both my undergraduate, and graduate education has empowered me to continue through the hardest of times. You are very much appreciated.

Table of Contents

List of Figures

List of Tables

Nomenclature

SRC	Sample Return Capsule
EEV	Earth Entry Vehicle
MSR	Mars Sample Return
OS	Orbiting Sample
EDL	Entry Descent Landing
LaRC	Langley Research Center (NASA)
MAV	Mars Ascent Vehicle
OML	Outer Mold Line
TPS	Thermal Protection System
SIRCA	Silicone Impregnated Reusable Ceramic Ablator
UTTR	Utah Test and Training Range
MMEEV	Multi-Mission Earth Entry Vehicle
M-SAPE	Multi-Mission System Analysis for Planetary Entry
JPL	Jet Propulsion Laboratory (NASA)
ALE	Arbitrary Lagrangian-Eulerian
MMALE	Multi-Material Arbitrary Lagrangian-Eulerian
SPH	Smoothed Particle Hydrodynamics
EOS	Equation of State
CEV	Crew Exploration Vehicle

Preface

This section serves as a thesis map, outlining the content, intent, and context of each chapter.

1. Introduction

The introduction serves to introduce the reader to the concept of sample return and its history, discussing past successful and unsuccessful missions. Mars Sample Return and the various aspects involved in that specific mission are introduced as well. An outline of the launches, spacecraft, and other components involved in the sample return mission are discussed, along with a brief introduction to EEV concepts. The history of EEV design prior to the current sphere-cone design are outlined, and the evolution of EEV goals and concepts are also mentioned. This section ends in the discussion of M-SAPE and how this work will contribute to the overall M-SAPE goal.

2. Motivation

This chapter begins by declaring the objectives of this work and supports those objectives with the motivation behind them. An emphasis on the logistical advantage of this project is taken, explaining how this work, and similar projects are able to drastically improve the EEV and sample return design process for current and future missions.

3. Background

Branching from the introduction, a focus specifically on EEV design work done for the purposes of MSR is made, discussing the infancy of EEV impact testing leading to the current state of the project. The chronological evolution of EEV design and testing is explained, giving the reader a reference to the current state of the MSR EEV design stage. Past impact testing campaigns are summarized and curtailed. This chapter explains the process leading up to the current design, impact testing, and finite element modeling being done at JPL.

4. Meshing Schemes

This section briefly explains the concept of mesh density, mesh convergence and mesh dependency.

5. Element Formulations

Element formulations are outlined in three different subsections: Lagrange, ALE, and SPH. In each subsection the concept of each element formulation is explained, followed by a summary of the theory and mathematics comprised in each formulation. Visual examples are used to explain the behavior and construction of each technique. The pros and cons of each formulation are given, along an explanation of the uniqueness of each element formulation.

6. Material Models

The four main materials used in this work: fluid, soil, concrete, and EEV material (aluminum) are assigned their respective material cards and material properties. The purpose of each material, as well as the application of each material is presented. In the case of the soil materials, the parameter generation process of axial load testing is briefly outlined and explained as it relates to each required input parameter. The origins of the soil models used are mentioned, along with their applicability to the overall mission. The concrete model parameters are listed, and the origin and original purpose of the chosen concrete material. This section ends with the listing and explanation of all of the deformable materials used to model the EEV. This subsection is mainly applicable to EEVs used for the off-nominal angle impact testing as well as the concrete impact testing. The limitations and behavior of each material are summarized.

7. Model Creation

The model creation process is explained, giving the reader insight into the approach taken in each model creation and analysis stage of the project. The general process common among most finite element analysis projects; formulation selection, mesh refinement, and reduction of artificial energies and other errors characteristic of finite elements are discussed. Also in this section the geometries of the two EEVs selected for testing are shown along with their geometric parameters and basic material properties.

8. Results and Discussion

This section contains all simulation and test results, accompanied by analysis and discussion.

a. EEV-R Mass Variation

A sub-section focused on the effects of the variation of EEV mass on the peak acceleration during impact with various soils. All numerical formulations are used for modeling different soils of varying moisture content, and their results are compared. The process of mesh refinement, simulation optimization, and the limitations of each formulation are discussed when appropriate. This section is used to make conclusions about the use of the available formulations for soil modeling and how each is able to successfully and unsuccessfully model the different types of soil

b. Off-Nominal Impact Testing

The impact angles of the EEV relative to the vertical axis were varied and analyzed for their influence on the peak EEV acceleration. Two different scenarios were depicted; one when the impact velocity vector and EEV orientation were changed between trials, and another when only the EEV orientation was changed and the velocity remained in the vertical direction at a

constant initial magnitude. The acceleration effects of each case are discussed, and conclusions are made and reasoned as to the optimal EEV orientation during impact.

c. Testing of CP-300

Based upon geometric parameters provided by JPL, the CP-300 EEV is used to validate the various soil models and element formulations used in this work. An empirical data set provided by JPL is compared to the acceleration curves of the CP-300 impacting soil constructed of various element formulations.

Additionally the CP-300 is tested, similarly to the EEV-R in previous sections, through the variation of the total mass of the EEV. Using two different soils of varying moisture content, a loading window for the CP-300 is generated for use in predicting the impact acceleration at a given mass and soil saturation.

d. EEV Curvature Comparison

The loading windows of each EEV tested are compared and discussed. The similarities and differences of the peak acceleration are compared between the two geometries and the various soils used. This section draws predictions about the effects of changing EEV geometry based upon the simulation data and suggests the optimal EEV design for a given EEV mass.

e. Concrete Impact

This subsection explains the process of simulation of EEV impact with a concrete surface. The behavior of the various EEV deformable materials used is explained, with a heavy emphasis on the mesh convergence of the concrete in each case. Using the converged acceleration estimates of each of the different EEV materials, a prediction window for EEV acceleration during impact with concrete as it relates to soil impact is made.

9. Summarizing Remarks

This chapter summarizes results explained in previous sections and helps to make more relevant the conclusions already made. It goes into further discussion of the various components of each simulation and compares and contrasts the methods used. Recommendations are made based on the results, about the optimal EEV design given other experimental parameters, and conclusions or predictions previously made are further explained and supported.

10. Conclusions

The final section will briefly state the main conclusions and major results of the work. Final recommendations about each design component are offered along with the limitations of the various studies conducted. Suggestions for future or continued work are made, with the addition of areas of this work which were seen to require improvement. The applicability and contributions of the results is also noted in this section.

1. Introduction

Since the end of the 20th century there has been an effort by space agencies to launch sample return missions, which allow for a more in-depth lab analysis of planetary samples compared to on site field analysis. The 2001 Genesis Discovery Mission was designed to return solar wind samples to Earth from Lagrange Point 1. The planned recovery procedure was to utilize a two stage parachute system; an initial drogue parachute deployed at 30 *km* altitude after Earth atmosphere entry, and a main parachute to be deployed following the spacecraft's initial deceleration after Earth atmosphere entry. During an off normal axis, pitched up reentry, the capsule utilized its center of gravity to maintain orientation prior to parachute deployment. A mid-air retrieval was planned using a modified helicopter equipped with a retrieval system to gain control of the descending probe during the main parachute descent stage (Burnett *et al.*, 2003). During the Earth entry procedure, the deployment of the drogue parachute was to be initiated by an explosive which jettisoned the back plate of the craft as well as the parachute along with it. This procedure failed to occur, resulting in the parachutes not being deployed. The Genesis Sample Return Capsule (SRC), a 60-degree half-angle cone, impacted the Utah Test and Training Range (UTTR) soil without either parachute assisting in its deceleration (Perino *et al.*, 2014). A NASA failure report concluded that a failure in the G-switch avionics failed to activate the pyrotechnics sequencer, resulting in the parachutes not being deployed (Failure Review Board and Sub-team, 2005). While samples were salvageable and scientists were able to use the return material for further, more in depth research, a concern for future missions was realized based on the failed reentry of the Genesis craft. As a result alternative entry vehicles and reentry procedures were explored.

Even before the Genesis mission, work in passive entry vehicles was being performed in an effort to simplify the sample return procedure and to create a more universal device in preparation for the expected expansion of sample return missions. A 2002 NASA Langley publication argued that the elimination of active, deployable descent systems on Earth Entry Vehicles (EEVs) can drastically increase the reliability of the overall reentry system. Devices such as parachutes or airbags require transportation and storage aboard any sample return vessel. This increases total weight, decreases available space onboard, and allows for the possibility of deployment failure, as in the case of Genesis. (Kellas, 2002).

A passive EEV which relied on a crushable energy absorber to mitigate impact energy was proposed in favor of active descent devices. The absorber could be a component of the EEV itself, for landing on more rigid surfaces, or part of the impact area, most likely a soft soil. In the latter case, the EEV geometry would provide some aerodynamic drag during descent, but the majority of impact energy would be absorbed by the material into which it impacted. Such EEV designs have the potential to prevent mission failure modes similar to that of Genesis. Kellas's 2002 publication outlines the design of an omnidirectional EEV designed to withstand impact velocities of 39-42 *m/s.* This design used a crushable foam structure of approximately .315 *m* diameter (Billings, 2002). It is made of carbon foam "cells" enclosed in a stiff, deformable material to absorb impact energy, protecting the internal, spherical Orbiting Sample (OS) (Kellas, 2002). Empirical impact testing of this design performed by NASA Langley Impact Dynamics Research Facility in the early 2000's utilized a system of "hexagonal and pentagonal foam-filled cells with hybrid composite, graphite-epoxy/Kevlar cell walls" separating each cell. See Fig. 1. Four drop tests were performed at a range of 30-40 *m/s* (Billings, 2002).

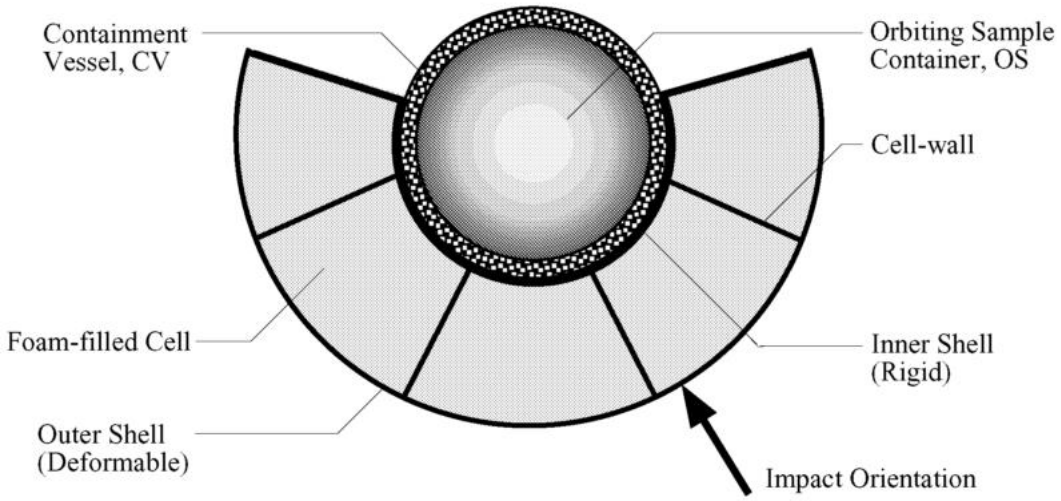

Figure 1. NASA Langley cellular sphere EEV model (Perino, Bayandor and Siddens, 2012)

A major drawback to this design is the large amount of space taken up by the energy absorbing structure, and it is designed such that the deceleration of the OS is totally reliant upon the energy absorbing structure. Alternative designs which used a reduced sized absorbing structure were pursued, resulting in a new EEV/OS design which relied on the impact area to absorb impact energy rather than only the vehicle materials. This alternate EEV design has the advantage of reducing the space required on the EEV to transport and store equipment necessary for the reentry procedure, and will be the design discussed in later sections, and analyzed in this paper.

Major concerns raised about these missions were the preservation of sample integrity. The ability to protect the samples from contamination during reentry and impact was underscored as a main safety objective. Stressed by Billings (2002b), the primary requirement of EEV design is to ensure that neither the samples or Earth atmosphere are contaminated or are allowed to interact. The concern of such a possible contamination is the transfer of Mars based pathogens to Earth, resulting in a contamination of Earth's biosphere, or the altering of the

samples in any way by the atmosphere or impact surface of Earth, thus rendering the mission results possibly obsolete. Also, contamination of the Martian samples by Earth organisms could possible cause false conclusions of discovery of Martian life (Mattingly and May, 2011). These concerns are the motivation for a simpler, more durable, and robust EEV design.

A major proposed NASA mission is the Mars Sample Return (MSR), with the objective of returning Martian soil and atmosphere to Earth. The mission is planned to involve three separate launches over the course of six years, taking advantage of the launch window every two years. The entire three launch mission layout can be seen in Fig. 2.

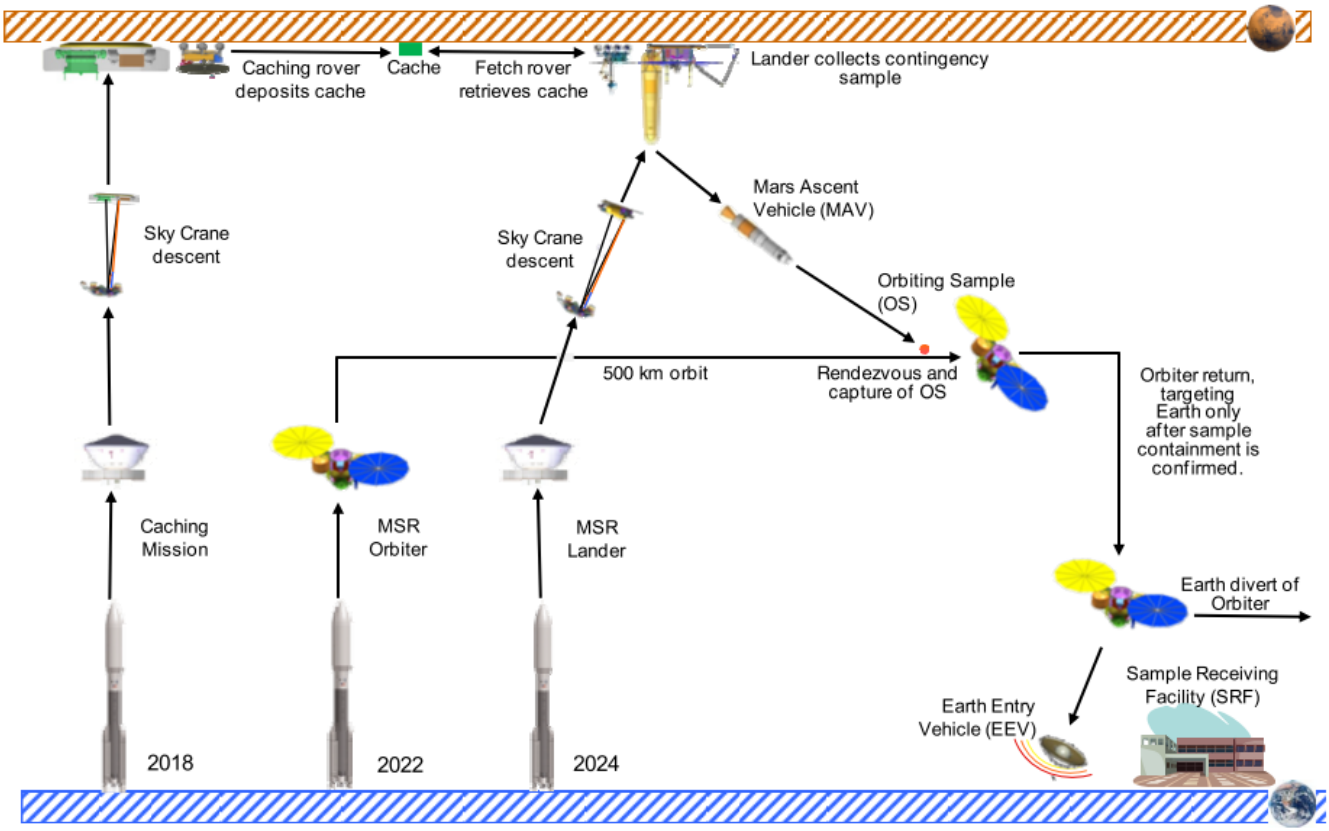

Figure 2. Mars Sample Return anticipated mission outlook

(Perino, Bayandor and Siddens, 2012)

Using the previously successful Entry, Descent and Landing (EDL) Sky Crane system, used in the Curiosity mission, a sample collection rover will be landed on the Martian surface and begin collecting soil samples which then will be cached and transferred to the Mars Ascent Vehicle (MAV). This device is sent via the third launch to Mars and will transport the samples from the Martian surface to the orbiting sample container at a 500 *km* orbit above Mars. This process can be seen in Fig. 3.

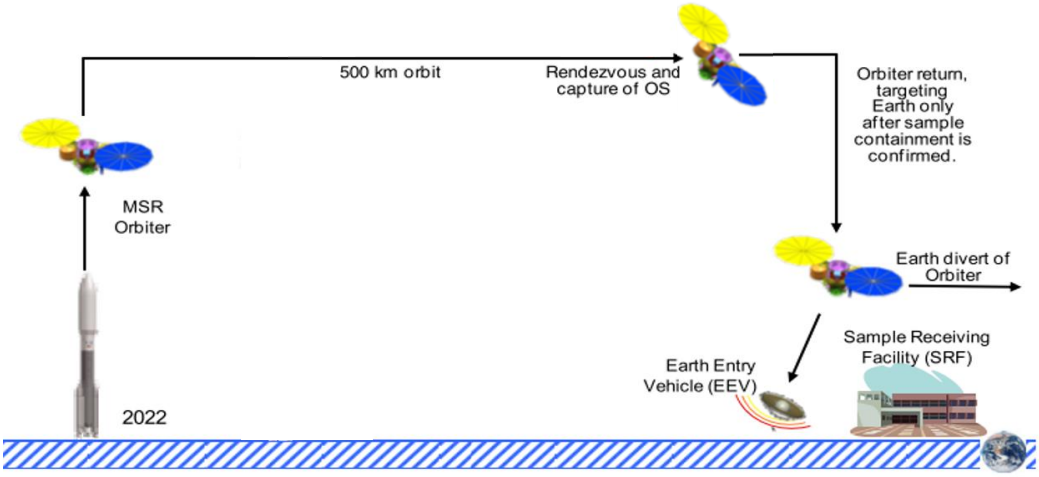

Figure 3. Orbiting Sample rendezvous with OS and Earth reentry (Perino, Bayandor and Siddens, 2012)

The Mars Orbiter, launched two Earth years prior to the launch of the MAV, performs what is known as the break-the-chain procedure on the OS. This process ensures all components which were in contact with the Martian atmosphere are safely contained for transport. The area where the OS will be contained is sterilized and sealed prior to mission start, as well as all mission components in contact with the Martian samples. This ensures the OS and its samples are not contaminated. Combined with an EEV, the MSR Orbiter is then directed on a non-impact trajectory with Earth. Once the EEV/OS is ensured to be successfully transported and has remained contained, it detaches from the MSR Orbiter and enters Earth's atmosphere. The MSR

Orbiter is then discarded, away from Earth orbit (Mattingly and May, 2011). Using a "parachute-less self-righting system" the EEV/OS will perform a high velocity, hard-impact landing in a predetermined area (Squyres *et al.*, 2011). Upon landing, a recovery team will transfer the EEV to a secure quarantine area at the Sample Receiving Facility (SRF). The returned sample will contain approximately 500 *g* of material consisting of anywhere between 19 and 37 rock core samples, at least one regolith sample, and a pressured atmosphere sample (Mattingly and May, 2011).

The standard EEV design for MSR carries and surrounds the OS with an energy absorbing impact sphere of a cellular structure. This is encased by a heat shield, an outer mold line (OML) and concave back shell, all surrounded by thermal protection systems (TPS). TPS on the front of the EEV is a fully dense carbon phenolic, and an acusil and silicone impregnated reusable ceramic ablator (SIRCA) is used for TPS on the back shell. The heat shield and OML form a rounded, conical shape with a slope of 60° from the vertical, meant to maintain correct reentry orientation during hypersonic velocities in atmosphere. During off-nominal EEV orientations due to foreign object impact or system failure during the entry procedure, the geometry of the EEV is designed to maintain vehicle orientation integrity during a tumbling, or 180° orientation offset. The internal structure of the EEV is designed to survive launch and entry loads and to serve as an aerodynamic decelerator, whereas the OS is meant to protect against sample contamination during impact loading (Samareh, Maddock and Winski, 2012).

The nominal landing site for the EEV is the UTTR, a 19,000 mi^2 region known to have large areas of soft, moist soil. The advantage of such a landing zone is that the need for energy absorbing material on the EEV itself is reduced, as much of the impact energy is predicted to be absorbed by the soil, rather than the structure of the EEV. This reduces the need for an EEV

design with large, energy absorbing foam cells, allowing it to be of a much simpler design, as seen in Fig. 4**.**

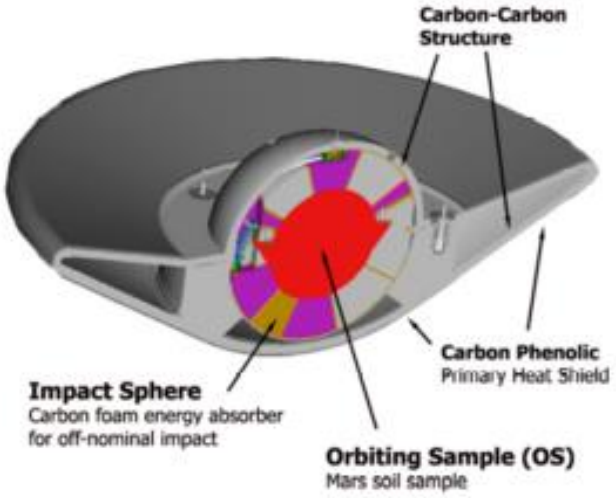

Figure 4. Proposed MSR EEV Design (Samareh, Maddock and Winski, 2012)

The UTTR area is not without faults however as there is still a possibility of the EEV to impact with various obstacles such as the rocks, roads and other hard objects or surfaces present in the region (Billings, 2002). This possibility demands that any off-nominal impact case of the EEV be explored and designed for, since in such an event the integrity of the samples, and the containment assurance be maintained.

A larger effort, which is based on the design of the MSR EEV, is the Multi-Mission System Analysis for Planetary Entry (M-SAPE) program. This work provides a framework for the rapid design of EEVs for the purpose of performing multiple sample return missions across numerous mission scenarios utilizing a Multi-Mission Earth Entry Vehicle (MMEEV). It allows for the variation of design geometry and mass and has laid forth a method for impact analysis, structural analysis, flight mechanics and acceleration, and load prediction methods. As with the

MSR EEV design, M-SAPE focuses on the minimization of risk of sample contamination through the use of passive descent methods and utilizes a common design concept for any sample return vehicle. The methods which it provides will avoid costly design and test work which would be required when creating unique vehicles for each of the anticipated sample return missions in the future. Allowing for the rapid creation of an initial low fidelity design and gradually increasing model intricacy and application of mission specific necessities, the M-SAPE method utilizes widely available software, such and Python and Java, and open source programs whenever available, in order to increase accessibility for all research programs and teams. It is designed such that engineers are able to quickly gain valuable information on a proposed design early in the design process in order to improve mission efficiency and cost effectiveness (Samareh *et al.*, 2014). See Fig. 5 for visual of mission design progression with M-SAPE.

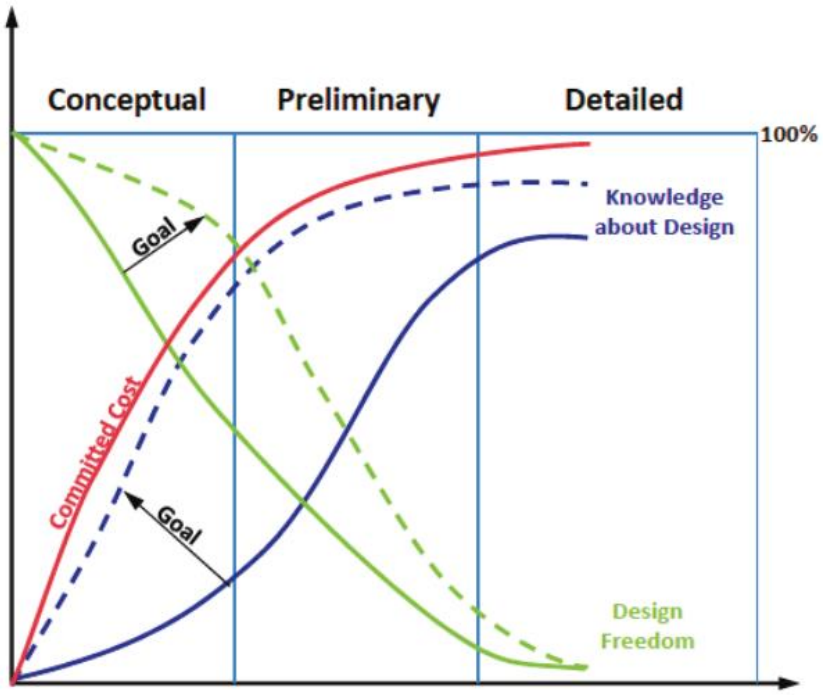

Figure 5. M-SAPE Framework Design Progression (Samareh *et al.*, 2014)

The work discussed in this thesis will aid in the overall M-SAPE objective of the creation of a sample return mission design process by providing a method and pathway for Earth impact analysis. Through the testing of low resolution models, the effects of multiple impact materials, EEV orientation scenarios, and the gradual process of increasing the intricacy of those models, an additional component of M-SAPE will be offered.

2. Motivation

The objective of this project is to create realistic EEV impact models using a variety of element formulations, meshing schemes, and impact material models to predict the maximum acceleration of EEVs during impact with soil. The outcome of these simulations can be used in the design and optimization of both the EEV and the OS for their application in the Earth impact stage of the MSR mission. The ability to quickly and inexpensively predict loads on the EEV during impact with different ground materials greatly broadens the capabilities of the MSR project. Empirical impact tests require significant preparation time and cost to perform, and all possible mission impact scenarios cannot be performed in this manner. Therefore, using a validated modeling approach can significantly facilitate the testing of relevant case studies. Finite element models are validated against empirical data to allow for a full parametric study of EEV landing events through a verified and reliable methodology. Testing efficiency can also drastically benefit from finite element models in instances where off-nominal impact conditions are prevalent; for example when the EEV impacts at an extreme orientation relative to the ground, or strikes hard objects such as rock or concrete. Simulations allow the user the control to designate specific initial or other experimental conditions with as precision that empirical testing does not allow. If such scenarios were performed empirically, available pitch control provided by the test apparatus, or lack thereof, of the EEV would increase the difficultly of accurately

varying the impact angles across test cases. Additionally, the possibility of extreme damage to the test article during impacts with hard surfaces has the potential to greatly increase the cost and man hours involved in preparing and performing testing. Building on existing impact test data and existing finite element models of the current MSR EEV, this work creates a database and methodology of modeling and model creation from which a large variety of impact scenarios can quickly and reliably be predicted.

3. Background

The process of collecting impact data of different EEV designs has been underway since as early as 1998 during a series of drop tests of 250 *mm* hemispherical penetrometers in the UTTR by engineers from NASA Langley Research Center (LaRC). Their goal was create an eventual EEV design which relied totally on a passive entry and deceleration methods for Earth reentry, doing away with the use of previous active descent techniques. These hollow penetrometers, seen in Fig. 6, were made of Bakelite reinforced spun aluminum shells and were dropped from a predetermined height using a hot-air balloon and helicopter.

Figure 6. Hemispherical penetrometer used during the 1998 and 2000 drop test campaigns (Kellas, 2016)

Due to the rudimentary test conditions, and unreliable drop method, limited data was obtained from this series of testing. However the results proved the relation, $A_{peak} \propto \frac{DV^2}{M}$, such that the peak acceleration is proportional to the EEV nose diameter times the square of the impact velocity divided by the EEV mass. This relation is used as the basis for subsequent test campaigns. While the goal of these tests was to generate information to be transitioned into a finite element software, limited success was had, and effective progress on this project slowed in the years to come (Kellas, 2016).

Significant work has been performed regarding the base design for the EEV/OS which has included an automated EEV geometry generating tool. Built by Perino *et al.* (2014), this program was designed to rapidly construct and determine optimal EEV geometry, and mesh the subsequently created geometry, for use in finite element simulation. Considered designs are shown in Fig. 7.

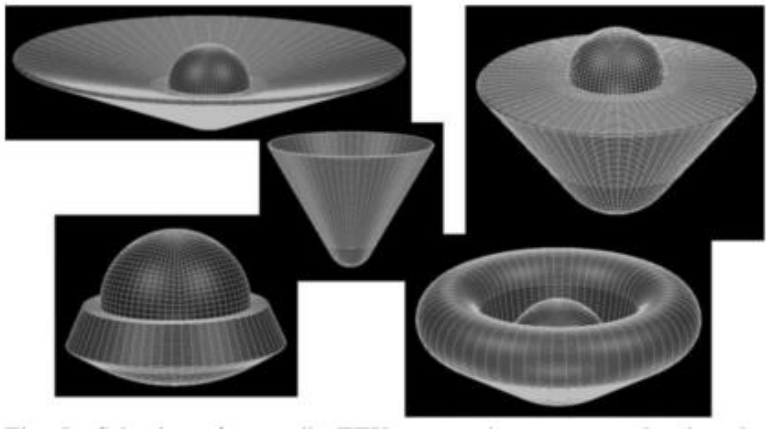

Figure 7. Possible EEV geometries generated by Perino et al., (2014)

The work done by Perino *et al.*, (2014) has allowed for clearer picture as the loading and vibration effects of changing EEV geometry, TPS density, material elastic modulus and various other design variables. Parametric studies were performed to determine the reliance of mass, the

stress induced by static loading, and vibration response on EEV geometric and material variables. Random acoustic loading was applied to a three-point constrained EEV model such that the induced stresses could be analyzed in addition to the various static loading cases associated with launch and reentry. Results from this work produced a methodology for dynamic structural analysis and the capability for rapid automated EEV geometry and material parametric study. This work shows a major contribution to the M-SAPE framework by creating an efficient methodology for EEV design and construction, and contributed to the eventual finalized EEV geometry, which will be used in later works. A limitation of this work however is that there was no ability to successfully validate its results against mission scenario impacts, and the loading results generated were a result of a static applied pressure distribution. Such loading behavior is not necessarily the same as would be experienced during soil impact. No validated soil models existed at the time which were able to successfully corroborate with the conclusions given in this project. Therefore, it was vital to the MSR mission at the time to determine the actual loading characteristics of the chosen EEV design, and how, if at all, the loading behavior would change under soil impact conditions.

EEV drop testing was revitalized in 2016, again by LaRC, testing the more recognizable conical EEV design, see Fig. 8, in UTTR with the objective of demonstrating the feasibility of such a design in sample containment, peak acceleration measurement, and its ability to interface with finite element simulation.

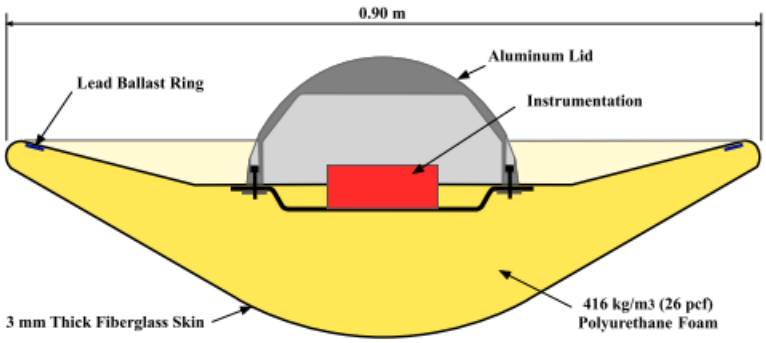

Figure 8. EEV design used by LaRC during 2016 drop test campaign (Kellas, 2016)

During this test campaign two non-crushable 1.2 *m* diameter EEVs were designed to impact soft soil, using the soil's deformation to absorb impact energy. During the design process at LaRC a peak load limit was assigned to the EEV design of 1500 *G*, a value dictated by the ability of soil samples to maintain their scientific value under loading. The EEVs were dropped from a height of 400 *m* from a helicopter, reaching near their terminal velocity, and predicted to land within a 60 *m* predetermined impact area. Reliable results were limited to a single data set due to strong winds in the area and unintentional release of the EEV from height during testing (Kellas, 2016). While conclusions regarding the predictability of EEV peak acceleration were made based on the results of this test, it relied on a single data set for this conclusion, and further investigation into the predictability of peak EEV acceleration must be made.

Continuing the EEV impact test campaigns, NASA Jet Propulsion Laboratory (JPL) has recently performed numerous impact tests of passive, conical EEV designs with soils of various water content. The aim of these tests is to gain the ability to accurately represent a range of soil conditions at the UTTR through the validation of finite element models using the generated impact data. Currently, impact test data has been used to create a series of finite element simulations which have been proven to replicate the results of physical experimentation to an acceptable degree of accuracy. The motivation for further model creation is to optimize these

simulations, to more closely capture the physics of the impacts, and to increase their reliability through the continued testing of various numerical methods such as Arbitrary Lagrangian-Eulerian (ALE), and Smoothed Particle Hydrodynamics (SPH) techniques. Additionally, alternate material parameters generated from test data gathered under varying soil type and water content, as well as different mesh geometries, were tested to determine the influence they have on EEV peak acceleration, soil deformation and behavior of the element formulation. These simulations were then analyzed to assess their sensitivities to impact conditions, hence determining their suitability to predict particular physical tests with realistic material deformation. The range of simulations were steadily increased in level of detail and type of impact surface materials considered, in order to build a larger archive of EEV landing scenarios.

Empirical test data collection during this campaign utilized an approximately 7 story metal frame tower and compressed air cable and pulley system to accelerate a sample EEV to terminal velocity within an extremely short time, seen in Fig. 9.

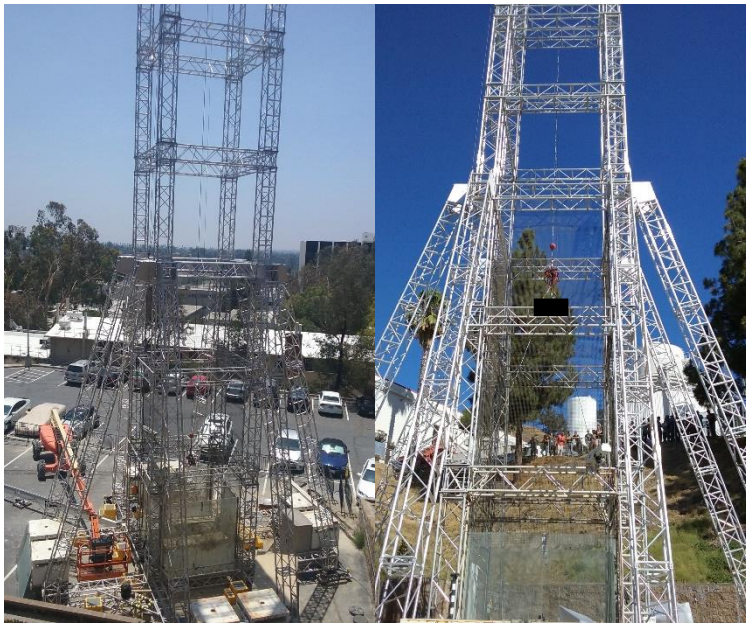

Figure 9. JPL EEV testing impact tower

Once accelerated, the EEV was released and impacted into a sample of soil taken from the Rosamond dry lake bed in Rosamond, CA. This more controlled test environment allowed for significantly larger numbers of data sets to be collected and utilized. Using attached accelerometers, and high speed video of the impact, the results of these tests were then used to validate the constructed finite element models and their ability to predict peak impact acceleration of the EEV. Once validated, the impact models will then be converted to model the UTTR soil, and progressively higher fidelity EEV models will be input and be tested. This process will ensure that the many errors associated with previous impact testing can be avoided, and a lower cost, higher efficiency methodology will be used in load prediction. Additionally, the use of validated finite element simulation in place of impact testing allows for the precise control of initial conditions such as impact velocity, EEV orientation and soil conditions. The work in this paper is stemmed from the methodologies used at JPL, and uses one of the impact tower data sets to validate the soil models and numerical techniques used.

4. Meshing Schemes

As part of each developed numerical method, meshing densities were varied to determine the effects of such variation on the predicted acceleration curve of the EEV. As a characteristic of finite elements, coarse mesh generally results in an overly stiff material which in turn results in less realistic deformation of that material. Mesh refinement studies were therefore conducted on each new mesh geometry and for each new element formation to construct a spectrum of results correlated to mesh densities and arrive at a result to which the refined meshes converged. This spectrum of results gives information on the relationship of mesh refinement level and the accuracies of the results of the simulation. Using this information, a pattern of convergence is observed as the mesh refinement process progresses and the mesh density is increased. This

procedure is meant to determine a mesh density such that the results of the simulation asymptotically approach what is the most accurate behavior, as the changing mesh density approaches the a critical value.

5. Element Formulations

5.1 Lagrange Formation

The Lagrangian formulation as explained by Kim *et al.*, (2011), is a finite element method typically used for solid mechanics simulation. Scenarios where relatively low material deformation, particularly minimal compressive strain, are expected are instances where Lagrangian elements are most effective. The Lagrangian formulation involves a single, translatable and deformable mesh for each material which moves in conjunction with the deformation of the material, or part, to which it is assigned. Each Lagrangian mesh consists only of its initial material for the duration of the simulation, meaning that any mesh in the simulation can only contain its original material and part. See Fig. 10.

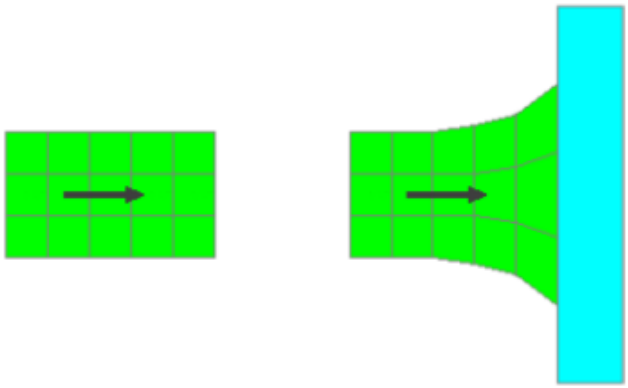

Figure 10. Lagrangian formulation consists of a material/part tied, deformable mesh which carries position information (Siddens *et al.*, 2012)

During large deformations, Lagrangian elements have the tendency to lose accuracy as their aspect ratio is increasingly distorted, resulting in a decreasing time step approaching zero (Do and Day, 2005). Kim *et al.*, (2011) adds that Lagrangian elements can undergo large element distortion, and as a result experience element entanglement which then often leads to negative volume and termination errors during simulation. These characteristics can cause severe stability issues when modeling easily deformable materials such as soft soil or non-viscous fluids due to their high strain response to loading. Using these materials will often cause failure of the simulation when the computed time step becomes too low to continue calculation, or elements deform to a negative volume.

During the modeling of the Lagrangian soil, one point integration elements were used in order to decrease computational time, as well as to avoid the overly large distortion of the element during deformation. This is something that can commonly occur when using a fully integrated solid element. In order to further reduce the artificial energy creation in the elements, known as hourglassing, an energy control card was used, *Control_Energy. Hourglassing refers to a zero energy mode, orthogonal to the strain the element, which can develop in elements during large deformation. It can result in the failure, or inaccuracy of a simulation through the creation of artificial energy. Hourglass modes are seen in Fig.11.

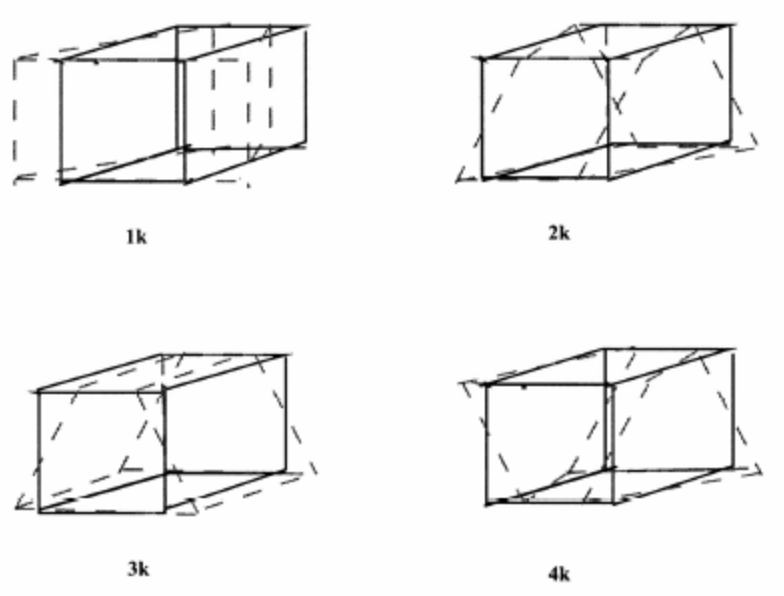

Figure 11. Examples of hourglassing in an eight node, single integration point element (Hallquist, 2006)

The *Control_Energy card in LS-Dyna instructs the simulation to compute and include the hourglassing energy into the energy balance of the system, allowing for the monitoring of the extent to which elements creating artificial energy. Additionally, this card monitors the energy dissipation and including it in the energy distribution. This card allows for the energy of the system to include the hourglass energy, and helps the simulation to consider the effects of hourglassing in its calculations (LS-Dyna, 2007).

5.2 Arbitrary Lagrangian-Eulerian

Arbitrary Lagrangian-Eulerian (ALE) is a combination of Eulerian and Lagrangian formulations and is typically reserved for modeling fluids and their interactions with solid materials, or fluid like behavior of non-viscous material. Models have the potential to involve interaction between multiple fluids and non-fluid parts. Unlike in pure Lagrangian formulations where material mesh is the same as the positional mesh, ALE uses two separate meshes. A

translatable, non-deformable background mesh, referred to as an ALE mesh, is initially created to contain the different materials in the simulation. Within this ALE mesh, there is a virtual mesh attached to the material or materials as they propagate through the fixed ALE mesh. These meshes can consist of a series of Lagrangian meshes which deform along with the deformation of each material, surrounded by a global Eulerian mesh. While the Eulerian mesh is able to move through space, it remains un-deformed as Lagrangian meshes flow through it. See Fig. 12 for a visualization of the ALE construction.

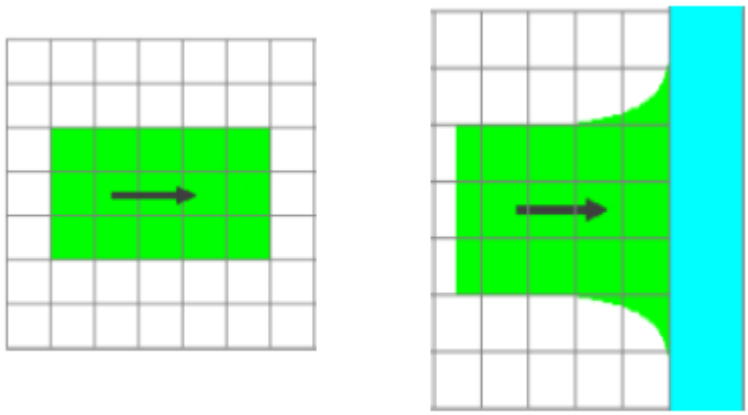

Figure 12. ALE formulation consists of a translatable, non-deformable control volume containing position information and material mesh showing deformation (Siddens *et al.*, 2012)

During distortion of the Lagrangian materials, deformation is calculated in the same manner as in pure Lagrangian formulations. The element state variables are subsequently remapped to relate their deformation to the background ALE mesh as each material contorts. This second step, advection step, is where element state variables are calculated using the "conservations of mass, momentum and energy together with material constitutive equations" (Do and Day, 2005). It is important to note that Eulerian meshes are very similar to ALE in that

they were designed for use modeling large deformation and fluid flow and consist of a non-deformable global volumetric mesh. The central difference is that ALE global mesh, while non-deformable as is Eulerian, is translatable in space. Eulerian mesh allows for material to flow through it, easing the possibility of mesh distortion but as a result, does not retain displacement data for each element, just the volume fraction of material in each Eulerian element, as explained by Kim *et al.*, (2011). This trait requires a large, refined mesh which as a result demands a significant computational expense and lends itself to being inferior to ALE which doesn't share this downside. For the purposes of this work, the background ALE mesh is not required to translate through space and thus behaves up to the same capabilities as an Eulerian background mesh would, but ALE was chosen because of its extensive reputation as a more reliable formulation as compared to Eulerian. Generally, ALE formulations show less element distortion with larger material deformation than in pure Lagrangian, making ALE more effective at modeling less stiff, more fluidic materials (Do and Day, 2005). When modeling fluidic materials using the Lagrangian formulation there is a tendency, depending of the element size and geometry and material viscosity, for elements to over deform into their adjacent elements, resulting in a negative volume element and inaccurate deformation mechanics.

The process of generating a single material ALE model and a multi-material ALE (MMALE) model are significantly different. When generating single material ALE models two separate parts are created, one from the desired impact material, and the other is set as a void for the material to deform into. The choice of using a void area above the impact material as opposed to air was made to avoid numerical errors which often occur when assigning the entire ALE mesh a material, as suggested by Kim *et al.*, (2011). Generating a MMALE model, a single meshed part is created and then partitioned into the initial volumes of the various materials used.

This process ensures that while each of the different materials deforms, the background reference mesh is a single construct such that any of the MMALE materials are able to flow into any part of the background Eulerian/ALE mesh.

In order to model the interaction of a solid or shell Lagrangian part with ALE or MMALE, a coupling constraint must be created which is a different formulation than generic surface to surface contact used in Lagrangian only interactions. During the interaction of Lagrangian and ALE materials, LS-Dyna uses the intersections between the two materials to determine when contact has occurred. Using the volume fraction of ALE which has penetrated the Lagrangian part during a single time step, the resulting penetration distance of ALE into the Lagrangian part is found at each element, and coupling forces between the two materials are determined. Using the magnitude of these coupling forces, the resultant forces on each of the materials is determined. LS-Dyna then re-distributes the ALE and Lagrangian elements and applies the determined coupling forces such that a realistic contact occurs (Do and Day, 2005). This process continues over all time steps that the ALE and Lagrange parts are influencing each other, adjusting accordingly for penetration after each iteration.

Depending of the conditions of the simulation, such a mesh size and geometry, impact velocities, etc. different variations on the *Constrained_Lagrange_in_Solid formulation are utilized on a case by case basis to prevent the over penetration of the ALE into the Lagrangian part. This process provides a much more conservative approximation for interaction between the Lagrangian and ALE parts by calculating the penalty forces between the two element formulations and adding an extra force referred to as the leakage control force. While this setting will result in an over prediction of the material deformation, it will aid in the prevention of

element over penetration which can potentially result in far more inaccurate acceleration curves for the EEV.

When using MMALE and varying density within the initial background MMALE mesh, LS-Dyna approximates the boundary between MMALE materials with different density by creating a density gradient through the boundary area. This is a byproduct of creating a single MMALE part and partitioning it to form varying materials and varying densities. A visualization of this approximation can be seen in Fig. 13.

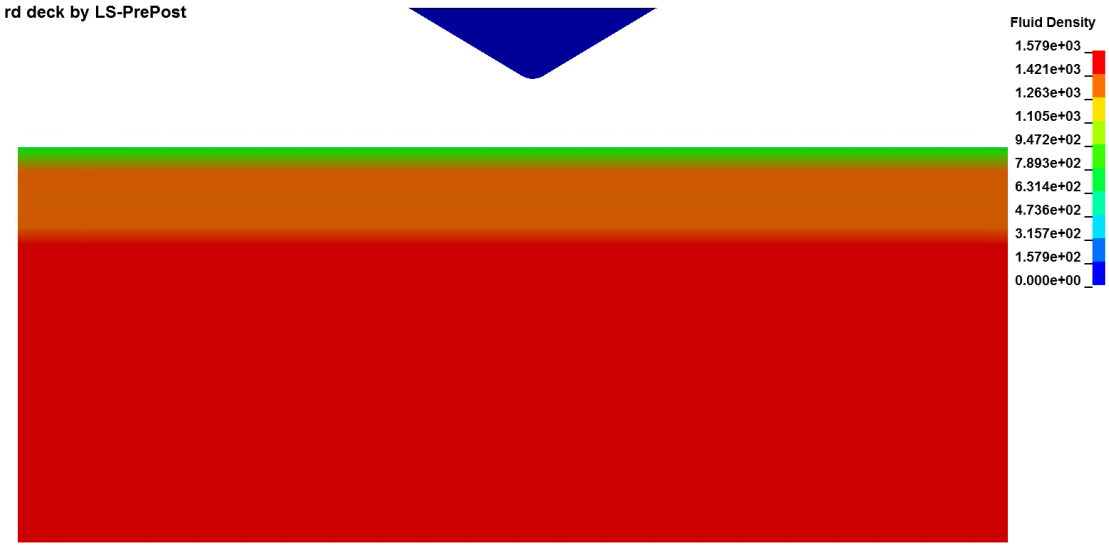

Figure 13. MMALE approximates changes in density (*kg/m^3*) between materials

Despite having a surface soil density of 1378 *kg/m^3* and sub-surface soil density of 1578 *kg/m^3*, LS-Dyna cannot transition the material boundaries without a density gradient. This numerical concept is important to consider when evaluating the changes in density and compression of soil as the EEV penetrates. This density gradient is unique to MMALE, and an immediate density change through the soil is made when using both the Lagrangian and SPH formulations. For this reason MMALE is slightly more realistic as such immediate density

changes are not how the soil is in reality. The soil density change with depth is already being approximated by only using two different soil density values, and having the ability to produce a small soil density gradient by default when using MMALE, increases the realism of the model slightly. The scale in Fig.13 reads as fluid density because this is the syntax used by LS-Dyna when describing the density of ALE parts, and is therefore not limited to fluidic materials only, although MMALE is commonly used model such materials.

5.3 Smoothed Particle Hydrodynamics

According to Horton *et al.*, (2017), smoothed particle hydrodynamics (SPH) is a mesh-free, Lagrangian, continuum method which uses volumeless spherical particles rather than polygonal, interconnected elements. Originally created for the modeling of the physics of galaxy evolution, it has gained use and reputability in the field of fluid mechanics. It excels at impact or penetration simulations as well as showing the behavior of fluid flows, both compressible and incompressible, due to its stability while exhibiting large material deformation. The arbitrariness of the particle distribution and lack of connectivity between particles allows for a more realistic deformation of granular and fluid materials as it allows for adjacent particles to separate and diverge from one another. Additionally, Kim *et al.*, (2011) points out that this characteristic also eliminates element hourglassing effects which can alter results in mesh based formulations. This negates many of the element instabilities that conventional Lagrangian meshes and occasionally ALE, show in larger distortion due to element connectivity. SPH is known to be computationally efficient and capable of showing higher accuracy than other element formulations when applied correctly (Vesenjak and Ren, 2009; Guo, 2010). Vesenjak and Ren (2009) explain that it has the potential to reduce or eliminate mesh biasing in material behavior,

mainly as it affects deformation, due to its mesh-free construction. Horton *et al.*, (2017) elaborates that in SPH, the continuum, **Ω**, is discretized by the many SPH particles, each containing nodal information, where each i^{th} particle is related to adjacent particles, *j*, of varying distance such that the conservation equations for density and momentum are obeyed.

$$\frac{\partial \rho_i}{\partial t} = \rho_i \sum_{j=1}^{N} \frac{m_j}{\rho_j} \mathbf{V}_{ij} \frac{\partial W_{ij}}{\partial x_i}$$

$$\frac{\partial \mathbf{V}_i}{\partial t} = -\sum_{j=1}^{N} m_j \left(\frac{S_i}{\rho_i^2} + \frac{S_j}{\rho_j^2} + \Pi_{ij} \right) \frac{\partial W_{ij}}{\partial x_i}$$

The sphere and intensity of influence of each particle based on its calculated smoothing length, *h,* and kernel function, *W,* visualized in Fig. 14

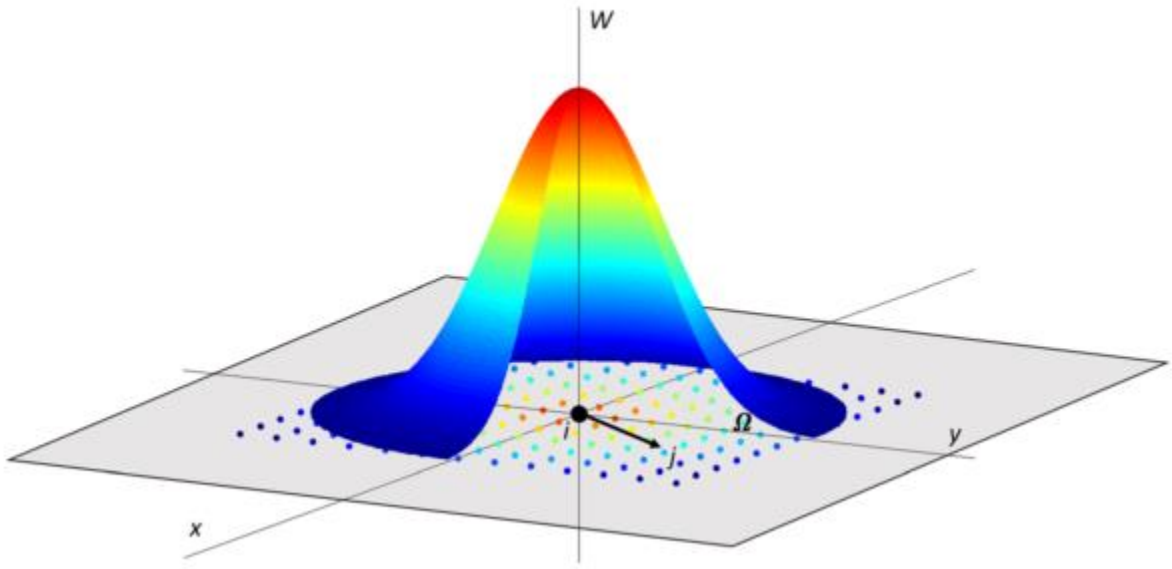

Figure 14. Visualization of SPH smoothing length, *h*, and kernel function, *W*, where red indicates a larger influence effectiveness. (Horton *et al.*, 2017)

Using this weighted sphere of influence, adjacent particles interact with one another based upon their proximity and relative strength of their kernel function, *W,* as seen in Fig. 15.

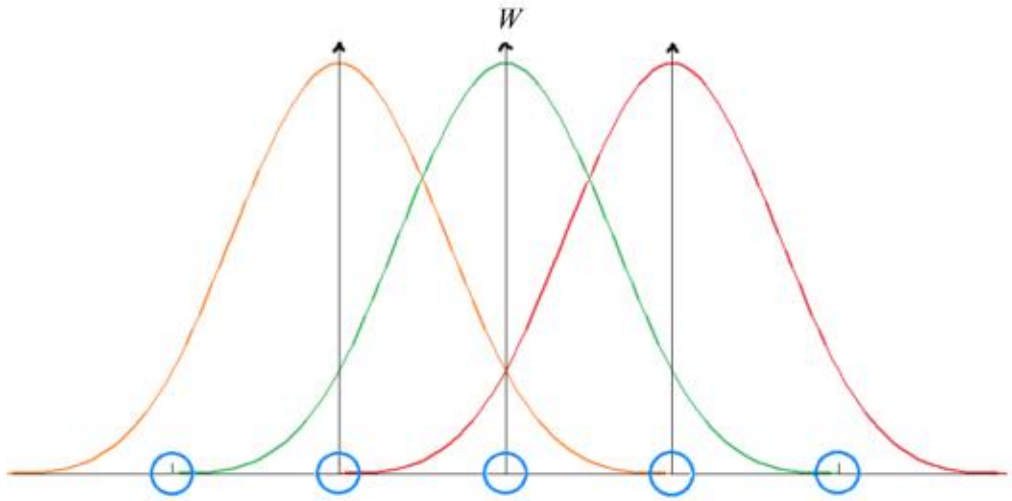

Figure 15. Depiction of smoothing length interaction between SPH particles (Gretsch *et al.*, 2012)

As provided by the LS-Dyna theory manual, the kernel function is defined as

$$W(\mathbf{x},h)=\frac{1}{h(\mathbf{x})^{d}}\theta(\mathbf{x})$$

where d is the number of spatial dimensions and W is expected to be centrally peaked. Using the cubic B-spline kernel function, θ(x) is defined as

$$\theta(u)=C\times\begin{cases}1-\frac{3}{2}u^{2}+\frac{3}{4}u^{3} & \text{for } /u/\le 1\\ \frac{1}{4}(2-u)^{3} & \text{for } 1\le /u/\le 2\\ 0 & \text{for } 2< /u/\end{cases}$$

where C is a constant of normalization dependent on the number of spatial dimensions and u is a normalized distance from the particle, as shown in Fig. 16.

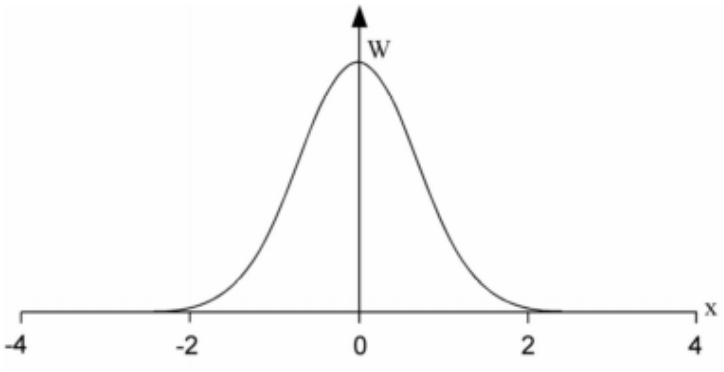

Figure 16. Normalization of distance from particle for use in B-spline kernel function (Hallquist, 2006)

Using these formulations a particle approximation function is created such that

$$\Pi^h f(\mathbf{x}_i) = \sum_{j=1}^{N} w_j f(\mathbf{x}_i) W(\mathbf{x}_i - \mathbf{x}_j, h)$$

and the "weight" of the particle is defined as the mass over density such that

$$w_j = \frac{m_j}{\rho_j}$$

Due to this arduous calculation process of neighbor searching, particularly in dense SPH fields, computational time can drastically increase as each particle must search its own influence sphere and then determine interaction with each of the found SPH particles within that sphere. Particles interact with one another based on their proximity to all adjacent particles within their sphere of influence, 2*h*, where the magnitude of that influence is based on the kernel function such that the closer two particles are, the larger the influence those two particles have on each other. In order to determine particles which are within a particle's sphere of influence, the SPH formulation performs a neighbor search during each iteration, for each particle. This process can become computationally expensive when using large numbers of SPH particles as the time step

also is a function of the smoothing length of each particle, increasing with increased smoothing length. Therefore during simulations with significant particle interaction and density, there is a laborious calculation process for each time step. To reduce this computational time, the bucket sort method is used, where space is broken into squares or cubes, depending of the number of dimensions used, and only the cube containing the particle in question and all adjacent cubes are analyzed for particle influences. See Fig. 17.

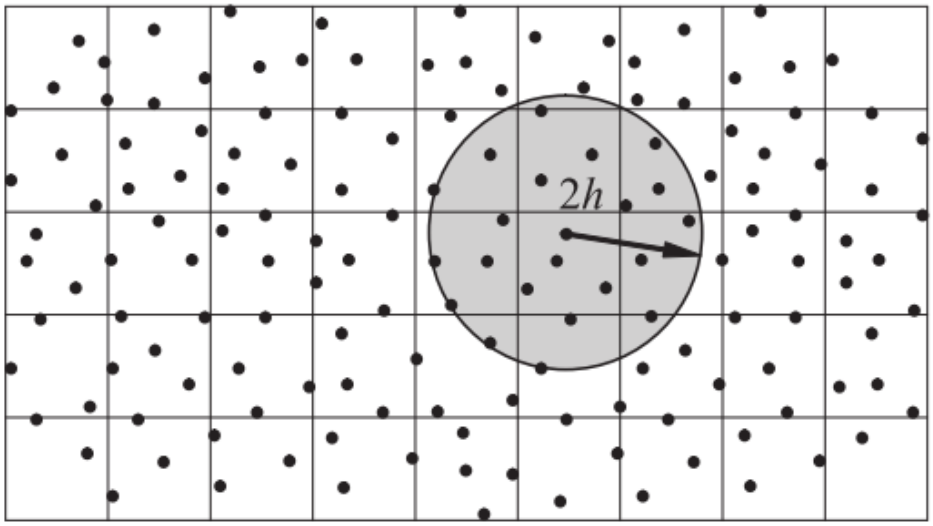

Figure 17. LS-Dyna Bucket Sort Method and Particle Sphere of Influence, 2*h*.

(Vesenjak and Ren, 2009)

In LS-Dyna, it is possible to vary the smoothing length during simulation to account for the changing of particle density, particularly when particles are becoming less dense, such as in tensile loading. As a result, the numerical inaccuracies caused by particles moving from adjacent particles' spheres of influence is reduced such that less dense particle fields have larger smoothing lengths for each particle. Downsides of using SPH are that enforcing essential boundary conditions is more difficult in applications of structural deformation, there is an

increased difficulty in estimating diffusion in material history, and the analysis of materials in tensile stress states is made more difficult due to the computational effects of increased smoothing length (Vesenjak and Ren, 2009; Wu and Hu, 2014).

In order to increase computational efficiency of SPH formulations and maintain a material interface across most of the material it is possible to create a SPH/Lagrangian hybrid model where only areas which are known to experience large deformation, or specific areas of interest within the model are modeled use SPH. The remainder of the model can then be formed with Lagrangian elements, using a special hybrid element formulation for elements along the Lagrangian/SPH border within the same material or part. The border hybrid elements contain SPH nodal locations which then provide a penalty force against the Lagrangian section of the element such that nodal iteration between the SPH and Lagrangian parts of the material are transferred to one another across the hybrid border. This method of using hybrid SPH greatly increases computational efficiency and simplifies the model creation process (Guo, 2010). For this study however it was found that the process of correctly assigning the contact and interaction between the SPH and Lagrangian parts was not well documented, and the computational efficiency of the simulation was improved in other aspects of the model without the use of hybrid Lagrange SPH constructions.

The process of creating SPH parts differs from traditional Lagrangian parts. Generally when creating an SPH part, a Lagrangian volume is first created in the area where the SPH part is desired. The Lagrangian elements are then filled with SPH such that the density and orientation of particles is dependent upon the parent Lagrangian mesh as seen in Fig. 18.

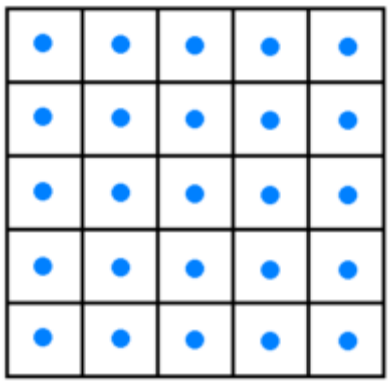

Figure 18. SPH particles are created from a parent Lagrangian mesh (Gretsch *et al.*, 2012)

When constructing the SPH particle distribution, it is important to maintain a uniform initial particle distribution within each part such that each particle has an equal initial smoothing length. This is crucial to the accuracy of the model as SPH rely of their sphere of influence to model nodal interactions and if a uniform body is not modeled uniformly with SPH, then its physical characteristics are inaccurate. For instance, when modeling cylindrical parts with SPH with a parent Lagrange geometry, the discrepancy must be made during creation to form the SPH from the Lagrange part such that SPH are approximately equidistant. See Fig. 19.

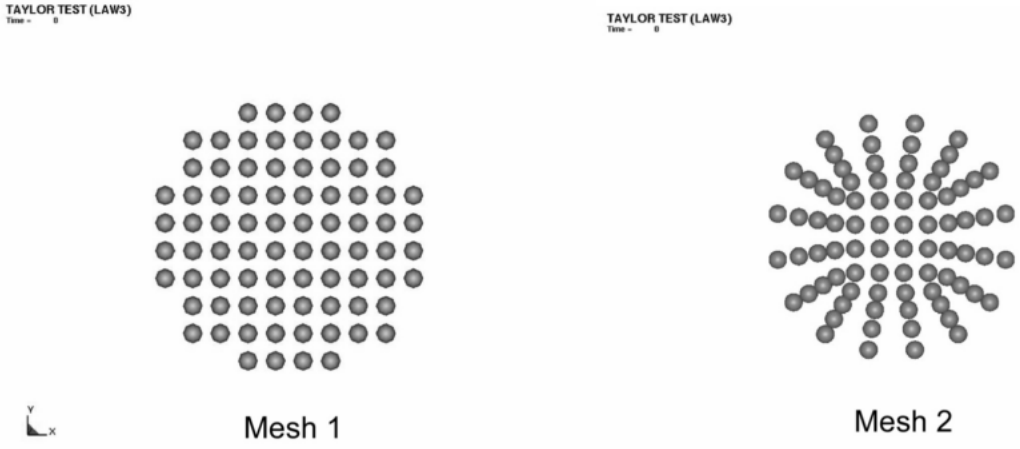

Figure 19. Mesh 1 shows a well distributed SPH particle field. Mesh 2 shows a poorly formulated SPH part. (Hallquist, 2006)

From Fig. 19 a clear discrepancy between a well distributed SPH particle field (mesh 1) and poorly distributed SPH field (mesh 2) can be seen. When using an SPH mesh such as in mesh 2, there is a large discrepancy between initial particle distances and can lead to inaccuracies. Therefore, when generating SPH models, the SPH configuration seen in mesh 1 was used to ensure equal particle initial separation.

6. Material Models

6.1 Fluid

Fluidic material models, for the purposes of this study, were largely meant only for the validation of various ALE and SPH methods due to their ease of use and easily predicable material deformation response. Lagrange element formulations were not used when modeling fluids due to the relative low viscosity of the materials chosen (vegetable oil and water) and the Lagrange formulation's limitations when modeling larger deformation. In preliminary testing, it was determined that fluid responses modeled using Lagrangian element formulation resulted in numerous element instabilities including element penetration and element zero volume errors. As such, ALE and SPH element formulations, which are commonly used to show fluid behavior were the only formulations extensively pursued for use in fluid modeling. The LS-Dyna material *Mat_9_Null was used due to its simple requirement of input parameters, its ability to show material strain-rate effects, and by direction of the LS-Dyna material manual. The non-zero material inputs for water and oil are listed in Table 1.

Table 1. *Mat_9_Null Non-zero material inputs

	Mass Density RO (kg/m^3)	Viscosity Coefficient
Water	1000	.001
Oil	700	.001

The viscous stress of the material is calculated using the equation

$$\sigma_{ij} = \mu \dot{\varepsilon}'_{ij}$$

where $\dot{\varepsilon}'_{ij}$ is the deviatoric strain rate and μ is the input viscosity coefficient.

*Mat_9_Null also requires an equation of state which was defined as a linear polynomial function with non-zero inputs seen in Table 2

Table 2. *EOS_Linear Polynomial Non-zero inputs

C1	2.2e9
V0	1

By definition of the EOS_Linear_Polynomial card, when all other coefficients are zero other than C1, it is defined as the elastic bulk modulus and the resultant equation of state (EOS) cannot be used for modeling any material behavior beyond the elastic regime. In this instance, this limitation is irrelevant when modeling fluidic response as the two fluids are assumed to only show elastic behavior. The pressure equation is of the form

$$p = C_0 + C_1\mu + C_2\mu^2 + C_3\mu^3 + \left(C_4 + C_5\mu + C_6\mu^2\right)E$$

where *E* is defined as the internal energy per initial volume, *V0,* and μ is defined as

$$\mu = \frac{1}{V} - 1$$

Such that *V* is defined as the relative volume (LS-Dyna, 2007).

A simple model consisting of a rigid shell aluminum ball with an initial velocity of 1 *m*/s dropping into the oil and water MMALE was created to validate the MMALE formulation. It was compared qualitatively against a similar model proposed by Alexander *et al.*, (2012) for general material deformation patterns and behavior. See Fig. 20.

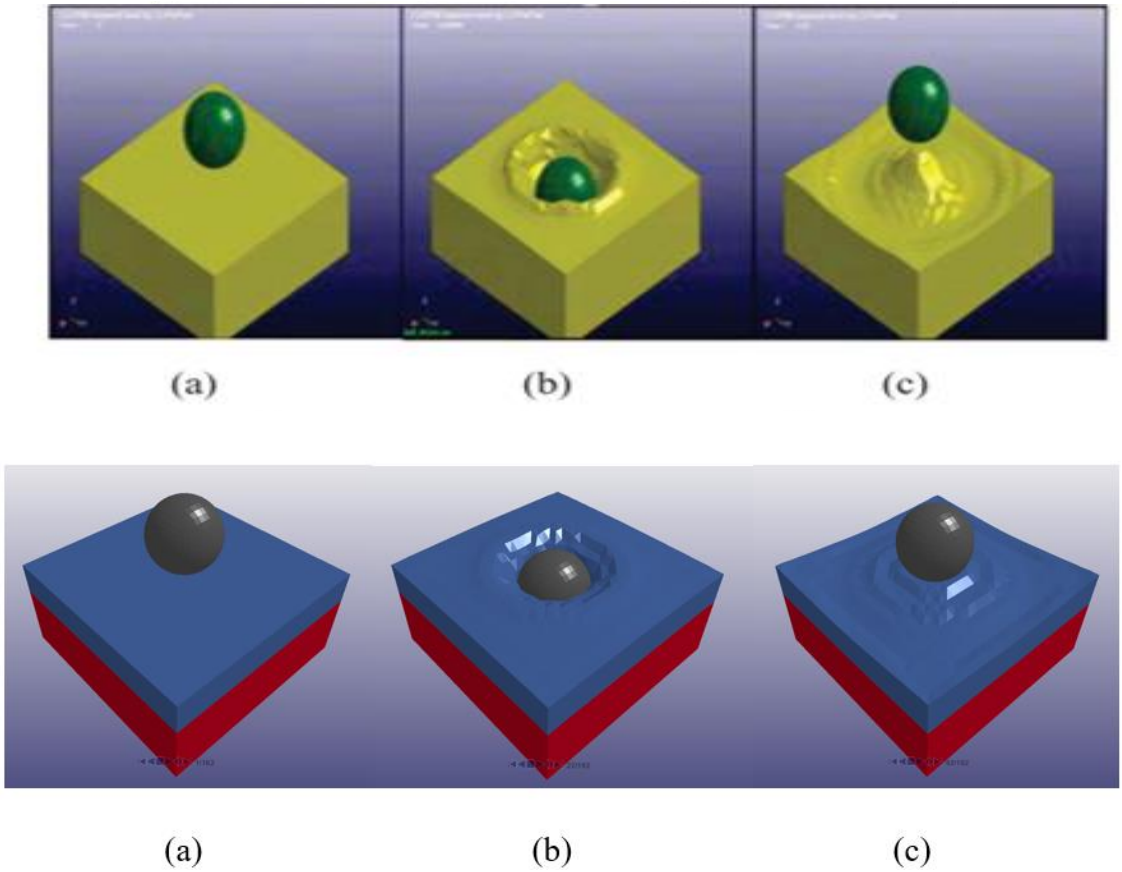

Figure 20. Current MMALE oil and water, bottom, comparison with ball into water, top (Alexander *et al.*, 2012)

The material deformation in the MMALE simulation was determined to be comparable to previous simple fluid modeling in LS-Dyna. As also suggested by Alexander *et al.* (2012), such an experiment could be validated qualitatively against a simple physical experiment. Base on the success of this simple MMALE model, it was determined that a similar construction methodology be used while creating the soil MMALE formulations.

6.2 Soil

Anticipated to be the nominal impact material for EEV missions, soil was extensively modeled using Lagrangian, MMALE and SPH methods to ensure that the most accurate method

was used for each different soil variation. A widely used and curtailed material card used for soil modeling, *Mat_5_Soil_and_Foam, was used as the soil material due to its ability to model pressure dependent materials and because its input parameters are generally easy to determine. The material card requires elastic shear modulus, G, bulk unloading modulus, BULK, three coefficients for a fit of the material's strength curve, a_o, a_1 and a_2, ten values for a pressure versus volumetric strain curve, mass density RO and various other material parameters are listed in Table 3 and Table 4.

Table 3. *Mat_5_Soil_and_Foam Carson Sink Soil Parameters

Material Parameter (m, kg, s)	LS-Dyna Syntax	Dry Soil	Wet Soil
Density	RO	1378.6 kg/m^3	1442.75 kg/m^3
Shear Modulus	G	1.096e7 *Pa*	3.447e6 *Pa*
Bulk Unloading Modulus	K	1.338e8 *Pa*	8.687e7 *Pa*
Yield Surface Coefficients	A0 A1 A2	1.336e7 Pa^2 6625.8618 *Pa* .822	9.355e7 Pa^2 1.281e4 *Pa* .439
Pressure Cutoff	PC	0	-1
Pressure – Volume Point 1	EPS1, P1	0, 0 *Pa*	0,0 *Pa*
Pressure – Volume Point 2	EPS2, P2	-.001, 1.655e4 *Pa*	-.007, 3.103e4 *Pa*
Pressure – Volume Point 3	EPS3, P3	-.002, 2.455e4 *Pa*	-.0102, 3.696e4 *Pa*
Pressure – Volume Point 4	EPS4, P4	-.004, 3.309e4 *Pa*	-.013, 4.137e4 *Pa*
Pressure – Volume Point 5	EPS5, P5	-.005, 3.944e4 *Pa*	-.019, 4.826e4 *Pa*
Pressure – Volume Point 6	EPS6, P6	-.01, 5.081e4 *Pa*	-.063, 8.274e4 *Pa*
Pressure – Volume Point 7	EPS7, P7	-.07, 1.379e5 *Pa*	-.125, 1.351e5 *Pa*
Pressure – Volume Point 8	EPS8, P8	-.111, 2.068e5 *Pa*	-.185, 2.206e5 *Pa*
Pressure – Volume Point 9	EPS9, P9	-.15, 3.447e5 *Pa*	-.22, 3.241e5 *Pa*
Pressure – Volume Point 10	EPS10, P10	-.18, 4.895e5 *Pa*	-.259, 4.619e5 *Pa*

Table 4. Notional *Mat_5_Soil_and_Foam Rosamond Lake Soil Parameters (Courtesy of JPL)

Material Parameter (m, kg, s)	LS-Dyna Syntax	Moisture 10%	Moisture 25%	Moisture 45%
Density	RO	1200 kg/m^3	1200 kg/m^3	1200 kg/m^3
Shear Modulus	G	4.16e6 Pa	3.441e5 Pa	1.227e5 Pa
Bulk Unloading Modulus	K	5.108e9 Pa	8.888e9 Pa	5.001e9 Pa
Yield Surface Coefficients	A0 A1 A2	3.398e10Pa^2 1.181e5 Pa .1027	3.565e9 Pa^2 1011.7 Pa 7.177e-5	2.189e8 Pa^2 18.8139 Pa 4.042e-7
Pressure Cutoff	PC	-100	-100	-100

Pressure – Volume Point 1	EPS1, P1	0, 0	0, 0	0, 0
Pressure – Volume Point 2	EPS2, P2	-.066, 6.249 *Pa*	-.01, 2.737e5 *Pa*	-.0024, 2.236e5 *Pa*
Pressure – Volume Point 3	EPS3, P3	-.1368, 1.386e6 *Pa*	-.0769, 7.028e5 *Pa*	-.005, 4.819e5 *Pa*
Pressure – Volume Point 4	EPS4, P4	-.2031, 2.419e6 *Pa*	-.1254, 1.073e6 *Pa*	-.0076, 2.246e6 *Pa*
Pressure – Volume Point 5	EPS5, P5	-.2724, 4.107e6 *Pa*	-.1565, 1.313e6 *Pa*	-.0102, 9.275e6 *Pa*
Pressure – Volume Point 6	EPS6, P6	-.3426, 6.911e6 *Pa*	-.1764, 1.809e6 *Pa*	-.0127, 1.587e7 *Pa*
Pressure – Volume Point 7	EPS7, P7	-.4144, 1.126e7 *Pa*	-.1908, 3.045e6 *Pa*	-.0153, 2.551e7 *Pa*
Pressure – Volume Point 8	EPS8, P8	-.484, 1.83e7 *Pa*	-.2006, 8.035e6 *Pa*	-.0179, 3.432e7 *Pa*
Pressure – Volume Point 9	EPS9, P9	-.5521, 2.975e7 *Pa*	-.2074, 2.962e7 *Pa*	-.0204, 4.128e7 *Pa*
Pressure – Volume Point 10	EPS10, P10	-.6223, 4.89e7 *Pa*	-.212, 4.976e7 *Pa*	-.023, 5.017e7 *Pa*

The elastic shear modulus, the slope of the shear stress versus shear strain curve, determines the shear deformation upon loading of the soil and is obtained through a uniaxial strain test. The same test can be used to determine the pressure versus volumetric strain curve values. A hydrostatic compression test is used to determine the unloading bulk modulus by fitting the mean stress versus strain curve during the unloading stage of the test. Finally, a triaxial compression test is used to determine the coefficient values for the shear failure envelope (Thomas *et al.*, 2008). The deviatoric behavior of the material is pressure dependent such that through the constants a_o, a_1 and a_2 it is described as

$$\phi_s = \frac{1}{2} s_{ij} s_{ij} - \left(a_0 + a_1 p + a_2 p^2 \right)$$

where s_{ij} is the measured triaxial stress. The single history variable used by *Mat_5 is the maximum volumetric strain in compression, which is progressively updated when a new value is measured at each time step. Using the equation

$$s_{ij}^{n+1} = \left(\frac{a_0 + a_1 p + a_2 p^2}{\frac{1}{2} s_{ij} \, s_{ij}} \right)^{1/2} s_{ij}^{*}$$

an updated value for the triaxial stress can be found upon yield condition violation where s^{*}_{ij} is the updated trial stress (Hallquist, 2006).

The triaxial compression test is performed through the hydrostatic loading of a specimen to a confining pressure, at which time a compressive axial strain is applied. Typically a range of confining pressures are used over multiple tests to build a "strength envelope" for that material and to determine the relationship between normal stress levels and shear strength. Uniaxial strain testing involves the application of compressive axial strain with no strain in the radial direction. A dynamically changing confining pressure is applied to prevent radial strain from occurring. Therefore in a uniaxial strain test the total volumetric strain of the soil sample is equal to the axial strain, and is easily measured compared to other testing scenarios. Output from the uniaxial test allows for the estimation of the Poisson ratio using the relationship between axial stress and the applied confining pressure which is then used to determine the shear and bulk moduli (Thomas *et al.*, 2008).

Used in a study by Thomas *et al.*, (2008), soil parameters for *Mat_5_Soil_and_Foam based on soil samples from Carson Sink, NV were used to justify the validity of soil impact models. The objective of Thomas et al. was to predict loading on the Orion Crew Exploration Vehicle (CEV), an airbag assisted, crewed impact vehicle. Carson Sink is similar to the UTTR in

that it is a playa, a dry lake bed, extending over a large area of varying soil, sand and rock conditions. Generally, the area is a dry, relatively hard clay with increasing moisture content at depth. The area is prone to seasonal flooding which can drastically alter the moisture content of the soil to the point where the soil is completely submerged in water. The behavior of the soil significantly changes according to moisture content where it is at its hardest when at its lowest moisture percentage and is progressively softer and more fluidic at higher water contents. There are areas of large sand dunes which interrupt what is otherwise flat clay. Unlike in some other dried lake beds, there is no shoreline that accumulates rocks and sediment. Regardless, off-nominal impact materials were considered in this study as there is still the possibility of rock or concrete impact at the proposed landing locations.

As explained by Thomas *et al.*, (2008), there were two samples taken from Carson Sink, a wet and dry soil, each representing either end of the soil saturation spectrum. Carson Sink, unlike other locations considered such as Cuddeback Lake, CA, does not contain a diverse soil variety, rather, it shows a wide range of soil moisture contents of the same soil type. This behavior is similar to the soil used by JPL for its EEV impact testing taken from Rosamond Lake, as they also focus on the variation of soil moisture rather than type of soil. Thomas *et al.* collected two samples from Carson Sink, a dry and wet saturation such that the two samples represent the two extremes of the area in terms of moisture content. Simulations were performed using both soils to show a potential loading envelope for the EEV impacting the most and least saturated Carson Sink soils.

Additionally, Rosamond Lake soil parameters, courtesy of JPL, were used and compared with the results from the Carson Sink simulations. The Rosamond Lake soil parameters have been used by JPL in validation of an impact testing campaign of sample EEV geometries. Their

objective is to successfully model the acceleration curve measured by an accelerometer placed in the nose of the test EEV penetrometer. Once the acceleration curves of these test are able to be recreated using numerical simulation, the soil parameters for the UTTR site will be input into the simulations, along with a higher fidelity EEV geometry with realistic materials. The resultant simulations will be used to predict mission scenario loading of the EEV and OS without the need for continued empirical testing. This methodology can be applied to the analysis of the UTTR site using the relative behavior of loading during soft and hard soil impacts and the proposed methodology used for loading predictions for impact in Rosamond Lake and Carson Sink.

6.3 Concrete

In the event that the EEV does not impact with the UTTR soil, there is a high likelihood that it would impact a rock or concrete like surface. The significantly harder, and more brittle impact surface would produce a much larger *G* load on the EEV than in a nominal impact case. In order to account for such a scenario and predict possible loading on the EEV, impact simulations using a concrete material model were performed.

The material card *Mat_159_CSCM_Concrete was chosen as the concrete material to be used due to its simple design, few required material inputs and well documented use. The Continuous Surface Cap Model (CSCM) implements isotropic constitutive equations, a three stress invariant yield surface, damage based softening, using element erosion and stiffness modulus reduction. Additionally, in the case of larger strain rate applications, such as in EEV impact scenarios when strain will occur very quickly as a function of the impact speed, the rate effects of concrete deformation are implemented. The strength of concrete is strain rate dependent such that the strength increases as strain rate increases. This means that under a large impulse impact where a large strain rate can be expected, the strength of concrete is much larger

than in a lower impulse impact. The behavior of these rate dependent parameters were determined through laboratory uniaxial testing by Murray, Abu-Odeh and Bligh (2007). This LS-Dyna model provides a set of default input parameters and only requires the material density, brittle damage modulus, aggregate size and the unconfined compressive strength. Using material data from a study on concrete road barrier impacts by Murray, Abu-Odeh and Bligh (2007), a series of simulations were created to model the survivability of an EEV impact with a concrete or hard aggregate surface. Non-zero LS-DYNA inputs are shown in Table 5.

Table 5. Non-zero/default, Material Input Parameters for *Mat_159_CSCM_Concrete

Material Parameter (m, kg, s)	LS-DYNA Syntax	Value
Mass Density	RO	2320
Element Erosion Criteria	ERODE	1
Compression Modulus Recovery	RECOV	10
Unconfined Compressive Strength	FPC	3.044e7
Maximum Aggregate Size	DAGG	.025
Unit Conversion for Calculation	UNITS	4

6.4 EEV Materials

In order to create a more realistic impact scenario, a deformable EEV-R model was used when impacting concrete or at off-nominal angles in order to more accurately capture predicted deformation. LS-Dyna offers numerous material models for modeling elastic plastic behavior. Three such models were chosen: *Mat_Elastic, *Mat_Piecewise_Linear_Plasticity, *Mat_Plastic_Kinematic. See Table 6, Table 7, and Table 8 for Aluminum EEV material input parameters.

Table 6. *Mat_Elastic material inputs

Material Parameter	LS-Dyna Syntax	Value
Mass Density (kg/m^3)	RO	2700
Elastic Modulus (Pa)	E	68.9e9
Poisson Ratio	PR	.33

Table 7. *Mat_Plastic_Kinematic material inputs

Material Parameter	LS-Dyna Syntax	Value
Mass Density (kg/m^3)	RO	2700
Elastic Modulus (Pa)	E	68.9e9
Poisson Ratio	PR	.33
Yield Stress (Pa)	SIGY	276e6
Tangent Modulus (Pa)	ETAN	447.4e6

Table 8. *Mat_Piecewise_Linear_Plasticity

Material Parameter	LS-Dyna Syntax	Value
Mass Density (kg/m^3)	RO	2700
Elastic Modulus (Pa)	E	68.9e9
Poisson Ratio	PR	.33
Yield Stress (Pa)	SIGY	276e6
Tangent Modulus (Pa)	ETAN	447.4e6
Strain at Ultimate Failure	FAIL	.08

As the name suggests, *Mat_Elastic only offers the ability to model the elastic region of the material deformation. While this card is useful when only small elastic deformation is expected, it cannot show plastic deformation or failure, meaning it will show an unrealistically strong material when large deformation occurs. It is therefore predicted that this material will show a much larger peak acceleration than the other two material cards used, as an elastic only EEV cannot absorb the impact energy as well as one that will deform more. A *Mat_Plastic_Kinematic material card allows for the plastic deformation of the material by requiring the input of both a yield strength above which plastic deformation will occur, as well as a tangent modulus. The tangent modulus, a parameter also used in *Mat_Piecewise_Linear_Plasticity, is a linear approximation of the plastic stress-strain curve, calculated using the know plastic and ultimate yield strengths of the material, the elastic modulus and strain at ultimate failure. This approximation allows for the greater simplification of the

model by not requiring the input of an actual, more accurate stress-strain curve. This greatly simplifies to the calculation process during simulation and reduces the number of required inputs on the material card. It allows for the plastic modeling of the material with only limited known parameters, and increases accessibility of the simulations with respect to what materials can be used. These values were obtained from public material databases. The approximated stress-strain curve, used by both *Mat_Plastic_Kinematic and *Mat_Piecewise_Linear_Plasticity is shown in Fig.21.

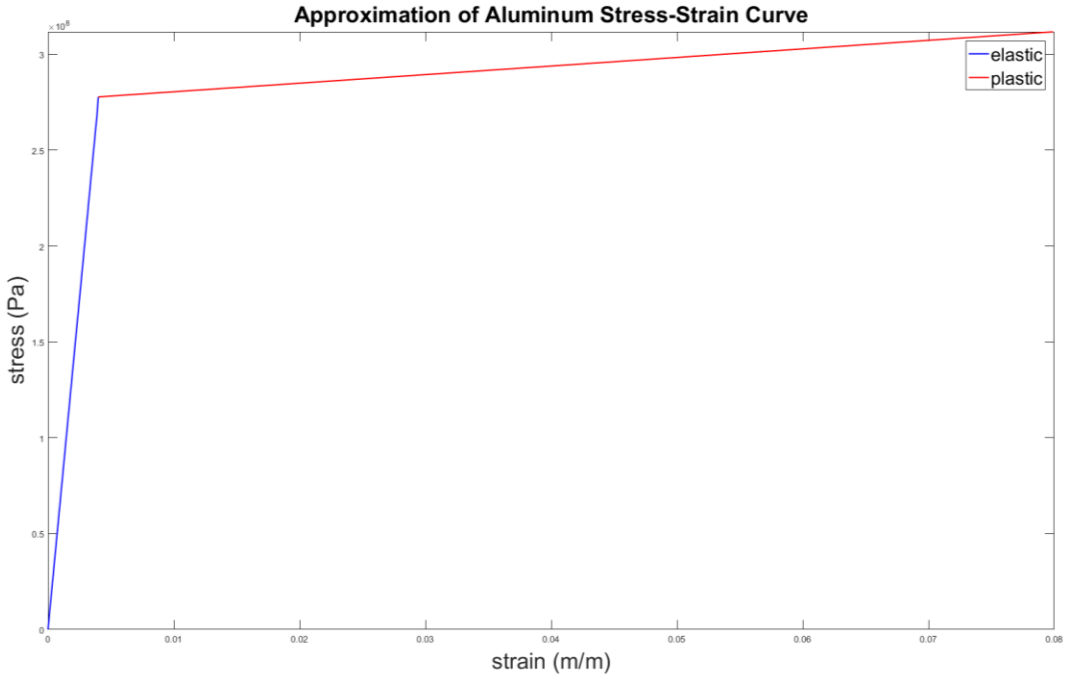

Figure 21. Stress-Strain approximation for Aluminum EEV

The main difference between the *Mat_Plastic_Kinematic and *Mat_Piecewise_Linear_Plasticity cards is that *Mat_Piecewise_Linear_Plasticity allows for the input of an ultimate failure. Upon ultimate failure, the elements are deleted from the visualization, yet the mass of each element remains for the sake of preserving momentum

conservation. A large advantage of this method is that it allows for both plastic and ultimate failure where the other two material models do not. When large deformations are expected, as is the case when impacting very brittle, or rigid surfaces, having the capability to show ultimate failure of the EEV becomes more valuable. While the other materials will most likely prove adequate for showing smaller EEV deformation, such as during off-nominal soil impact scenarios, they will show an overly strong material during the application of loads larger than the yield strength.

7. Model Creation

Final model geometries were based upon past and current EEV experimental setups used by NASA JPL for empirical EEV impact testing. In order to progressively validate the accuracy and efficiency of each experimental parameter such as mesh densities, element formulation or LS-Dyna material models, the complexity and resolution of each scenario were progressively increased, gradually increasing model fidelity. Generally in the case of impact problems this involved first the validation of the materials being used, then finalization of the element formulation, increase of the model fidelity, and finally optimization of the meshing scheme. A simple ball/box model was created where a solid, rigid ball of a previously validated material such as steel or aluminum impacted the test material using a course, simple mesh, at a low velocity, with no acceleration. Using an estimate of how the impact material's deformation would occur, the appropriate element formulation was chosen for initial testing. Generally, very rigid, brittle materials, or more viscous soils were first modeled in Lagrangian, and less viscous materials were chosen to be modeled in ALE. Based on the behavior and elemental stability of the resulting simulation, it was determined what changes could be made to improve the stability and realism of the impact material, or if alternative materials would be better suited for the

current objective of the model. Upon stability validation, or in some cases when alternative element formulations were estimated to show possible improvements, a finalization of the element formulation was made. Based on the initial behavior of the model, it was determined if another element formation would be more appropriate and was subsequently tested. Upon finalization of the material parameters and element formulation, the model's fidelity was steadily increased over progressive models through the application of gravity and external forces, replacement of the generic rigid ball with rigid EEV followed by a deformable EEV, and more accurate impact velocities. Once the final model intricacy was successfully tested, meshing schemes were explored and the model dependence on the mesh density was analyzed in an effort to determine the resultant convergence of the model.

Depending on the element formulation and desired impact material mesh geometries, the modification of the EEV mesh was required. In many cases when using ALE or SPH element formulations, a general element size ratio must exist between the ALE or SPH, and the Lagrangian EEV such that over penetration does not occur, and the contact parameters are able to accurately map material interactions. This ratio is typically a 1:1 ratio for ALE, and a 1:4 ratio for SPH such that there are 4 SPH particles for each Lagrange element. Due to the geometry of the EEV, specifically its rounded nose, the meshing scheme and element size were limited when meshing with relatively coarse mesh due to the number of elements in that area of the EEV required to capture the surface's curvature. This resulted in many simulations in which the generic EEV was used to be limited in the element size chosen for the impact material. Maintaining the desired element size ratio between the two impacting surfaces was required in order to prevent over penetration by ALE or SPH elements and also show realistic deformation

in element formulations with connected nodes, Lagrange and ALE, where the smoothness of material deformation is largely governed by the size of the elements.

There were two different EEV's used for testing, each of a different geometry and mass, both made from Aluminum 6061-T6 with material parameters listed in Table 9.

Table 9. Aluminum 6061-T6 EEV Basic Material Parameters

Parameter	LS-Dyna Syntax	Value
Density	RO	2700 kg/m^3
Elastic Modulus	E	7e10 *Pa*
Poisson's Ratio	PR	.3

The smaller of the two EEVs, the EEV-R has dimensions listed in Table 10

Table 10. Dimensions for EEV-R

Diameter	.5 *m*
Height	.15 *m*
Sphere Cone Radius	42 *mm*
Slope Angle from Normal	60.3 º

and is shown meshed in Fig. 22.

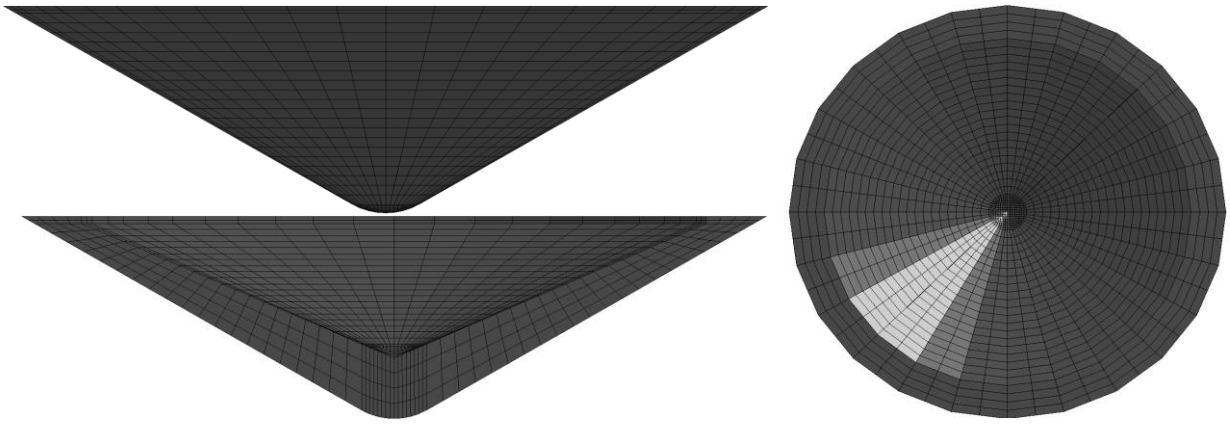

Figure 22. Meshed EEV-R

The other EEV, the CP300 has dimensions provided by JPL listed in Table 11.

Table 11. Notional CP-300 Dimensions. (Courtesy of JPL)

Diameter	1.35 *m*
Height	.39 *m*
Sphere Cone Radius	300 *mm*
Slope Angle from Normal	60.8 º
Nominal Mass	120.9 *kg*

The meshed representation of the CP-300 can be seen in Fig. 23.

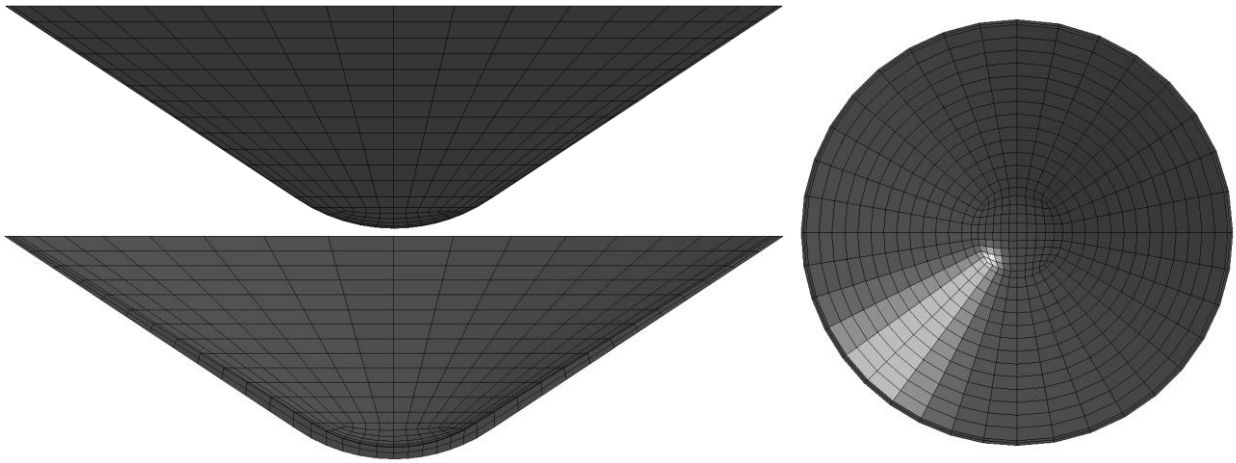

Figure 23. Meshed CP-300

The use of a fully integrated, and highly detailed EEV model is unneeded for much of this work since the main focus is on the soil model and the general behavior of the parameters of the EEV as they relate to the peak acceleration. During simulation, the mass of each EEV is able to be increased from its nominal mass to simulate an increased payload or increase in internal component mass. Therefore, since the mass is changed independent of the geometry, and the geometry of the leading face of the EEV is most crucial of impact behavior, these approximations of the EEV are used. Additionally, this technique reduces the complexity of the model and as a result, the computational cost and meshing difficulty. When meshing the curved surfaces of the EEV, the element size is limited based on the intensity of the object's topography

changes. This limitation is the cause for the mush denser mesh around the vertical center of the EEVs since in order to capture the geometry, the element size must be decreased. Also, when meshing a circular object using radially emanating elements, the size of the more central elements is typically much smaller than that of the outer most elements. As a result, a compromise must be made to make elements towards the center which are small enough to capture the curved geometry and to ensure that the elements around the outer edge of the EEV are not overly large, but also large enough to maintain a computationally effective aspect ratio and lower simulation time.

The soil geometry was universally constant across all simulations. A 2*m* x 2*m x* 1.5*m* cubic geometry was generated as the soil. The soil consists of two separate parts, a surface and sub-surface part such that the subsurface part begins at .203 *m* in depth and is the denser of the two soils. The boundary conditions of the soil were set to be fixed along the bottom horizontal plane and each vertical side plane along the outside of the geometry. This simulated a fixed

container in which the soil is housed. A constant gravity load is applied across the model for the duration of the simulation. A representation of this construction is shown in Fig. 24.

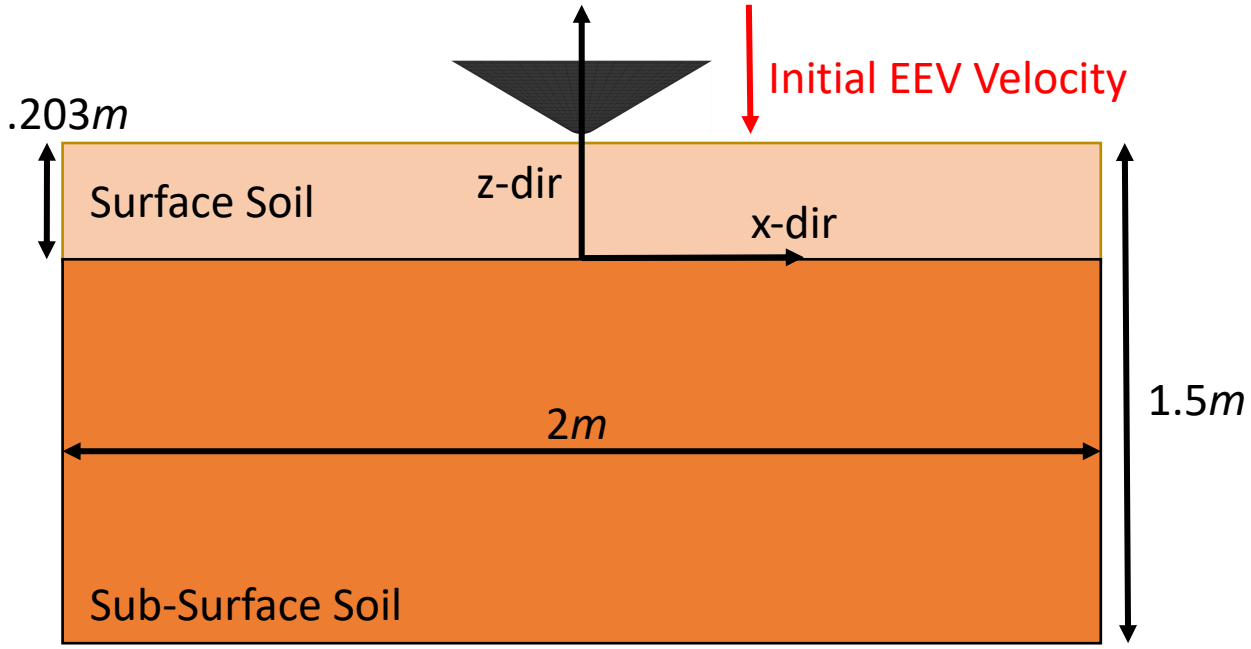

Figure 24. Impact model representation

8. Results and Discussion

Data results were generated through the LS-Dyna output ASCIII and were filtered when necessary using a Butterworth filter via Matlab. When used, the filter applied was a second order filter with normalized cut-off frequency of .1π rad/sample. This filter was selected because it was able to smooth the data and decrease any excessively large vibrations in the results without detracting from the overall trend of each data set. Displayed data is filtered using this technique unless otherwise specified.

8.1 EEV-R Mass Variation

In order to gain a perspective of the influence of changes in EEV mass on the peak EEV acceleration upon soil impact, a study was performed using Lagrangian, MMALE and SPH element formulations. The goal of this section is to establish a relationship between EEV mass, peak acceleration and penetration depth, all other parameters held constant so that effects due to changes in payload mass could easy be predicted. All three numerical formulations were used in an effort to validate the legitimacy of each one through the comparison of its results to the others. Due the somewhat large percent error associated with the SPH and Lagrange formulations during material validation (see 8.3.1), these formulations were compared with the results of the MMALE simulations in this section over numerous trials. This was done to show that they have the capability to produce results consistent with MMALE, a model validated in section 8.3.1, and that errors in reproducing the specific test scenario provided were unique to that scenario. Where large errors were found between the numerical formulations in this section, various element parameters, most frequently the element size, were varied on a case by case basis to optimize each model to the scenario being modeled. Using this process, the results of each modified simulation were compared across numerical formulations to ensure that each formulation produced consistent results.

The findings from this section can be used to predict changes in peak acceleration due to different sample sizes, the addition of internal components or any increase in the payload of the EEV without changing its overall size. A constant EEV impact velocity of 40 *m/s* was chosen across all trials and the EEV was chosen to be rigid to eliminate vibrations and non-uniform accelerations through its geometry.

8.1.2 Lagrangian

A traditionally easy formulation to work with and to create models from, the simplest formulation available, Lagrangian, was initially used to model the deformation of soil due to EEV impact. Rosamond 25% saturated soil was used during the first series of tests due to its comparatively high viscosity, and thus predicted lowest deformation of all available soil models. A sample acceleration curve generated using a 50 *kg* EEV-R, can be seen in Fig. 25.

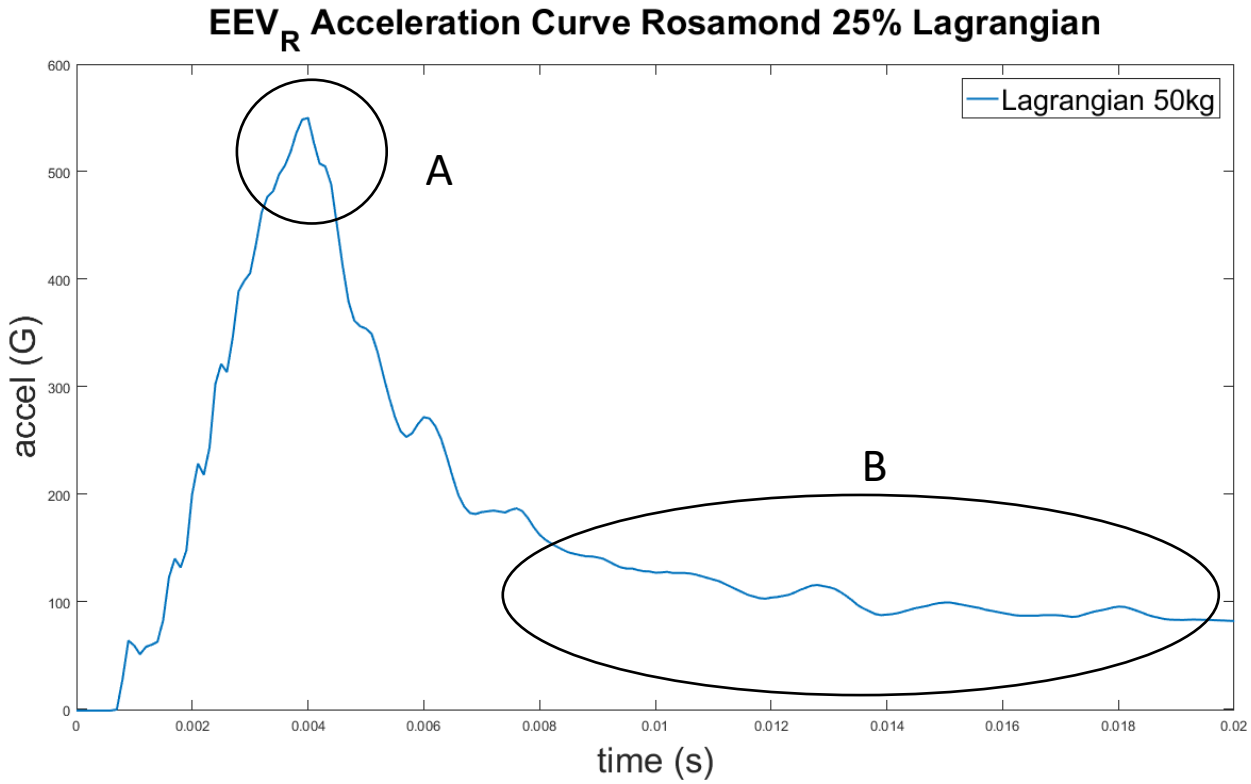

Figure 25. 50 kg EEV-R z-acceleration during impact with Rosamond 25% Lagrangian soil

From Fig.25 there can be seen two distinct behaviors occurring in the acceleration curve. Region A shows peak acceleration, occurring after the initial loading of the soil, and region B shows the prolonged acceleration due to the large hour glassing effects in the simulation. As the EEV impacts, the Lagrangian elements become increasingly distorted with more soil deformation, leading to simulation instability, characteristic of Lagrangian elements under larger

deformation. A progression of this element distortion can be seen in the time-lapse shown in Fig. 26.

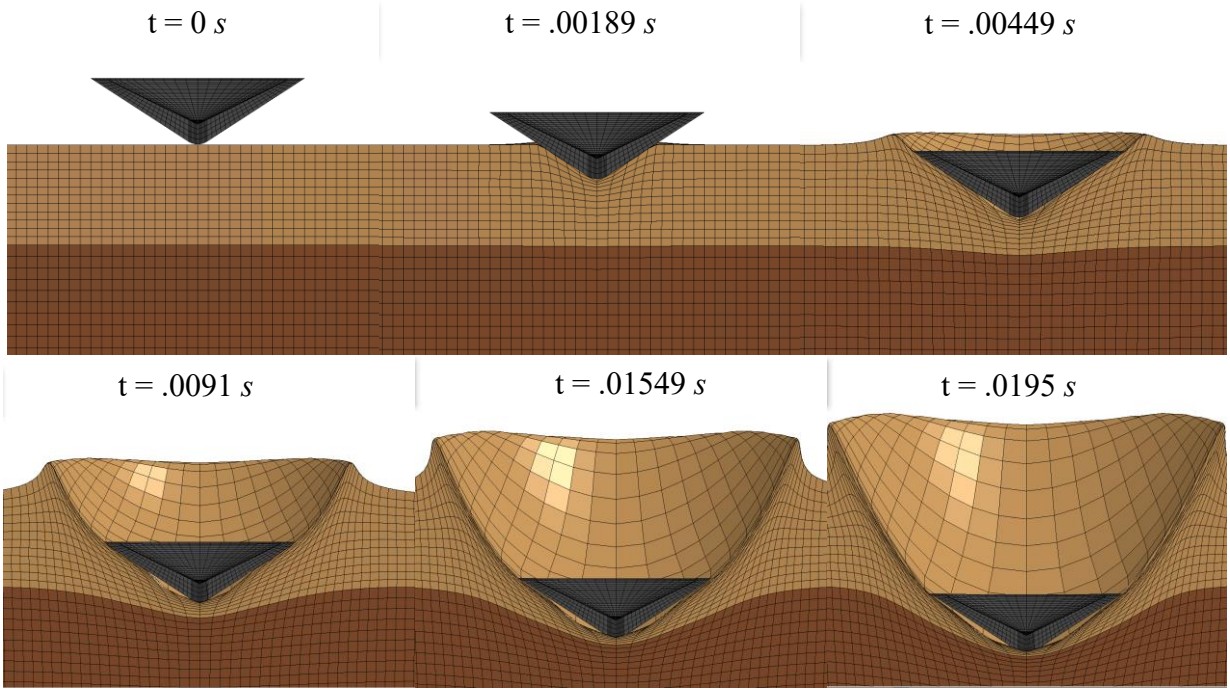

Figure 26. EEV-R time-lapse of Rosamond 25% Lagrangian penetration

The large distortion in the Lagrangian elements is expected during large deformation, but this distortion results in large amounts of simulation energy being diverted to hourglass energy. A plot of the simulation energies can be seen in Fig. 27.

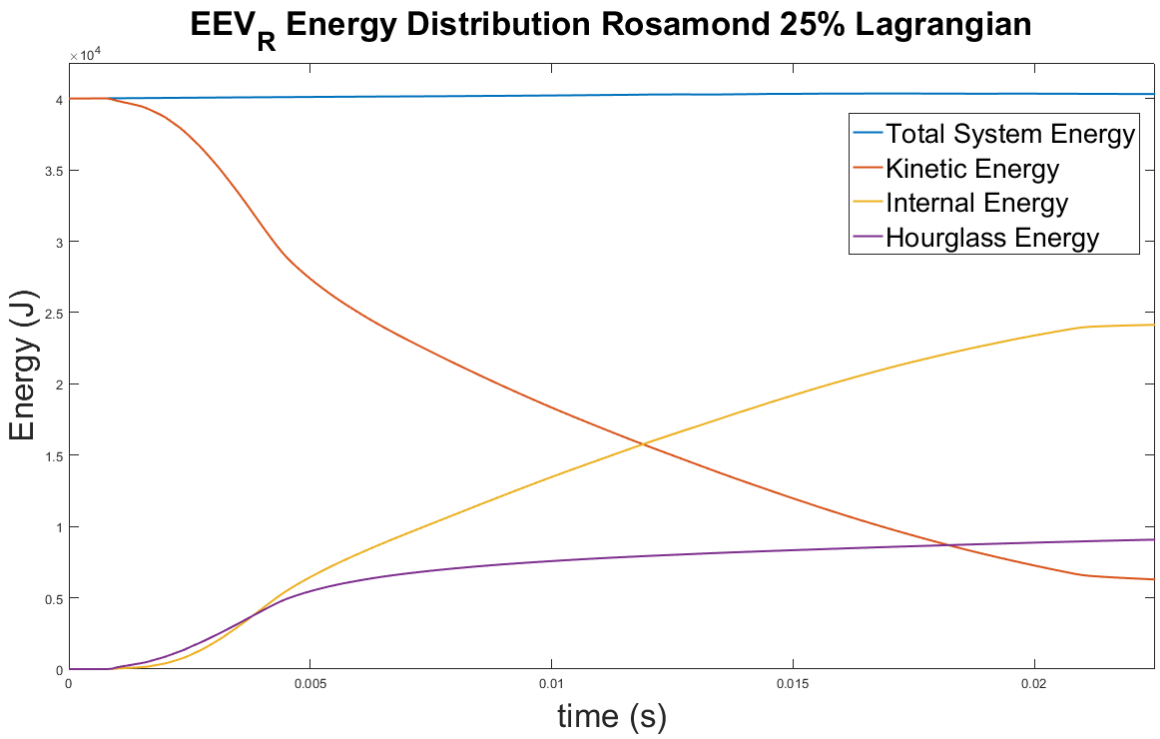

Figure 27. EEV-R impact with Rosamond 25% Lagrangian soil energy distribution

The hourglass energy increases to a significant percentage of the total energy after the peak acceleration occurs, at approximately .004 *s*, due to the increase in the element distortion. This also is a cause of extremely prolonged non-zero EEV acceleration during region B of Fig.25. The excessive energy unrealistically maintains EEV acceleration as distortion increases. The same pattern can be seen in all other cases, seen in Fig. 28

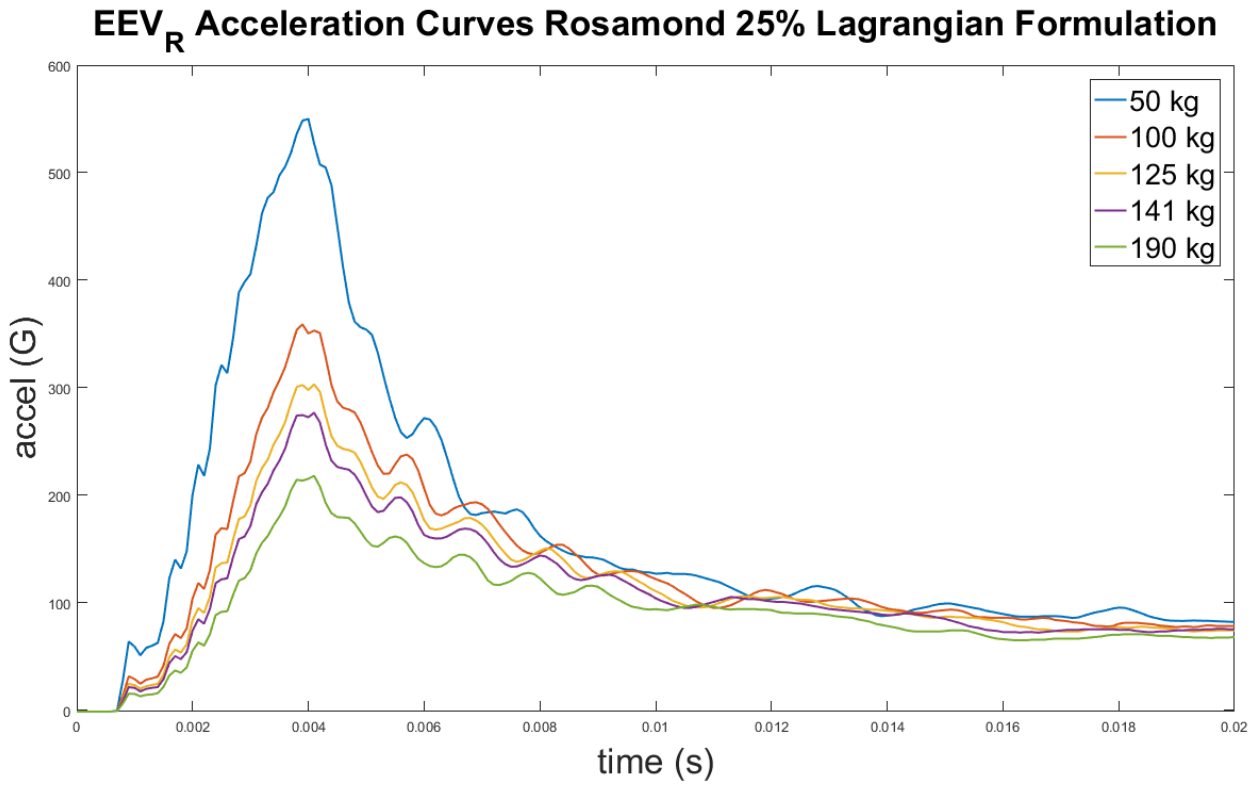

Figure 28. Unfiltered EEV-R z-acceleration vs. time for Rosamond 25% soil, Lagrangian formulation

The measured peak acceleration of each case is shown in

EEV- R Mass (*kg*)	Peak Acceleration (*G*)
50	549.99
100	359.03
125	303.17
141	276.76
190	218.18

Despite having drastically different peak accelerations, each mass case maintains an approximately equal residual acceleration during later time steps. Due to this characteristic of the simulations, it can be estimated that the deformation present in these impact scenarios is too large for Lagrangian elements to accommodate accurately. To provide further evidence of the inaccuracy of Lagrangian elements, a CP-300 impact test was simulated using Lagrangian elements and is discussed further in subsequent sections. Due to the found limitations of

Lagrangian elements for modeling the high deformation of soil, further simulations using soil impact surfaces were performed using MMALE or SPH elements.

The Lagrangian mesh was refine in order to determine if any reduction of hourglassing would occur. The results of the mesh refinement are shown in Table 1 and Fig.29.

Table 12. Results of Lagrangian mesh refinement

Number of Elements	Peak Accel (G)	Percent Convergence
299,820	549.99	-
1,199,280	527.79	4.04 %

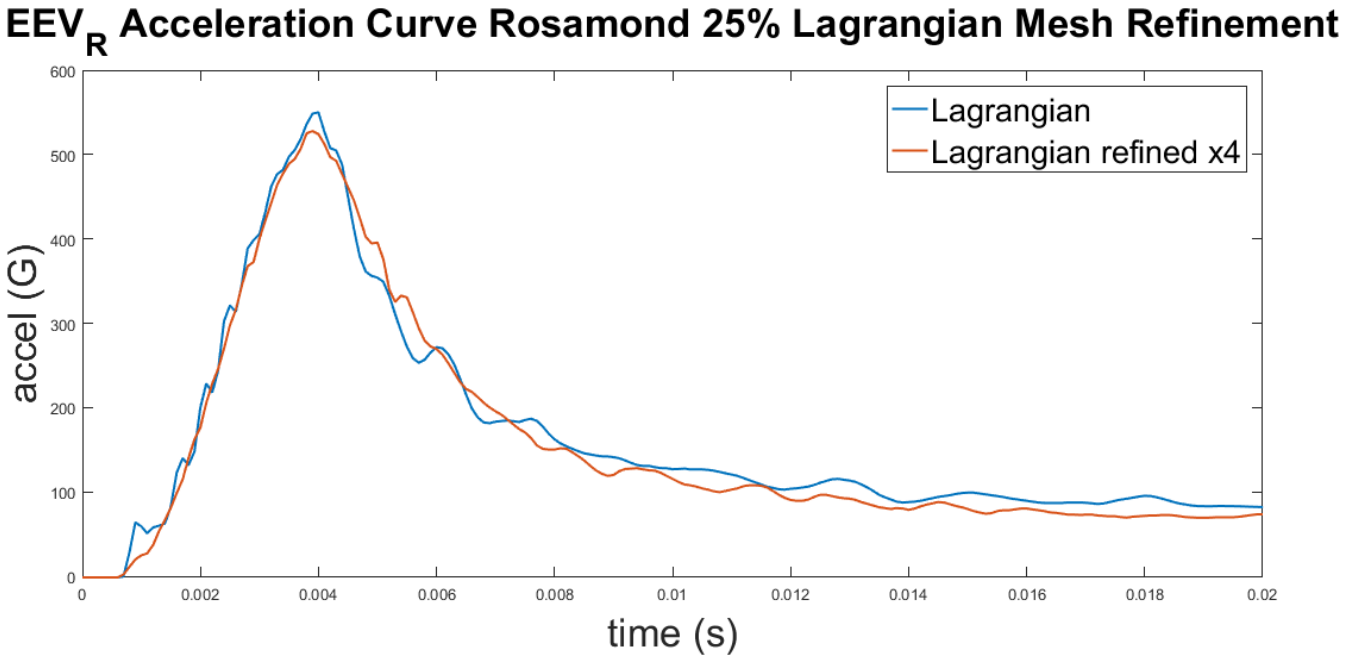

Figure 29. Unfiltered z-acceleration curve of refined Lagrangian mesh

It was determined based on the resultant acceleration curve of the refined mesh that the hourglassing is still occurring, and that the deformation of the Lagrange elements is too large to maintain simulation accuracy. The further refinement of the mesh resulted in the negative volume of elements due to over compression, and for this reason, further refinement was suspended. Therefore, alternative element formulations are preferred, and were explored more thoroughly.

8.1.2 MMALE

Due to the clear limitations seen in the analysis of the Lagrangian element simulations, the MMALE formulation was explored significantly further for its use as a soil modeling tool. Both Rosamond and Carson Sink soils were analyzed using MMALE for this reason. The peak EEV-R acceleration values and penetration depths can be seen in Table 13 for Carson Sink, and Table 14 for Rosamond.

Table 13. Compares EEV-R mass with peak acceleration and maximum penetration depth Carson Sink soil

EEV Mass (*kg*)	Dry Soil Peak Accel (*G*)	Wet Soil Peak Accel (*G*)	Dry Soil Max. Penetration Depth (*m*)	Wet Soil Max Penetration Depth (*m*)
50	605.39	564.13	.426	.361
100	457.33	395.78	.534	.461
125	401.49	344.97	.577	.511
141	373.51	314.97	.602	.552
190	299.29	264.97	.665	.615

Table 14. Compares EEV-R mass with peak acceleration and maximum penetration depth Rosamond Soil

EEV Mass (*kg*)	25% Sat. Soil Peak Accel (*G*)	45% Sat. Soil Peak Accel (*G*)	25% Sat. Soil Max. Penetration Depth (*m*)	45% Sat. Soil Max Penetration Depth (*m*)
50	545.35	565.63	.550	.582
100	353.12	425.09	.679	.741
125	283.62	327.22	.747	.795
141	247.88	277.78	.775	.811
190	277.02	273.54	.710	.809

A general pattern in the EEV acceleration can be seen throughout each mass case. The behavior of a 100 *kg* EEV-R impacting Carson Sink dry soil can be seen in Fig. 30.

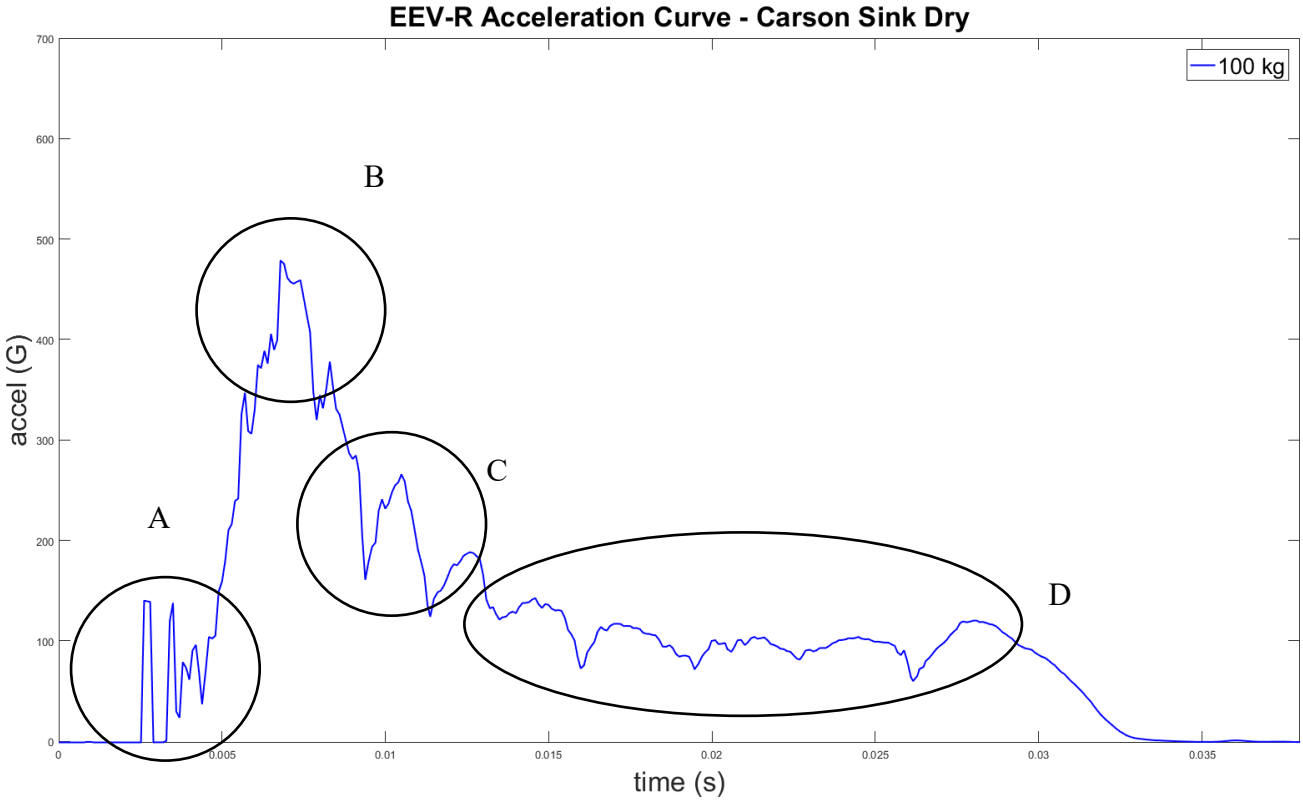

Figure 30. Unfiltred 100 *kg* EEV-R unfiltered z-acceleration during impact. Carson Sink Dry

There are four distinct regions in each EEV acceleration curve, labeled A, B, C and D in Fig. 30. Region A is a result of the conservative penetration settings made for the MMALE to ensure that the soil material does not over penetrate the EEV. While this setting ensures more realistic deformation during later time steps, it results in a larger, non-physical initial acceleration spike in the data due to the preemptive contact between the EEV and the soil. The maximum acceleration shown by region B represents the maximum impact acceleration of the EEV as it impacts the surface soil. It is at this point where the maximum acceleration of the EEV for that case is measured. After reaching maximum acceleration, the EEV descends through the surface soil, progressively feeling an increased effect of the denser sub-surface soil on its acceleration. Region C shows the time period where the more dense sub-surface soil significantly

influences the EEV's acceleration, resulting in a large secondary acceleration increase. The sub-surface soil extends the acceleration time of the EEV and in some cases which will be seen in Fig. 33, can result in a small increase in late impact acceleration. This prolonged, and less rapid deceleration is denoted by region D. The D region acceleration occurs when the EEV moves completely through the surface soil comes in direct contact with the sub-surface soil. Since the sub-surface soil is denser than the surface soil, it is more resistive to deformation than the surface soil, resulting its resistance to EEV penetration. A snapshot the simulation at each region can be seen in Fig. 31.

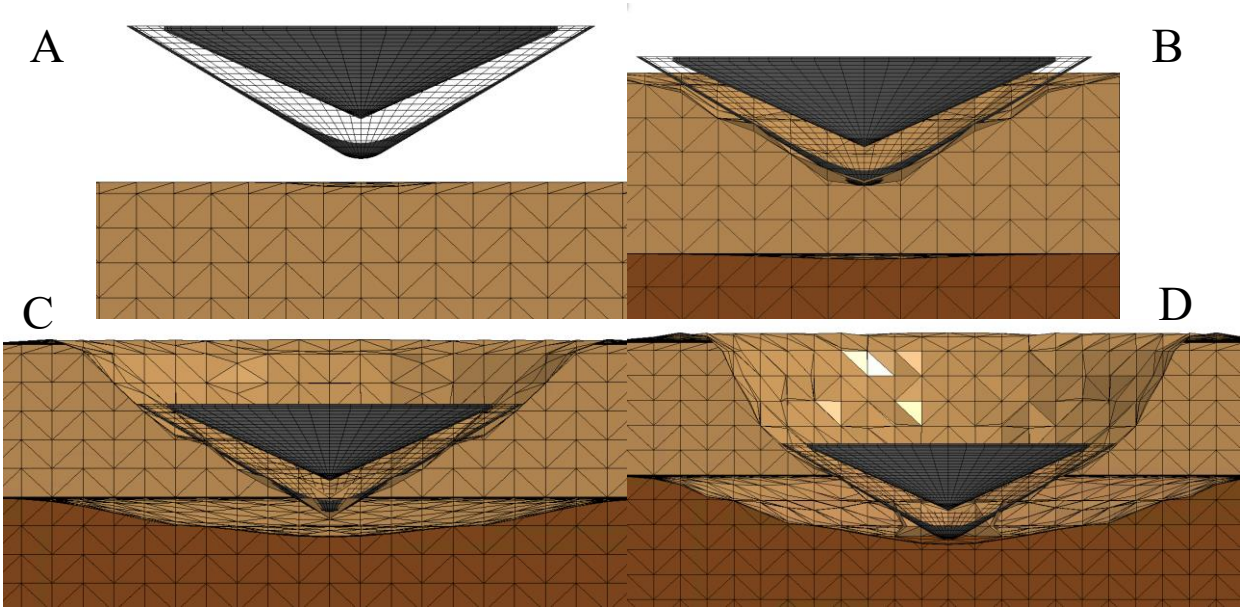

Figure 31. EEV-R time-lapse of acceleration curve regions

Using Fig. 31 as reference, region A is clearly a result of the conservative contact settings for the MMALE. The peak acceleration at region B does not show a defining characteristic other than most of the EEV is submerged at the time, and there is limited interaction with the sub-surface. Region C shows a significantly larger EEV effect on the sub-surface soil which translates to

region B where the EEV is in physical contact with the denser soil, leading to the prolonged acceleration magnitude.

The deformation of the soil was found to be significantly larger when the mass of the EEV was increased. See Fig. 32.

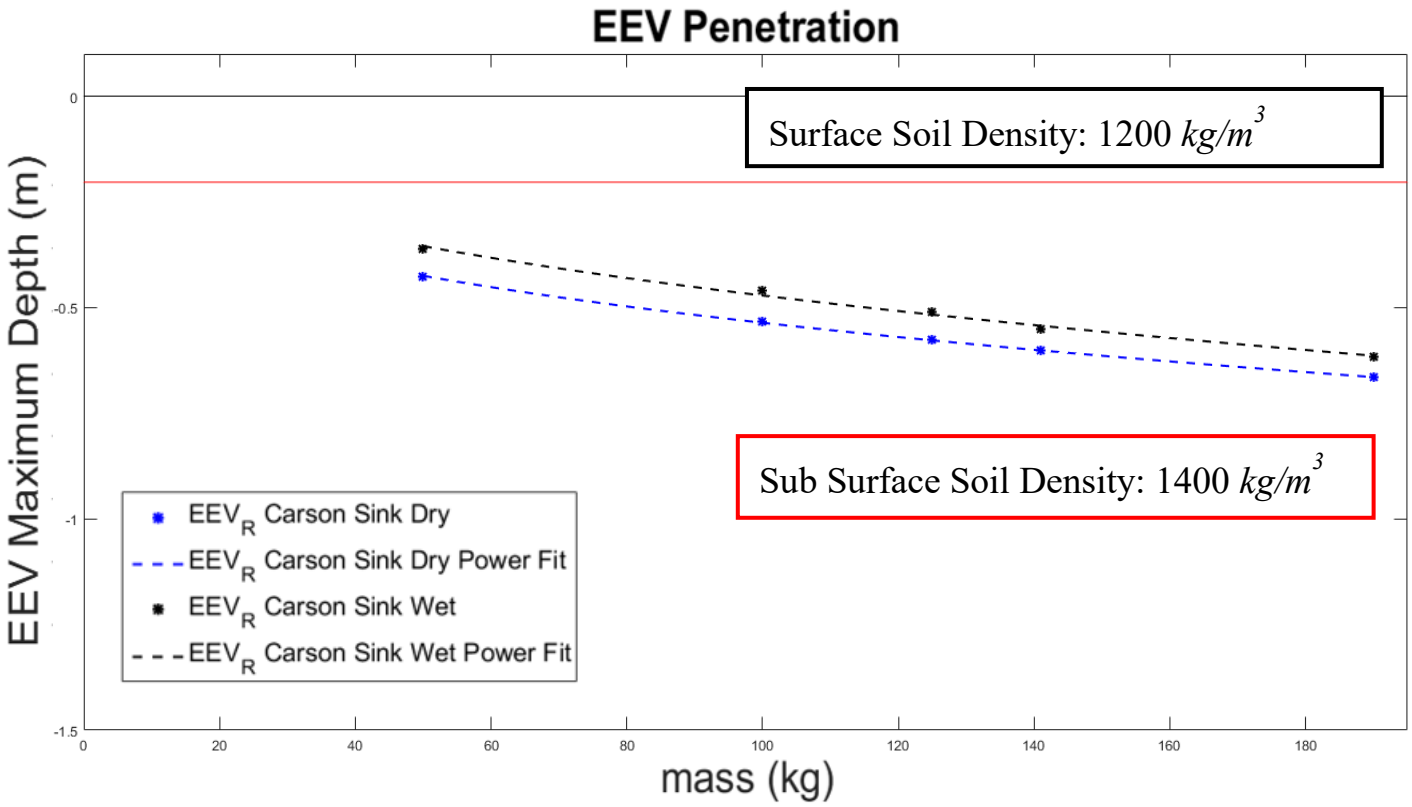

Figure 32. Total soil penetration depth as a function of changing EEV-R mass – Carson Sink

As a result of the more massive EEV-Rs penetrating deeper into the soil, their acceleration curves show a larger secondary acceleration peak proportional to increasing EEV-R mass. Also, total acceleration time of the EEV-R was largest at largest mass. The peak acceleration was found to increase as a function of decreasing mass. See Fig. 33.

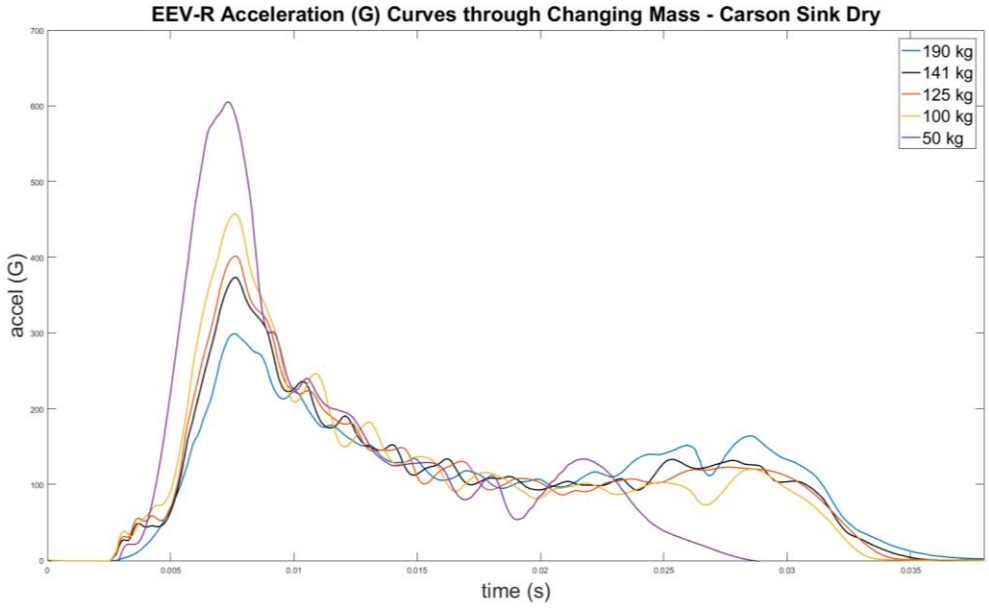

Figure 33. EEV-R z-acceleration curve as a function of changing EEV mass Carson Sink Dry (filtered at 1000 *Hz*)

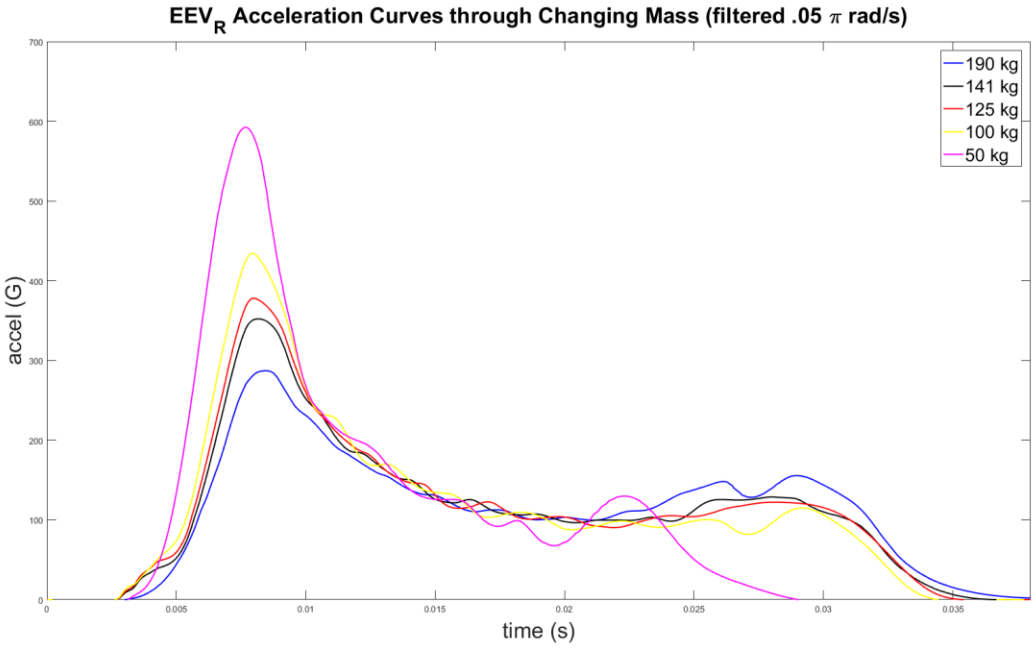

Figure 34. EEV-R z-acceleration curve as a function of changing EEV mass Carson Sink Dry (filtered at 500 Hz)

In addition to the 1000 *Hz* filter, a 500 *Hz* filter was also applied in Fig. 34 to mask any high frequency vibrations and to gain a perspective on the general acceleration behavior during impact. While it is obvious in these trials that the larger mass experiences a lower peak acceleration, another clear variation is present between masses. Since the more massive EEV penetrate more into the surface soil, they subsequently interact more with the denser, sub-surface soil. This interaction can be seen in Fig. 33 at approximately .02 *s*, where there is a sudden increase in EEV acceleration. This behavior occurs because once the EEV initially impacts the surface soil and experiences peak acceleration (~ .0075 *s*) and begins to move through the surface soil (~.0075 *s* - ~.02 *s*), it then must begin to displace and compress the more dense sub-surface soil which up until this time has not undergone significant deformation. See Fig. 35.

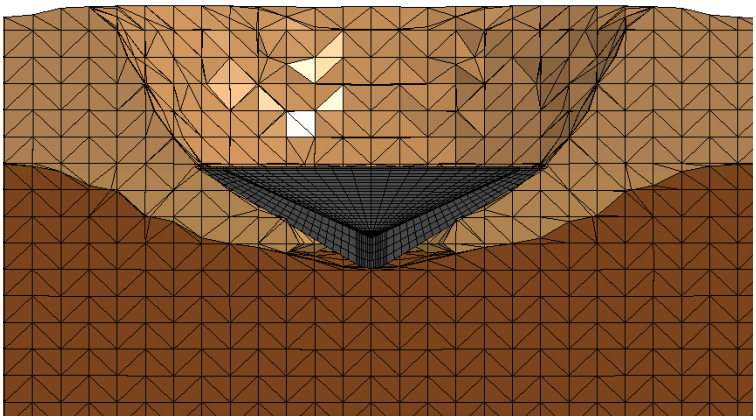

Figure 35. EEV begins interaction with the significantly less deformed sub-surface soil, resulting in acceleration increase in later time steps – Carson Sink Dry

The behavior of the acceleration curve is better understood when examining the behavior of the stress inside the soil, seen in Fig. 36.

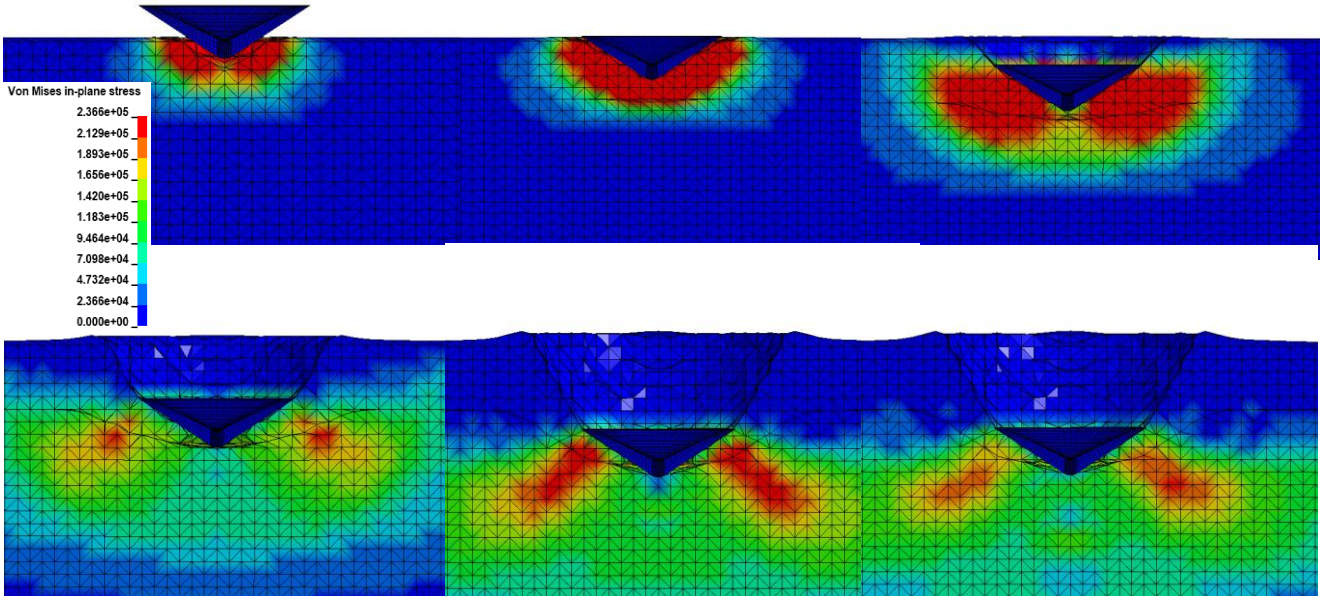

Figure 36. Von Mises stress (*Pa*) through cross-section of Carson Sink soil during impact

Based on the stress distribution in the soil, there can be seen to be two main loading stages during the impact; one at the initial impact of the EEV, corresponding to the first three frames of Fig. 36, and a secondary loading, in the 5th frame, mainly along the outer rim of the EEV which occurs after a slight drop in maximum stress in the soil, between loading stages. These two main large compressions of the soil coincide with the initial peak acceleration, and the secondary, more prolonged acceleration, of the EEV. Using this information, and the behavior of the EEV acceleration curve, the reaction of the soil can be more extensively understood and used in the design of EEV and OS construction. Also, it should be noted that the stress in the soil propagates radially and vertically from the point of EEV impact due to the compression of the soil as the EEV penetrates, meaning that while the surface soil feels large stresses, the sub-surface soil feels

no stress. It is not until the soil around the EEV has compressed significantly, and the EEV has traveled into the deeper areas of the soil that the stress at the bottom of the soil is nonzero. The progressive density change with compression through the soil can best be seen in the SPH density distributions of Fig. 45 and Fig. 47 in section 8.1.3.

As a consequence of using a less refined ALE mesh for the sake of increasing computationally efficiency, as well as maintain compatibility with the mesh of the EEV, there is minor ALE penetration of the Lagrangian part during later time steps. Due to the shape of the EEV geometry, there must be small elements in the center to ensure that the elements extending radially outward are not overly large towards the edge of the EEV. Therefore, there is a compromise between the element ratios of the central EEV elements and ALE elements and the outer EEV elements and ALE elements. This compromise, while it enables a more realistic contact in early time steps when on the nose of the EEV is in contact with the soil, begins to become less accurate as the outer edges of the EEV penetrate the ALE material. In order to compensate for this penetration in the results, the ILEAK formulation in the *Constrained_Lagrange_in_Solid card is used as an effort to account for this penetration. This card will consider the penetrated MMALE material in its force iteration calculations, helping the numerical data to be more accurate. This technique does not however change the visual error associated with this numerical phenomena.

A clearer picture of the relationship between peak acceleration and mass can be seen in Fig. 37

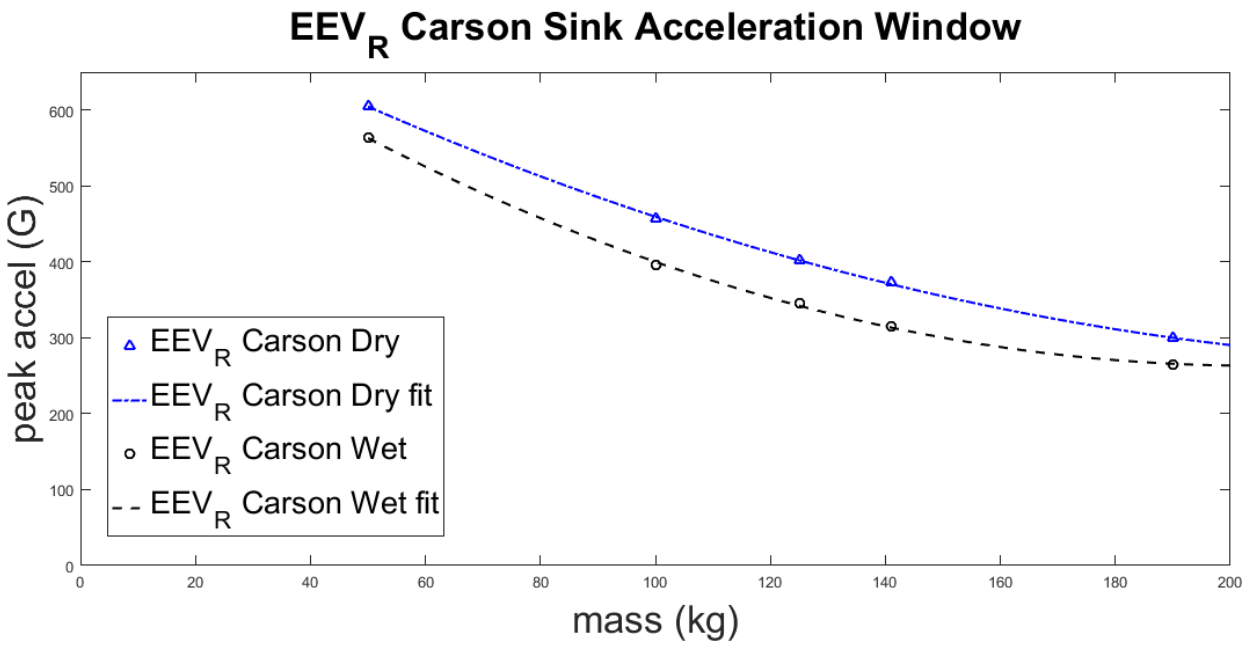

Figure 37. EEV peak z-acceleration as a function of EEV mass. The fit, shown as dashed lines, is a second order polynomial – Carson Sink

This trend obeys the laws of conservation of momentum in that a larger mass with the same velocity will require a larger impulse to decelerate it. Since larger masses penetrated deeper into the soil, taking a larger time to come to a stop, the impulse applied to them is larger than that applied to smaller masses which penetrate the soil significantly less. The fitting equations are derived through the linear fit of the peak acceleration plotted as a function of

$$\frac{DV^2}{M}$$

such that the peak EEV-R acceleration in Carsion Sink can be predicted using the equation and constants listed in Table 15.

Table 15. Carson Sink soil equation for peak acceleration

Carson Sink Soil	$A_{peak} = \alpha \frac{DV^2}{M} + C$	
	α	C
Carson Sink Dry	143.2	233.6
Carsib Sink Wet	146	179.3

The implication and limitations of fitting the peak acceleration data using this method are discussed further in 8.4.3. It should be noted that this relation is only valid for the range of mass, diameter and velocity in this study and does not show realistic acceleration estimations as these values approach zero due to the *C* value.

The effects of mesh refinement on the acceleration behavior was studied. Due to the larger computational expense required to run all mass cases using a refined mesh, a single mass case was used to examine mesh density effects. The original mesh was refined such that each element is divided into four elements for one simulation, then again for a second refined simulation. The effects of that refinement are seen in Table 16 and Fig. 38.

Table 16. Mesh convergence of MMALE Carson Sink Dry Soil

Refinement Level	Number of Elements	Peak Accel (G)	Percent Deviation
Original	2,000	665.73	-
Refined x 4	8,000	640.49	3.79 %
Refined x 8	16,000	626.13	2.24 %

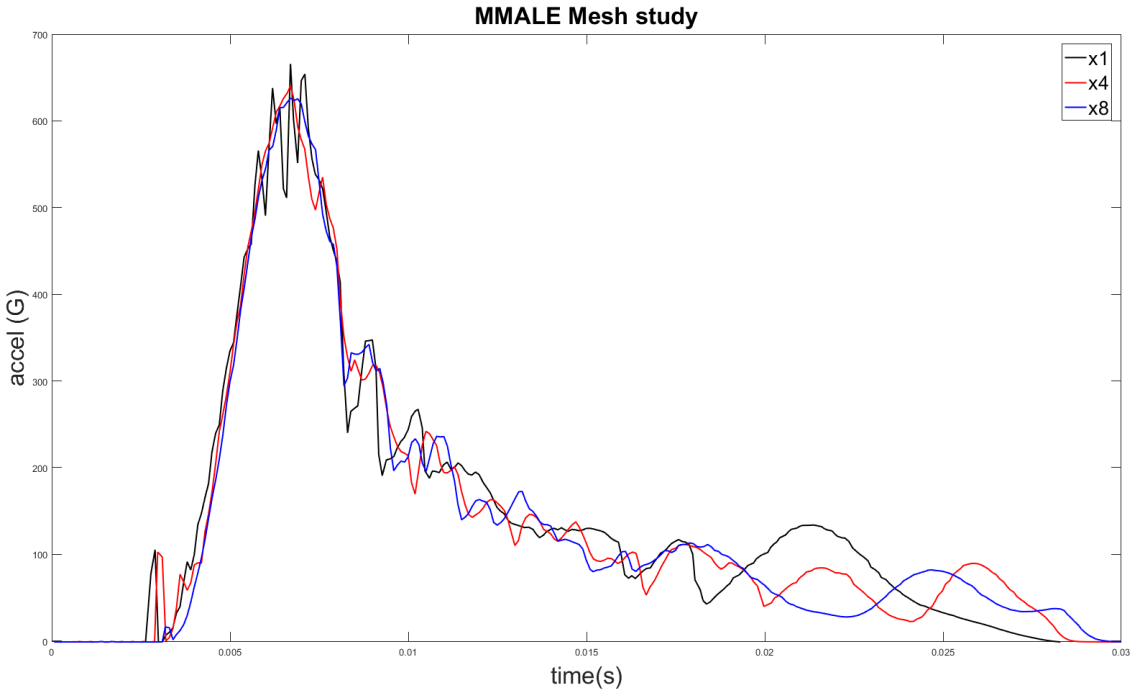

Figure 38. 50 *kg* EEV unfiltered z-acceleration curve for coarse (black) and refined x2 (red) and refined x4 (blue) mesh (Carson Sink Dry)

Based on the relationship between the three curves seen in Fig. 38 the refinement of the MMALE mesh shows a smoother acceleration curve without much of the noise that is present in the coarser meshed MMALE. Most crucially, the peak acceleration and overall acceleration trend between the three meshes is similar, and a relatively low convergence percentage is calculated, meaning that the mesh used shows a result very near the converged result.

A major behavioral difference is during later steps when the rate of change of EEV acceleration is less for more refined meshes, showing a smaller secondary acceleration peak. This is most likely due to the soil material's ability to deform across a more refined space rather than rely on fewer, larger elements to model deformation. The most effective visualization of this change is evident at the interface between surface and subsurface soils as the EEV moves

through it. A comparison of mesh refinements at this moment can be seen in Fig. 39.

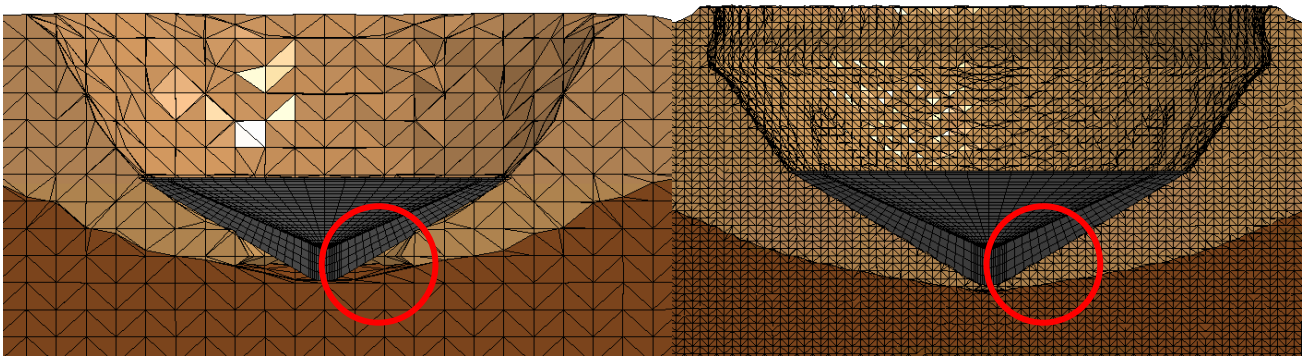

Figure 39. Comparison of soil deformation across mesh refinement (right frame has eight times more elements than the left)

The region of interest, highlighted in red, is shown to exhibit much higher fidelity and realism in the more refined mesh case (right) than seen in the less refined case (left). This occurs because the Eulerian mesh is more refined, and there are therefore eight times as many nodes within the same area unto which the material deformation can be mapped. This means that the simulation is able to show a much higher fidelity interface within the smaller area around the EEV nose and subsurface soil interface. As a result of this improved soil fidelity, the stress distribution is not only a larger magnitude at its maximum value, but also more accurately distributed through the soil. See Fig. 40.

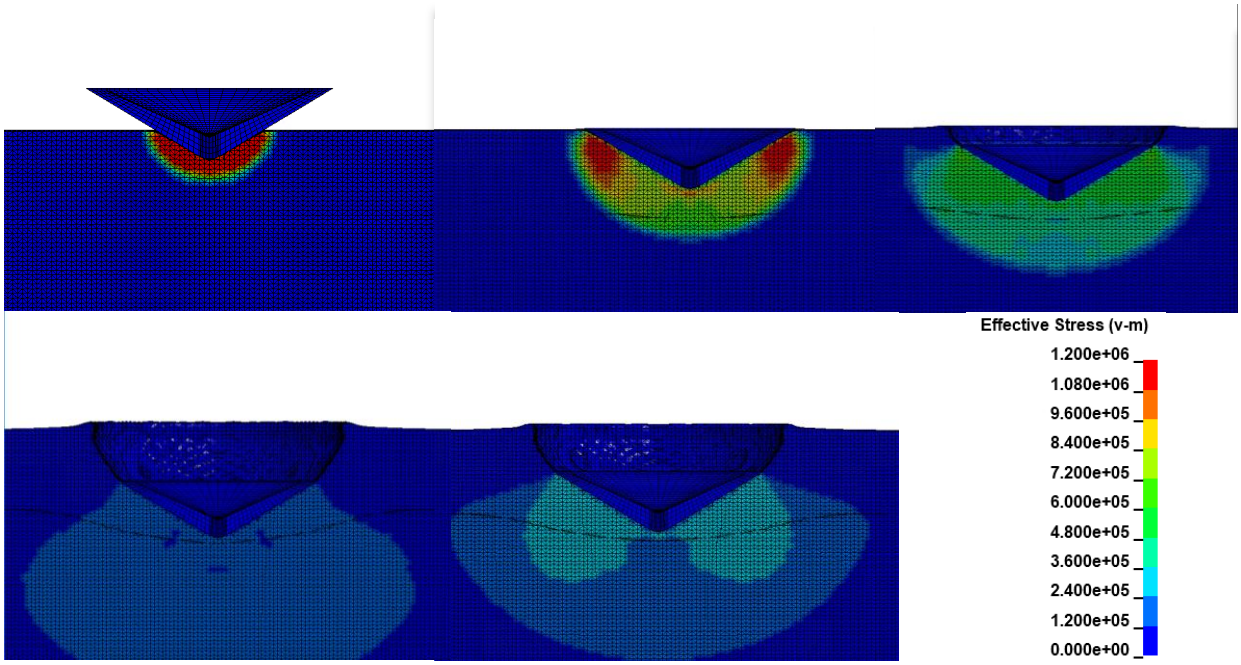

Figure 40. Von Mises stress (*Pa*) distribution through refined mesh Carson Sink soil during EEV-R impact

Based on the stress distribution shown in Fig. 40 (note the change in scale from Fig. 36, required to show a realistic distribution with larger peak stress value) there appears a loading of the EEV edges upon impact with the soil, as well as a more even stress distribution across the soil density change interface, which was not evident in the more coarse mesh density. The larger peak stress in the soil with refined mesh is a result of the improved contact between the EEV and soil due to improved element size ratio. Additionally, as previously shown in Fig. 39, there is an improved soil deformation fidelity at the EEV and soil interface, which results in a more even loading of the EEV by the soil. As a result of this, as the EEV nose passes the soil density change interface, the more even contact does not result in the same loading of the EEV outer edge as was present in the coarse mesh case. A direct result of this is the more accurate depiction of stress in the soil, extending across both soils and across the entire front surface of the EEV.

In addition to this improvement caused by mesh refinement, the artificial initial contact between the EEV and soil was drastically lowered through mesh refinements. This can be seen in Fig. 38 by the blue (most refined) curve at the instant that the acceleration becomes non-zero. It is clear that the refinement of the MMALE mesh greatly increases the realism of the physical behavior of the soil, and also decreases the numerical errors associated with a more coarse mesh.

Despite this difference, since the most crucial aspect of this study is to predict the maximum EEV acceleration, the late time acceleration differences between different meshes is negligible. Subsequent refinements significantly increase the computational time without drastically changing the peak acceleration in most cases. Based on these findings, it can be concluded that the acceleration curves in Fig. 33 are an accurate representation of the converged behavior of the simulation, meaning that for as long as the results are consistent with other numerical formulations, the currently used mesh density is a suitable compromise between a minimization of computational time and numerical errors and the accuracy of the peak acceleration and soil deformation. On an individual basis however, a more refined mesh would be desirable, when computation time is not a determining factor in mesh selection. It should be noted that part of the reason the more refined mesh is more accurate, is because the conservative contact parameters previously applied to prevent element penetration are no longer required in such magnitude due to a closer element size ratio between the MMALE and Lagrange elements of the two parts.

A similar mass variation process was performed for impact of the EEV-R into the provided Rosamond soil data. The acceleration as a function of EEV mass is shown for both saturations of soil in Fig. 41.

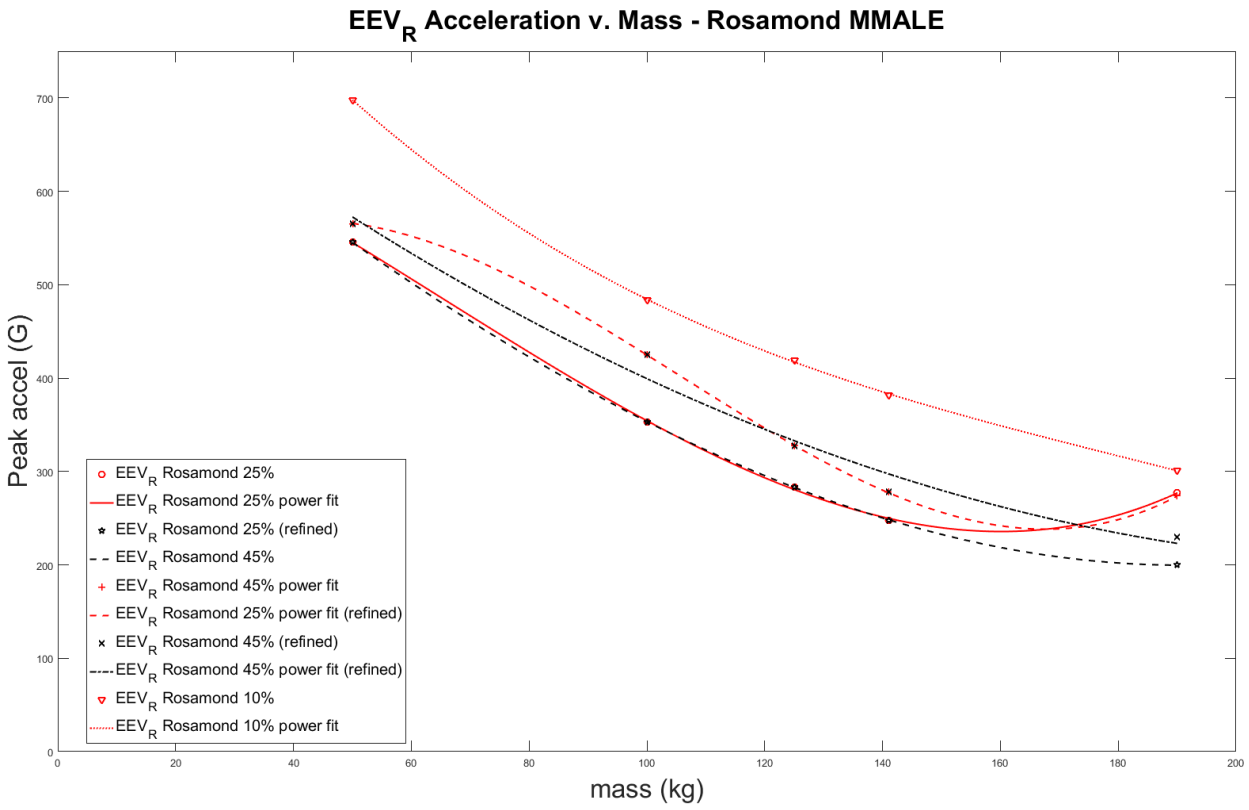

Figure 41. EEV-R peak impact z-acceleration in Rosamond soil

The peak EEV-R acceleration as a function of mass during impact into both Rosamond soils is fitted with a second order polynomial. Using this data, the peak acceleration of an EEV of similar geometry and impact velocity impacting in the Rosamond area can be easily predicted to be within the limits of the two curves. In the case of the 190*kg*, a more refined mesh was required in order to show similar results to the other simulations explored. These "refined" results are shown in black in Fig. 41. This estimate is further strengthened in its validity through the comparison of the Lagrange formulation results with the MMALE in Table 17.

Table 17. Comparison of MMALE and Lagrange acceleration results - Rosamond 25%

EEV-R Mass (*kg)*	Peak Acceleration, MMALE (G)	Peak Acceleration, Lagrange (G)	Percent Difference
50	545.35	549.99	-.85 %
100	353.12	359.03	-1.67 %
125	283.62	303.17	-6.89%
141	247.88	276.76	-11.34%
190	277.02	218.18	+21.24 %

Table 18. Comparison of Refined x8 MMALE and Lagrange acceleration results - Rosamond 25%

EEV-R Mass (*kg)*	Peak Acceleration, refined MMALE (G)	Peak Acceleration, Lagrange (G)	Percent Difference
50	524.58	549.99	-4.84 %
100	336.44	359.03	-6.64 %
125	286.03	303.17	-5.99 %
190	199.71	218.18	-9.25 %

Based on the information in Table 17, the MMALE results are consistent, within a reasonable amount of deviation, with the Lagrange results, yet show the largest deviation in the 190 *kg* case. This disparity shows the possible error associated with testing a relatively small EEV geometry with large mass impacting soft MMALE soil. In an effort to reduce this large error, the MMALE mesh was progressively refined for four different massed EEV-Rs, and the resulting converged results are shown in Table 18. The percent difference between the two numerical formulations is shown to drastically decrease to less than 10% error. This large change in peak acceleration when using MMALE over mesh refinements shows the importance of mesh density when modeling large deformation of soil under rapid loading. The larger error during the nominal mesh density is due to the inability of the relatively large elements to accurately model the large, rapid deformation, resulting in large amplitude acceleration spikes in the EEV

acceleration curve. Additionally, the elimination of the artificial initial contact was achieved. See in Fig. 42, for the comparison of the converged case to the original mesh density acceleration curve.

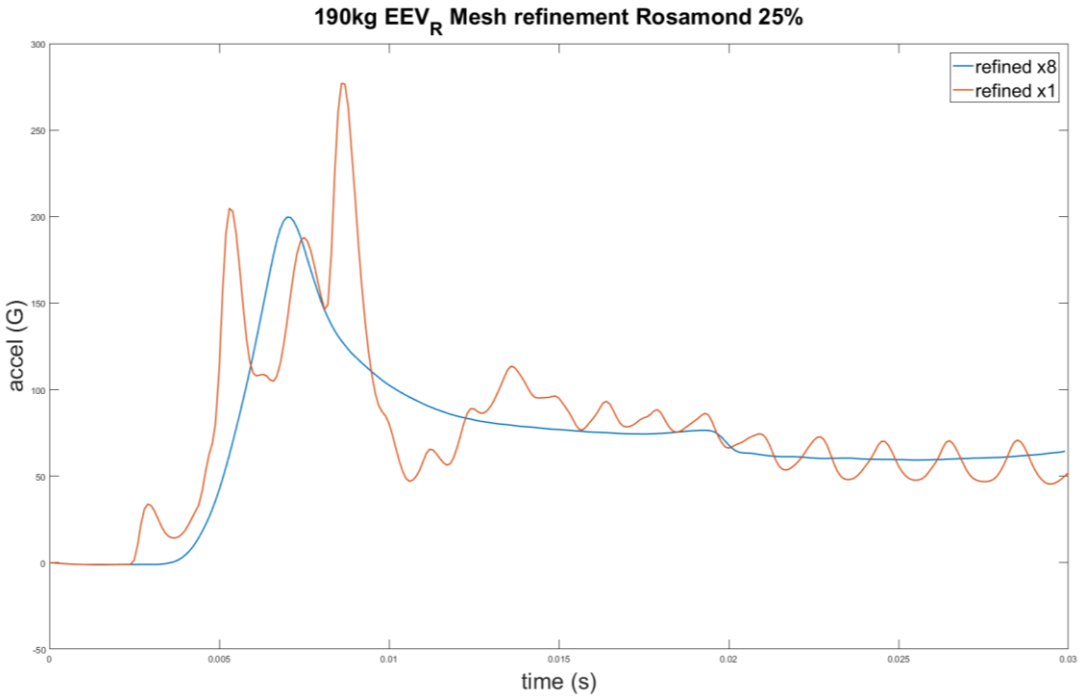

Figure 42. Mesh refinement of 190*kg* EEV-R filtered acceleration, Rosamond 25%

Comparing the two curves in Fig. 42, the large oscillations which are present in the nominal mesh density case are totally eliminated through the refinement of the MMALE mesh. The smaller elements allow for the more realistic, and higher fidelity deformation of the soil, resulting in a smoother curve, with no large spikes in acceleration. The difference in the results as they relate to the refinement of the mesh across all MMALE trials shows the importance of mesh study, and use of refined meshes, especially when large deformation is expected in the material. Note that the non-zero acceleration at .03s is a result of ending the simulation early for efficiency sake, all MMALE curves return to zero in all trials, as seen in Fig. 33.

Despite this occasional heavy reliance on mesh density, there were not the same hourglass effects and element distortions present in the MMALE that were characteristic of the Lagrange simulations. For this reason, MMALE formulation was continued to be used through other studies not concerned with determining element formulation dependence.

8.1.3 SPH

In order to gain a perspective on the feasibility and process involved in modeling the soil with SPH, a similar mass variation study was conducted using SPH elements. A unique benefit which makes SPH formulation intriguing is its ability to model the granular behavior of the soil. The unconnected particle elements of SPH allow it to deform significantly while maintaining element stability, without hourglassing effects. Difficulties associated with using of SPH over other formulations is enforcing boundary conditions and maintaining an acceptable computational cost. Additionally, SPH particles perform optimally at a 4:1, SPH to Lagrange element ratio. Ratios less than this can result in SPH penetration of Lagrange elements. This issue was diminished by creating the optimally sized Lagrange elements when possible while

still maintaining the geometry of the EEV. This problem was most prevalent at the nose of the EEV, where the elements must be the smallest in order to capture the curvature of the geometry.

A time-lapse of the SPH impact with Rosamond 25% is shown in Fig.43.

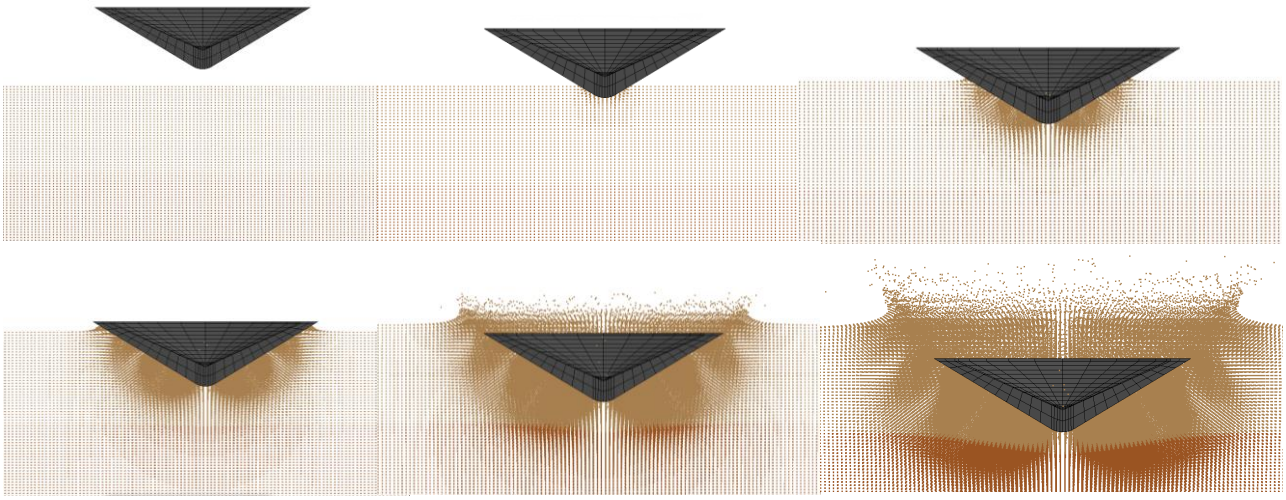

Figure 43. EEV-R impact with Rosamond 25% SPH soil

The ability of SPH to show the ejected soil particles is evident in Fig.43 in the later frames, as the EEV penetrates deeper into the soil. The splashing of the particles extending vertically, and radially outwards after the outer edge of the EEV penetrates the surface of the soil. This is better seen in Fig. 46 A buildup of particle density along the outer edge of the EEV is seen during later time steps as the soil compresses and moves along the sloped front of the EEV. See in region A of Fig.44. This buildup of soil will be first to be ejected from the impact area.

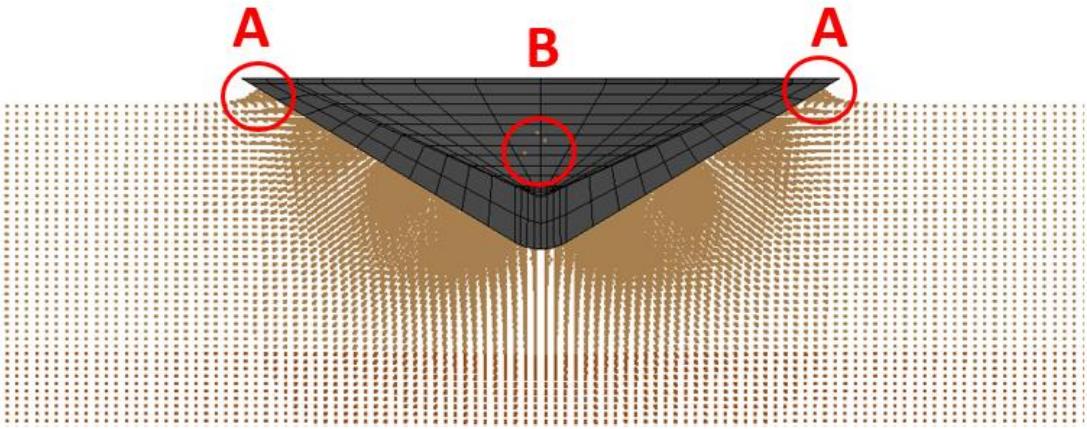

Figure 44. EEV-R impact with Rosamond 25% SPH soil regions of interest #1.

Region B in Fig.44 shows the penetrated SPH particles. This penetration occurs as result of the SPH to Lagrangian element ratio required to maintain relatively low computational efficiency by limited the density of the SPH and the small element size required to capture the EEV geometry. Both the increase in density along the outer EEV edge, and the penetrated SPH particles can more easily be seen in Fig.45.

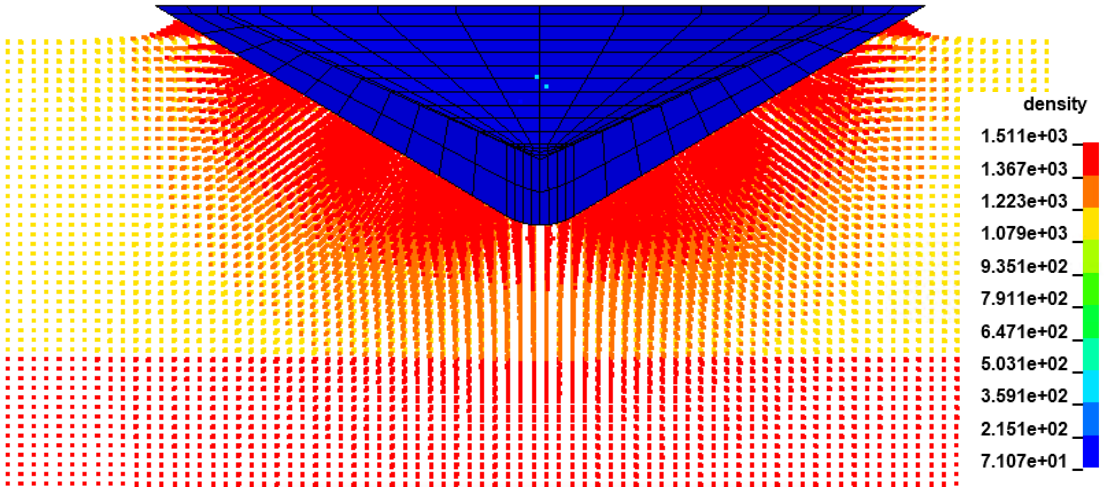

Figure 45. Soil density (kg/m^3) distribution EEV-R impact with Rosamond 25% SPH soil #1

There is clearly a larger density of SPH along select regions of the front of the EEV which include region A of Fig. 44 as well as region D of Fig.46.

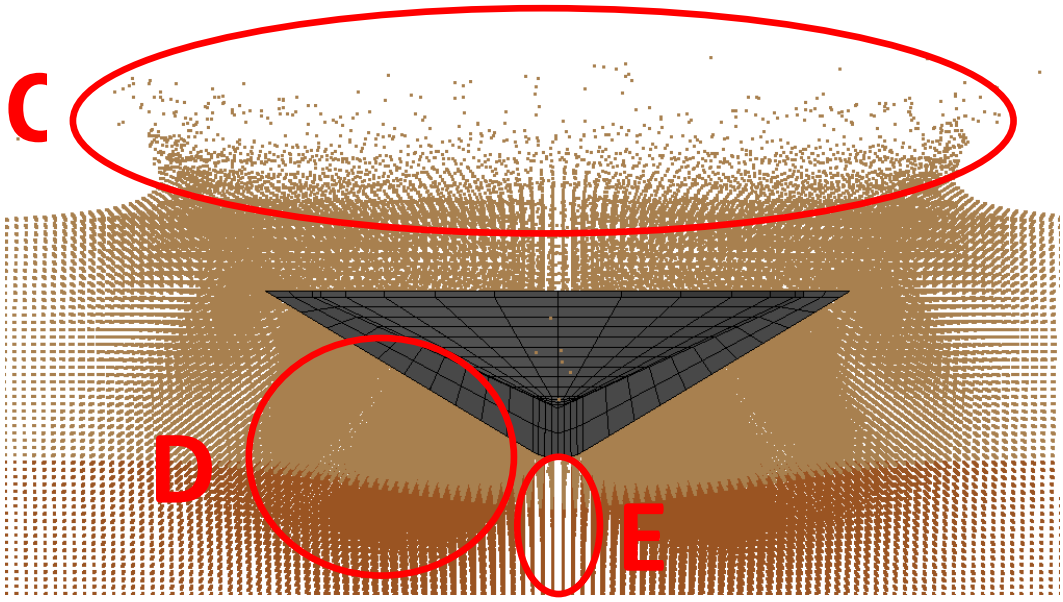

Figure 46. EEV-R impact with Rosamond 25% SPH soil regions of interest #2

The density of SPH from Fig.46 can better be observed in Fig. 47.

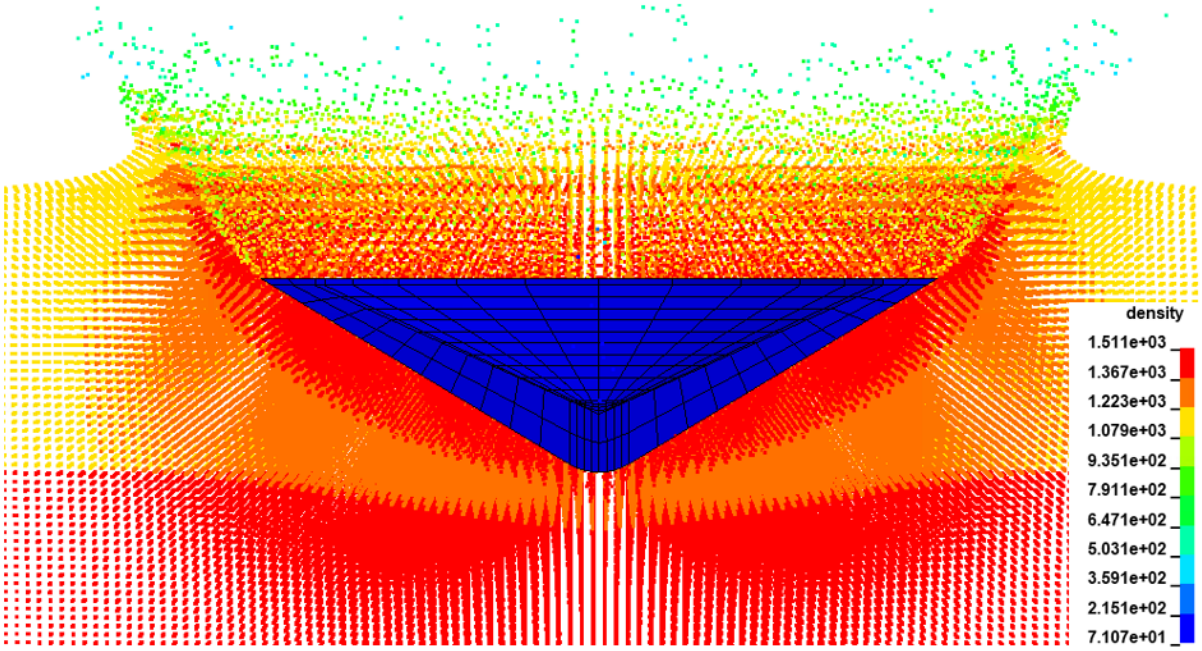

Figure 47. Soil density (kg/m^3) distribution EEV-R impact with Rosamond 25% SPH soil #2

The information in the previous figures shows that there is a compression of the soil which occurs mainly directly below the EEV, and begins to extend radially outward beneath the surface of the soil, as seen in region D. That is to say that there is very limited compression of the soil along the surface, rather, most of the compression occurs directly along the bottom surface of the EEV. It should be noted that this compression is radially uniform through the SPH, and occurs in all areas of the soil under the EEV. Region E is an area which, from the angle of the image, appears to not show particle compression, however this is a product of the image angle, and EEV geometry. Since above region E the EEV geometry has normals which are close to vertical, the SPH particles will only compress in the vertical direction, unlike those particles in region B, which are compressed both in the horizontal and vertical directions. Analyzing Fig. 47, this artifact of the SPH visualization is still present, however using the color of the particles in regions D and E, it can be seen that the density of particles across the boundaries of these two regions is continuous, proving that the seemingly uncompressed region E particles is only a result of the visualization of the SPH, and the direction in which they are being compressed.

Additionally, region C of Fig.46 and again in Fig.47 show the power of SPH in modeling the ejected soil particles as they are displaced by the EEV. Comparing Fig.44 and Fig.46, the SPH do not begin to be ejected from the impact area until the outer edge of the EEV passes the plane of the surface of the soil. As the SPH build up along the front of the EEV, they are progressively compressed, and pushed radially outward, until there is no longer a surface for them to be compressed by. The forcing of the soil particles radially outward results in the ejection of the soil. It is immediately evident that if any effort is made to better understand the behavior of the ejected particles as a result of EEV impact, or the effects of soil density change, SPH formulation would be the preferable method. SPH’s clear limitations restrict its capability

however as it has the potential to be extremely computationally expensive. As particle density is increased, it requires a specific Lagrangian element size in order for effective interaction, and it also poses challenges in applying boundary conditions to the SPH area. During this study, the SPH particle to Lagrange element ratio was determined to be approximately four SPH to every one Lagrange element, however this was made more difficult due to the varying Lagrange element size with varying EEV geometry, especially around the nose of the EEV. In an effort to improve the element ratio around this region, the SPH density was increased, yet this this results is significantly larger computational times. Since a uniform SPH particle density was used, increasing the number of particles for the sake of maintaining a perfect element ratio at the impact area resulted in a large increase in total SPH particles. This increased computation time to an inefficient size for use in a significant number of consecutive trials. In the simulations shown, along the EEV/soil interface where there was less than a 1:1 SPH to Lagrange element ratio, element penetration appears to occur much more frequently than at larger SPH densities. It is therefore advisable that under ideal conditions, the SPH field be made as dense as computationally possible in order to limit penetration, through the maximizing of the element ratios. Achieving this is not always practical however due to the significant computation cost that accompanies such SPH densities.

The acceleration curves for the EEV-R impacting with Carson Sink dry soil can be seen in Fig. 48.

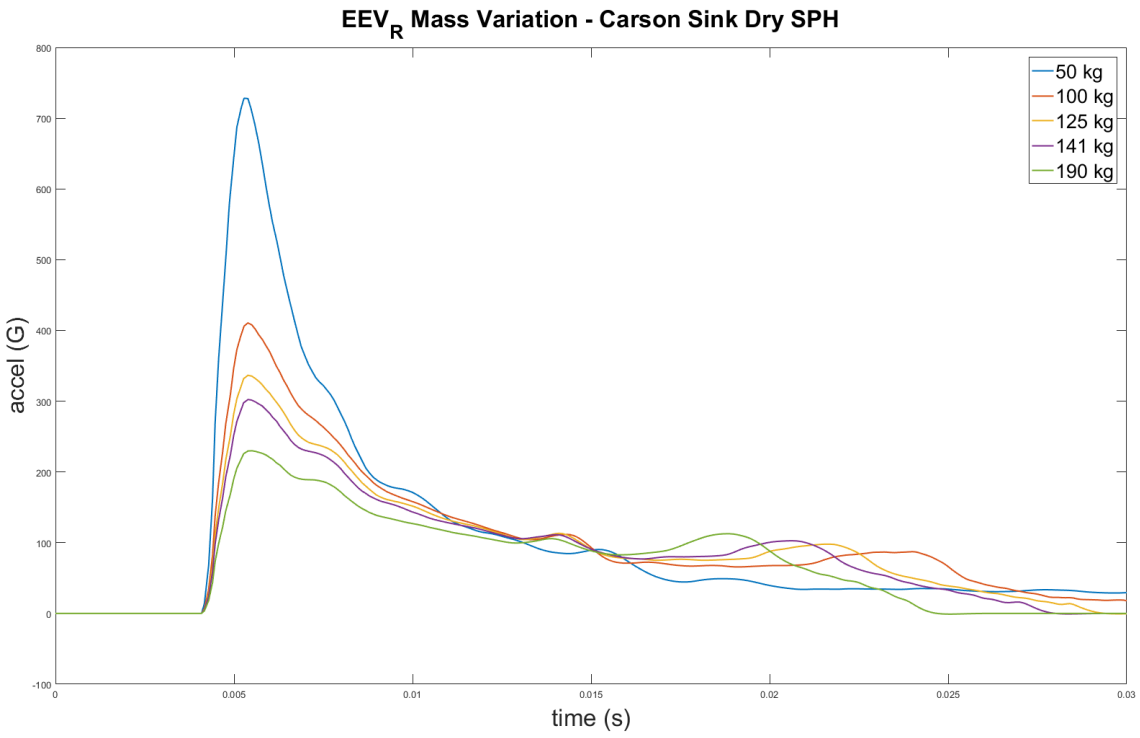

Figure 48. EEV-R z-acceleration over time impacting Carson Sink dry soil, SPH

The peak acceleration values are comparable to those measured using the MMALE formulation, in most instances. See Table 19.

Table 19. Comparison of SPH and MMALE acceleration results - Carson Sink Dry

EEV-R Mass (*kg*)	Peak Acceleration, SPH (G)	Peak Acceleration, MMALE (G)	Percent Difference
50	728.19	605.39	16.86 %
100	410.67	457.33	11.36 %
125	336.56	401.49	19.29 %
141	302.29	373.51	23.56 %
190	229.95	299.29	30.15 %

The SPH formulation was also used to model Rosamond 25% soil, and the acceleration curves over time for each EEV mass are shown in Fig.49

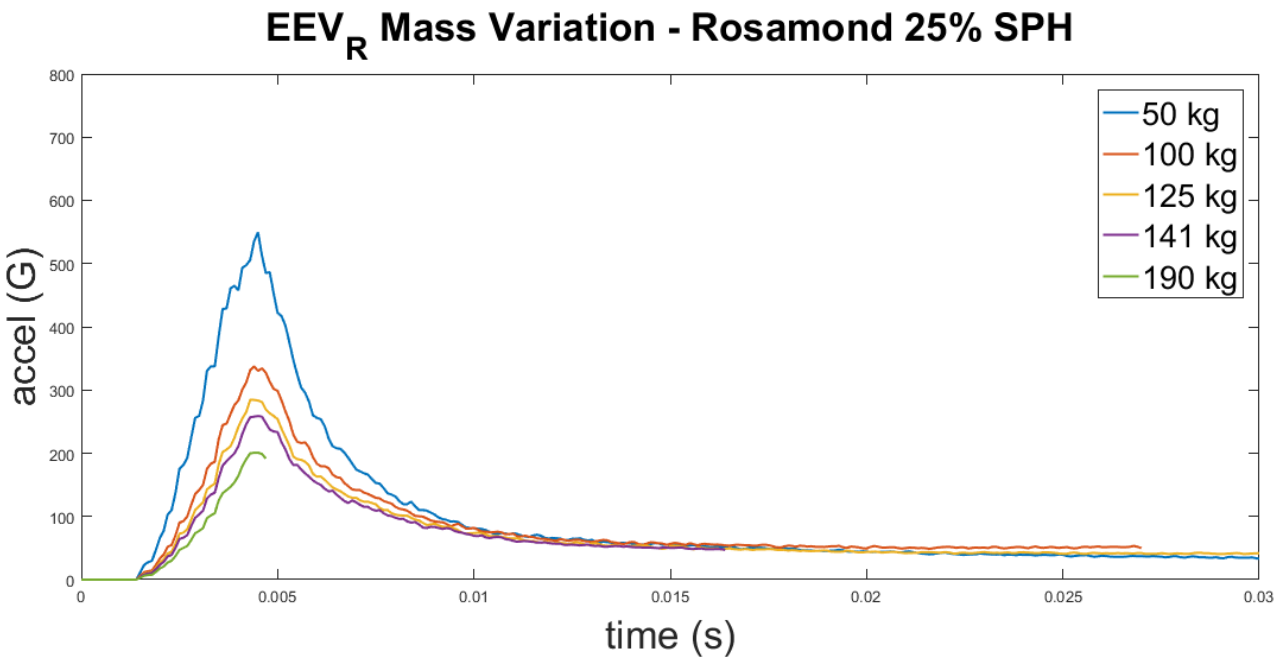

Figure 49. Unfiltered EEV-R z-acceleration over time impacting Rosamond 25% soil, SPH

The measured peak accelerations of the EEV-R during impact with Rosamond 25% SPH soil are summarized and compared with MMALE results in Table 20, with a refined MMALE mesh in Table 21, and compared with Lagrange results in Table 22.

Table 20. Comparison of SPH and MMALE acceleration results - Rosamond 25%

EEV-R Mass (*kg*)	Peak Acceleration, SPH (G)	Peak Acceleration, MMALE (G)	Percent Difference
50	549.43	545.35	+.74%
100	337.41	353.12	-4.66%
125	284.40	283.62	+.27%
141	258.92	247.88	+4.26%
190	200.82	277.02	-37.94%

Table 21. Comparison of SPH and refined x8 MMALE acceleration results

EEV-R Mass (*kg)*	Peak Acceleration, SPH (G)	Peak Acceleration, refined x8 MMALE (G)	Percent Difference
50	549.43	524.58	-4.74 %
100	337.41	336.44	+.227 %
125	284.40	286.03	-.571 %
190	200.82	199.71	+.556%

Table 22. Comparison of SPH and Lagrange acceleration results - Rosamond 25%

EEV-R Mass (*kg)*	Peak Acceleration, SPH (G)	Peak Acceleration, Lagrange (G)	Percent Difference
50	549.43	549.99	-.1%
100	337.41	359.03	-6.41%
125	284.40	303.17	-6.60%
141	258.92	276.76	-6.89%
190	200.82	218.18	-7.96%

Based on the summary of results above, there is clearly a strong correlation between the results of each element formulation, particularly in the case of Rosamond 25% soil. Most Rosamond 25% results are within less than 7% difference from each other, a similar trend to the comparison of MMALE and Lagrange formulations previously. Note that with further refinement of the MMALE mesh, a more acceptable percent difference between the different numerical formulations was achieved, this is discussed in more detail in section 8.1.2. A plot comparing the peak acceleration as a function of EEV-R mass across each numerical formulation, and MMALE mesh refinement is shown in Fig. 50.

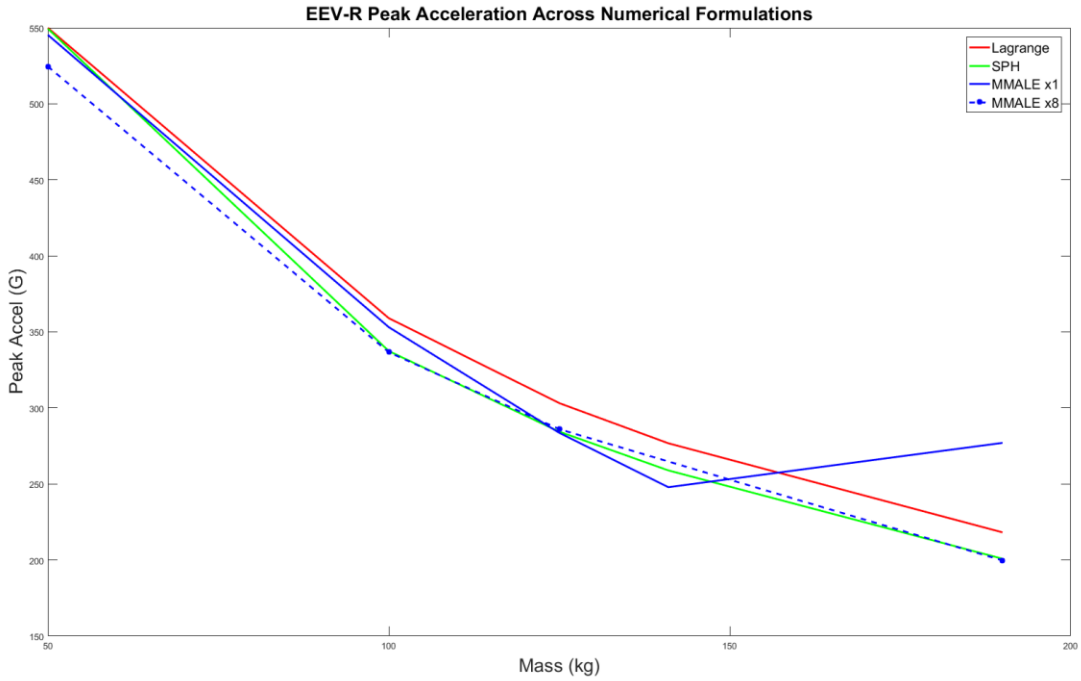

Figure 50. EEV-R peak acceleration as a function of mass for all numerical formulations and MMALE mesh refinement (blue dotted)

While the effects of each formulation's negatives continue to allow each to produce consistent results, MMALE requires the most efficient model creation process, and ease of rapid simulation generation. Seemingly equally as accurate both quantitatively to MMALE, the SPH formulation demands a long computational time, and must be generated specific to each scenario desired, further increasing total study time and complexity. Therefore, despite the similarities in results between element formulations, MMALE was used whenever able in place of other formulations.

8.2 Off-Nominal Impact Testing

Due to the reliance of the EEV on passive descent, the orientation of the EEV during Earth impact can only be controlled using the final commands to the MSR Orbiter before separation with the EEV, and with the geometry of the EEV. As stated previously, the geometry of the EEV is designed to maintain vehicle orientation during descent, but for the sake of maintaining sample isolation, off-nominal impact scenarios need to be considered in testing. In order to determine the dependence of peak EEV acceleration on velocity vector angle upon impact, a parametric study was conducted keeping the mass (50 *kg*) and effective velocity (40 *m/s*) of the EEV constant. The impact angle of the EEV relative to the normal vector of the soil surface was increased across several different cases. This scenario is referred to as velocity vector at impact variation. The occurrence of this mode of off-nominal impact would most likely occur as a result of wind around the drop area. If there is not wind during the descent, the geometry of the EEV would orient it for a perfectly nominal landing (assuming no gyration of the EEV), however this is unlikely. Wind around the drop area would result in non-vertical components of EEV velocity. The orientation of the EEV while moving through windy conditions would affect the magnitude of the applied wind force based on the effective area of the EEV normal to the wind vector. This means that at large inclination angles, the EEV would be more drastically effected by the force of the wind. This results in a non-linear wind effect on the EEV such that as the wind reorients the EEV, and changes its effective velocity, the wind's influence grows in magnitude as the effective EEV area increases with orientation angle. For this study, the effective EEV velocity was assumed to coincide with the local vertical axis of the EEV, such that the EEV nose and velocity vector were oriented along the same axis. This

scenario is a sample of possible velocity and orientation combinations as the local EEV axis and velocity vector would not necessarily always be parallel.

Another scenario of off-nominal impact which was investigated is when the vertical velocity component is the only non-zero velocity component, such that the velocity vector is perpendicular to the surface of the soil. During such an impact it is likely that the EEV will land slightly angled to one side from nominal. This would be due to the oscillations of the EEV's orientation as a result of aerodynamic forces during descent. In order to model this behavior, a deformable EEV was chosen in order to model the damage caused by impacting at extreme angles relative to the EEV's local vertical axis. This scenario is referred to as impact angle orientation variation. Graphics depicting each scenario are shown in

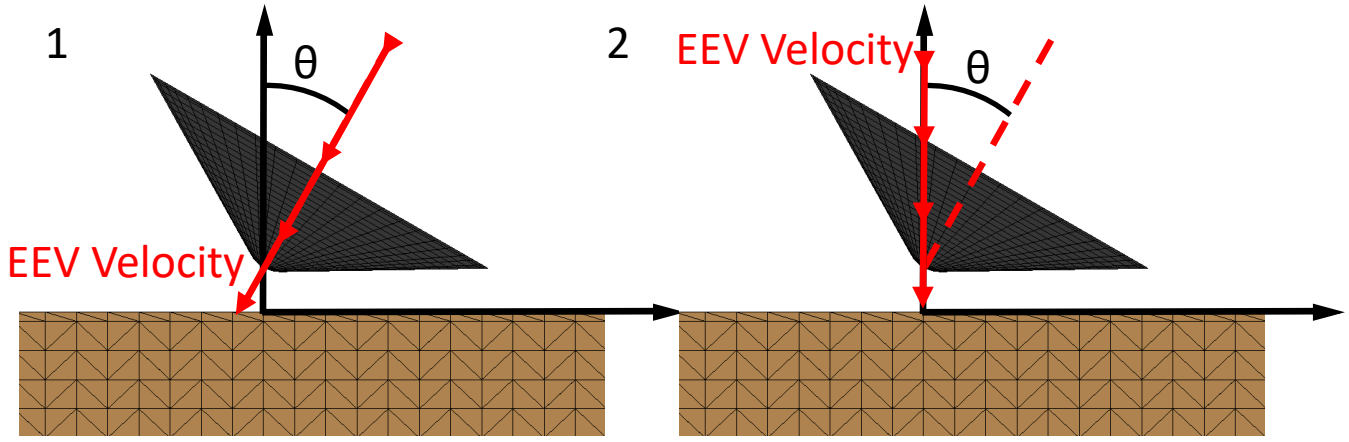

Figure 51. Velocity vector at impact variation (1) and impact angle orientation variation (2)

8.2.1 Velocity Vector at Impact Variation

The acceleration as a function of the impact angle of a 50 *kg* EEV can be seen in Fig. 52.

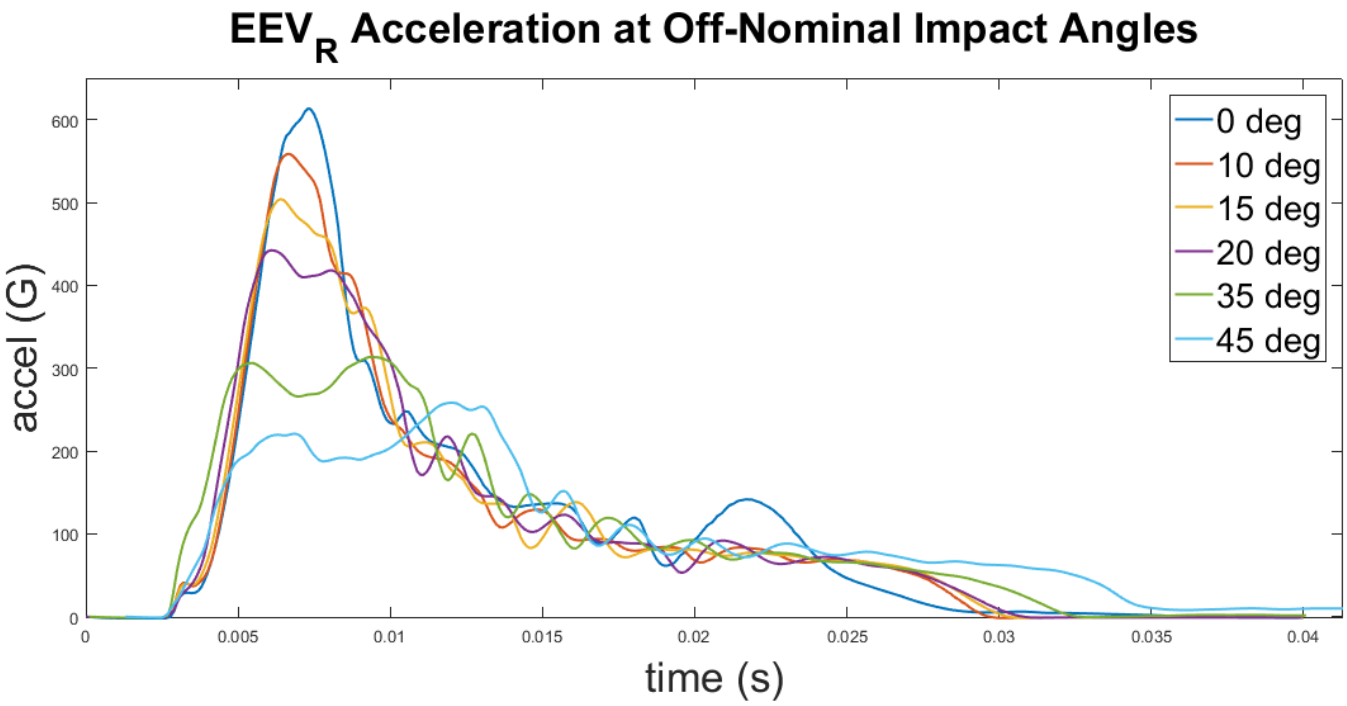

Figure 52. EEV-R resultant acceleration curve over time with the variation of the off-nominal impact angle – Carson Sink Dry

Based on the information in Fig. 52 the peak acceleration of the EEV is largest in the nominal impact angle case. This is most likely because during large angle impacts, the EEV doesn't come into direct interaction with the denser subsurface soil. Similar to the case of mass variation, the deeper penetration into the soil results inherently in the interaction of the EEV with denser soil, and results in larger accelerations in later time steps. At large angles, the EEV's impact energy is absorbed almost entirely by the less dense surface soil, resulting in a lower peak acceleration and longer period of applied force. A visualization of the peak acceleration as a function of impact angle can be seen in Fig. 53.

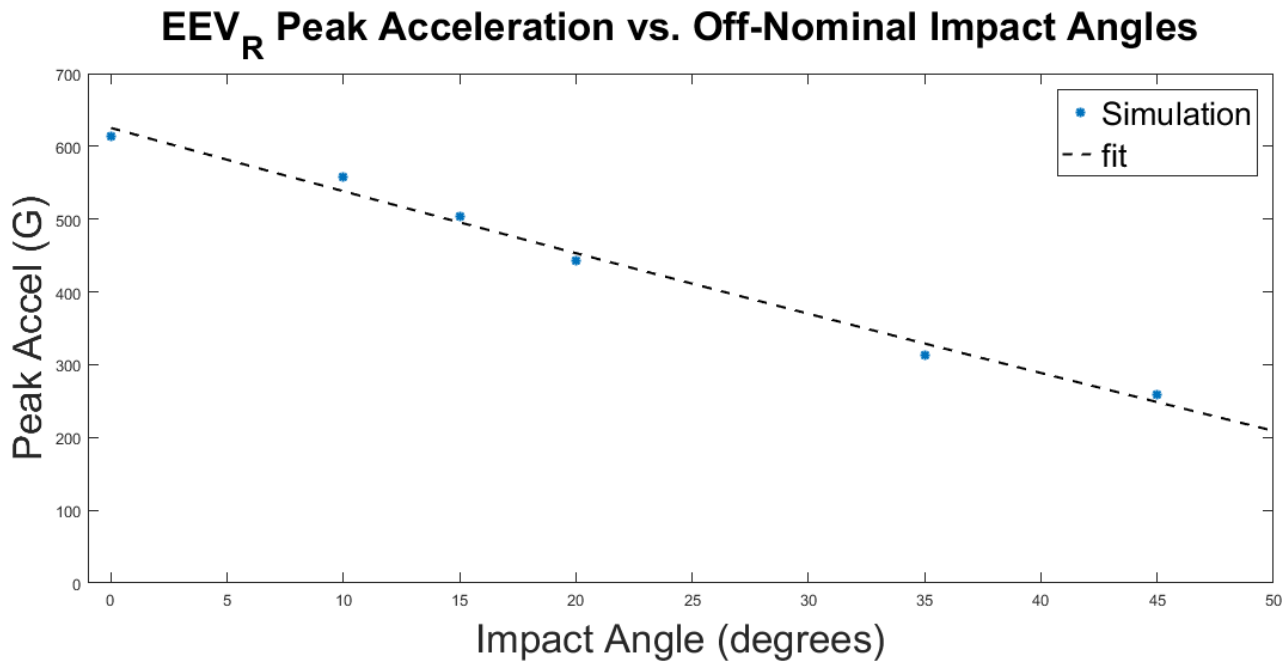

Figure 53. Peak EEV resultant acceleration as a function of impact angle – Carson Sink Dry

A quadratic fit was given to the data in Fig. 53 where peak EEV acceleration can be predicted.

$$A_{peak} = .0865\phi^2 - 12.99\phi + 666.44$$

Fig. 54 shows EEV penetration depth as a function of impact angle, corroborating the theory that the reduced EEV acceleration at higher impact angles is a result of the reduced interaction with the denser soil. The red line represents the depth at which the soil density changes, showing that the lower impact angles penetrate past that .203 *m* mark.

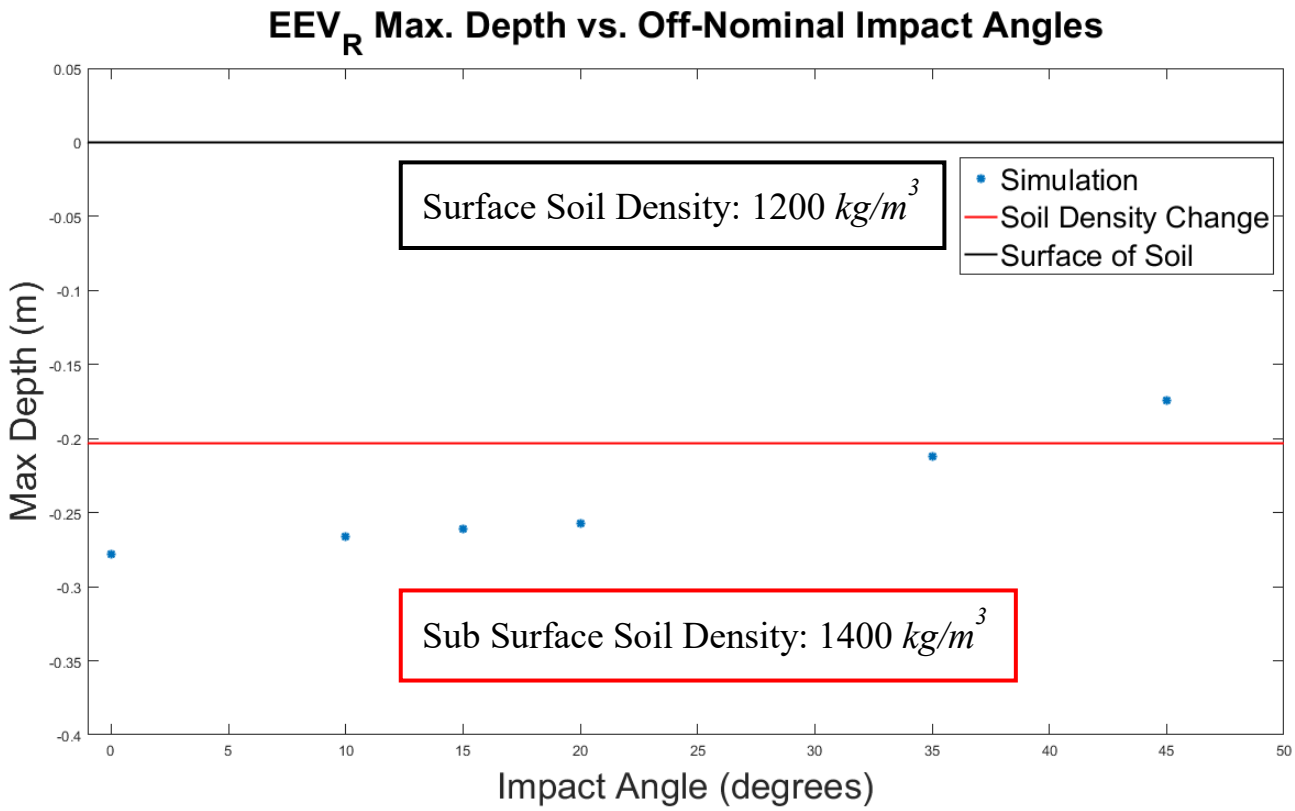

Figure 54. EEV penetration depth as a function of impact angle – Carson Sink Dry

While at first glance of these results it could be assumed that a large impact angle would provide more suitable EEV loading, more consequences of such an occurrence must be considered. During large angle impacts, the rotational velocity of the EEV is increased upon impact when a moment is applied to the EEV, expanding the possibility of multiple secondary ground impacts after the initial impact has occurred. The EEV is more likely continue moving from its initial impact area, traveling laterally along Earth's surface. A repercussion of increasing the surface area required for EEV deceleration increases the possibility of a collision with other materials in the area other than soft soil. This expands the risk of containment failure as a result of off-nominal material impact. A visualization of this effect can be seen in Fig. 55

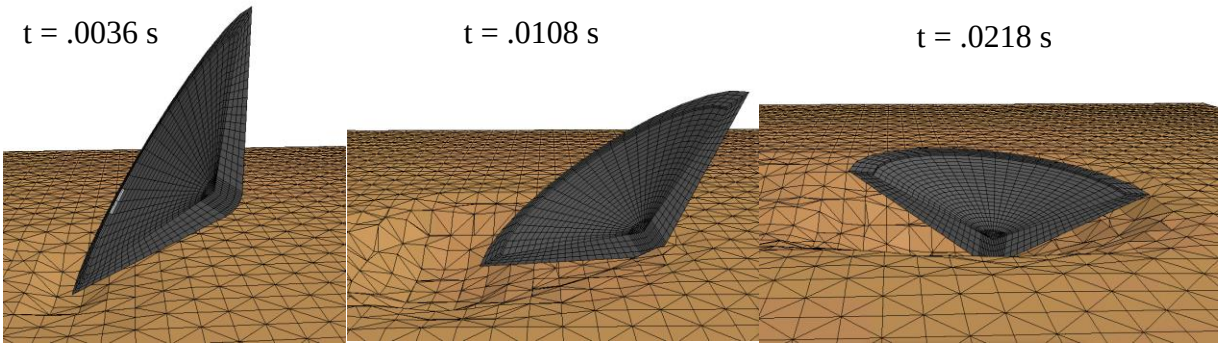

Figure 55. Timelapse progression of 45º off-nominal EEV impact with Carson Sink dry soil

The EEV orientation and large lateral velocity can justify the estimation that there is a large possibiliy of EEV tumlbing to occur as a result. In the third frame of Fig. 55 the leading rim of the EEV begins to make contact with the soil. During real life conditions and a possible non-uniform soil composition this EEV behavior could result in the flipping of the EEV after interaction with such an inconsistency. Therefore, maintaining an envelope of impact angles between 0 degrees and some impact angle where the benefits of low angle impact no longer outweigh the risk of secondary impacts as a result of tumbling.

8.2.2 Impact Angle Variation

In the likely event that the EEV lands slightly off axis from nominal, the loading on the outer wing will increase, and the overall loading and induced moment during landing will change based on the impact angle. In order to model this possibility, a deformable EEV-R model was used. The possibility of EEV failure is much larger during this mode of impact due to the excessive loading of the EEV wing. A restriction of using a deformable material for the EEV is that the EEV's mass cannot be modified, and therefore the nominal mass of the EEV-R, 12.5 *kg*, is used. Rotating the EEV through each case from the nominal angle of 0º to an extreme angle of 40º, the velocity is maintained at a constant 40 *m/s* in the downward direction. Initially, the data

was filtered using the same filter criteria as in previous trials. The filtered results are plotted in Fig.56.

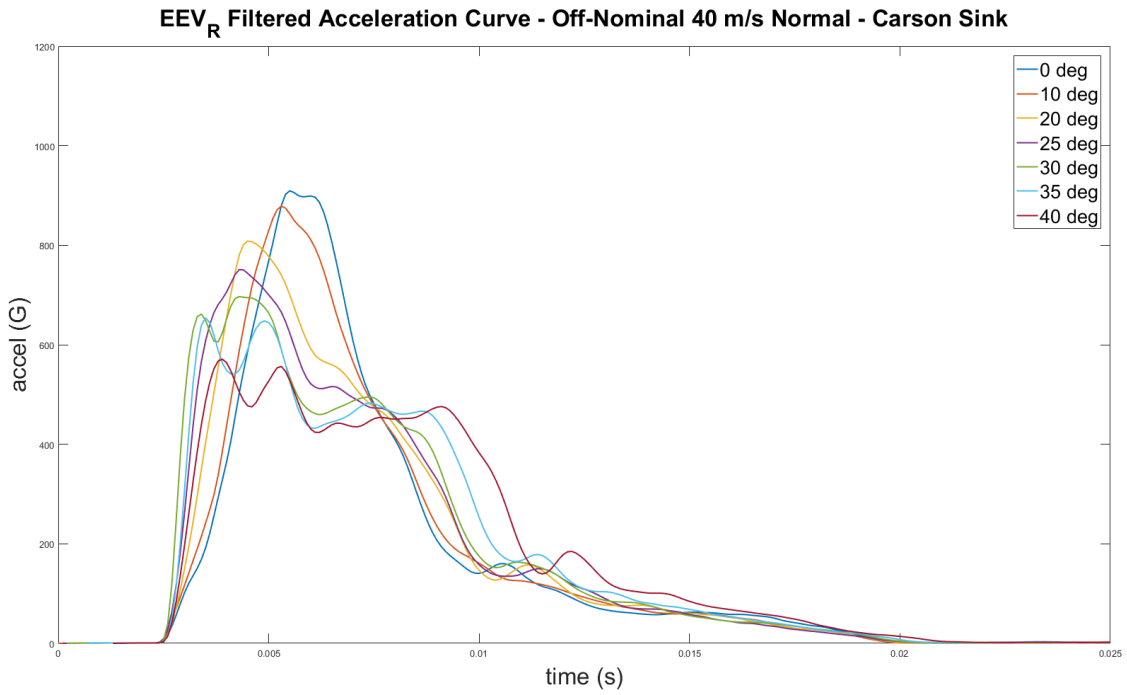

Figure 56. EEV-R off-nominal filtered resultant acceleration curves – Carson Sink dry

Through further examination of the simulations, it was predicted that there should be a large acceleration spike occurring at the critical inclination of the EEV such that a maximum surface area is impacting the soil surface at one instant. This occurrence was not evident in the filtered data, therefore the filter was removed, resulting in a drastically different behavior. A sample of three filtered curves and the same curves, unfiltered, can be seen in Fig.57 and Fig.58 respectively.

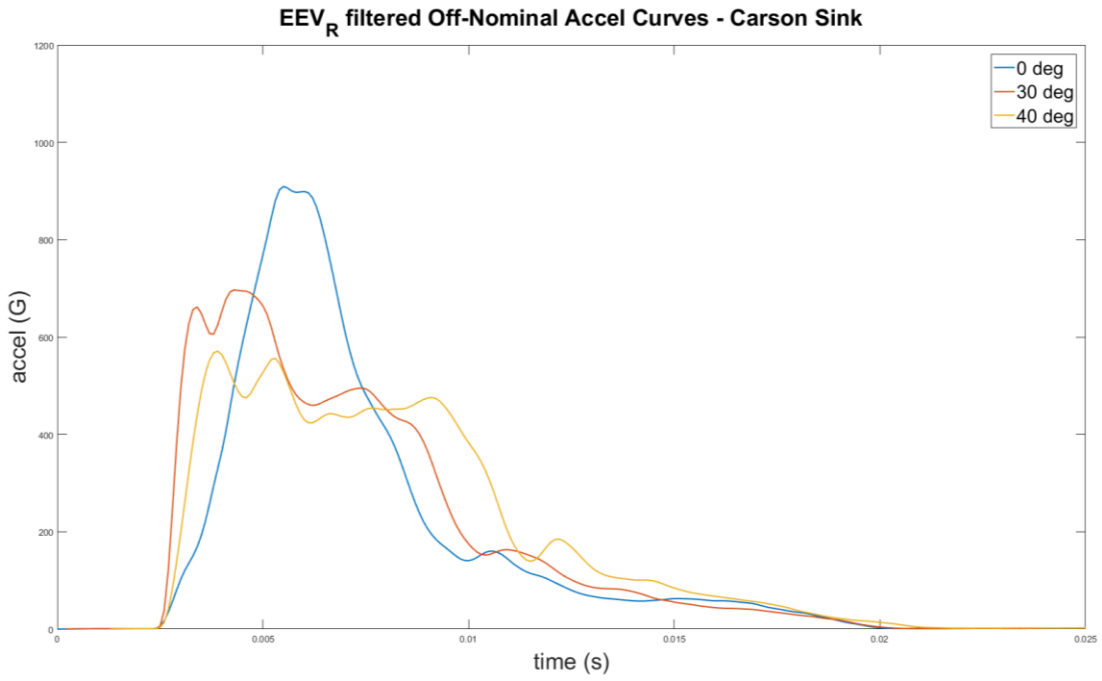

Figure 57. Three sample EEV-R filtered resultant acceleration curves

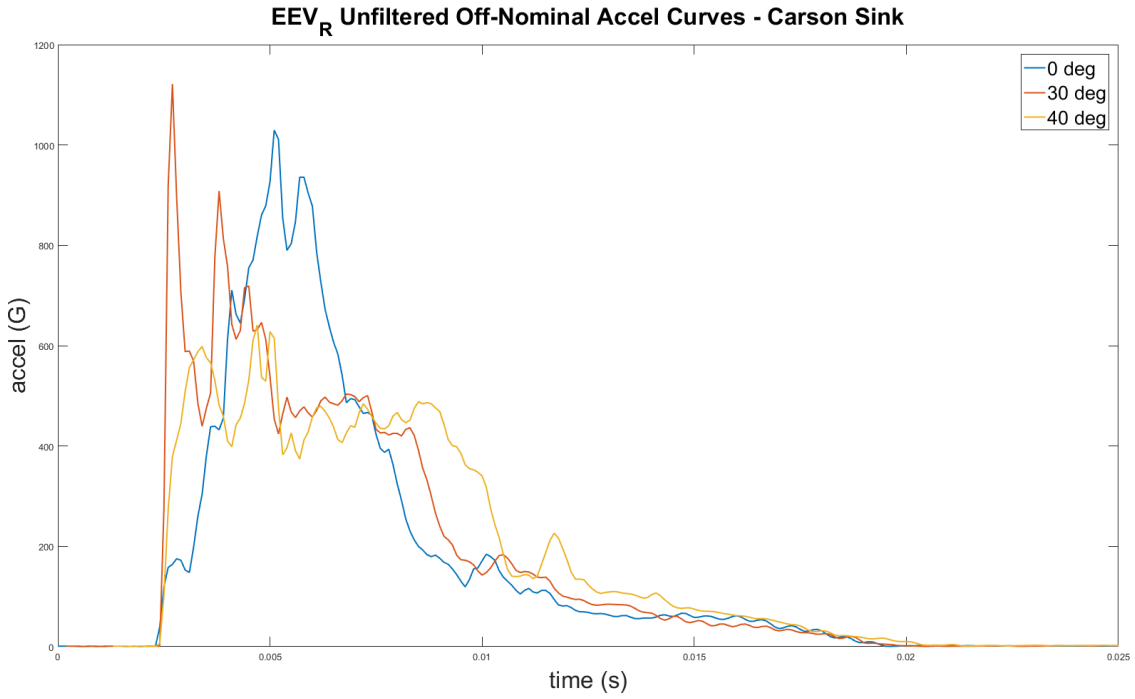

Figure 58. Three sample EEV-R unfiltered resultant acceleration curves

The drastic spike in acceleration in the 30º case is a characteristic of the EEV geometry, and should not be ignored through the filtering of the data. Since the inclination angle of the EEV wing is approximately 60º, the largest acceleration of the EEV is experienced at an inclination angle of 30º from the vertical axis. This occurs because it is at this inclination that the EEV sloping wing impacts flat with the surface of the soil, and the largest possible surface area of the EEV impact with the soil surface at one time. See an example in Fig. 59.

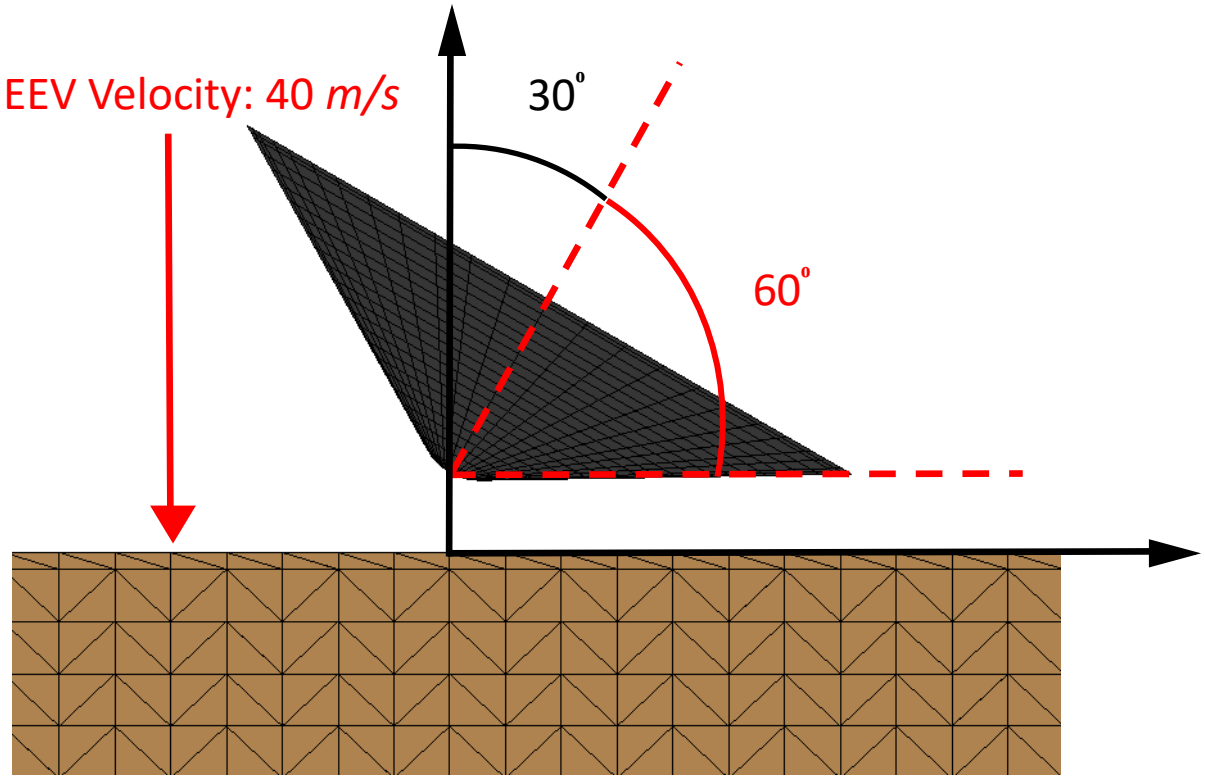

Figure 59. EEV-R off-nominal impact at 30. MMALE Carson Sink dry soil

This results it a dramatic spike in the acceleration versus angle function. The uniqueness of angles approaching 30º can be clearly seen in the comparison of the filtered and unfiltered peak acceleration in Fig.60.

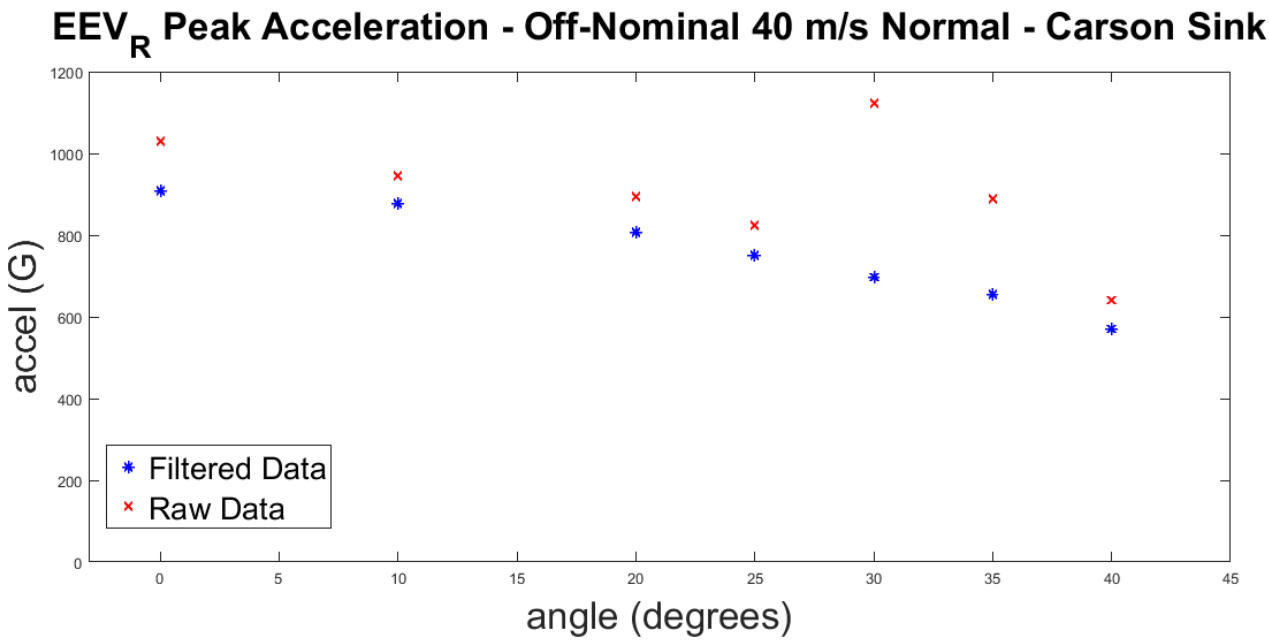

Figure 60. Off-nominal EEV-R peak resultant acceleration as a function of EEV-R orientation angle at impact

The reasoning behind the inclusion of the unfiltered peak acceleration values is further corroborated by the results of EEV penetration depth, shown in Fig.61.

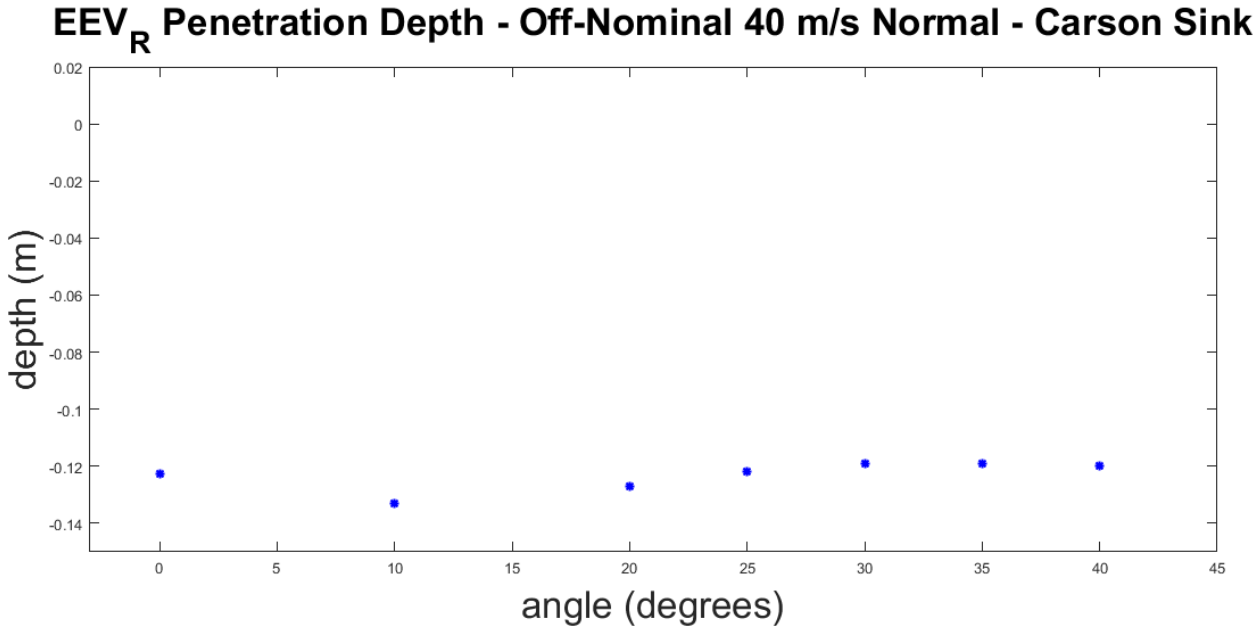

Figure 61. EEV-R penetration depth as a function of orientation angle at impact

It should be noted that there is significantly lower penetration than in previous EEV-R Carson Sink trials due to the lower mass of the EEV-R.

A summary of the depth and acceleration results is displayed in Table 23.

Table 23. Summary of EEV-R impact orientation variation

EEV orientation angle (degrees)	Penetration Depth (m)	Filtered Peak Accel (G)	Unfiltered Peak Accel (G)
0	.1225	909.39	1029.6
10	.133	878.42	943.9
20	.127	808.32	895.0
25	.122	751.06	823.6
30	**.119**	**696.80**	**1121.3**
35	.119	653.99	889.9
40	.12	570.95	641.2

There is minimum penetration at an impact orientation of 30**º**. Based on previous conclusions regarding the inverse relation between penetration depth and peak acceleration, hints that a maximum peak acceleration should occur at 30**º**, as recorded in the unfiltered data column.

In order to gain a perspective on the effects of the effective surface area of the EEV (the cross-section of the EEV in the same plane as the soil surface), it was plotted against peak acceleration in Fig. 62.

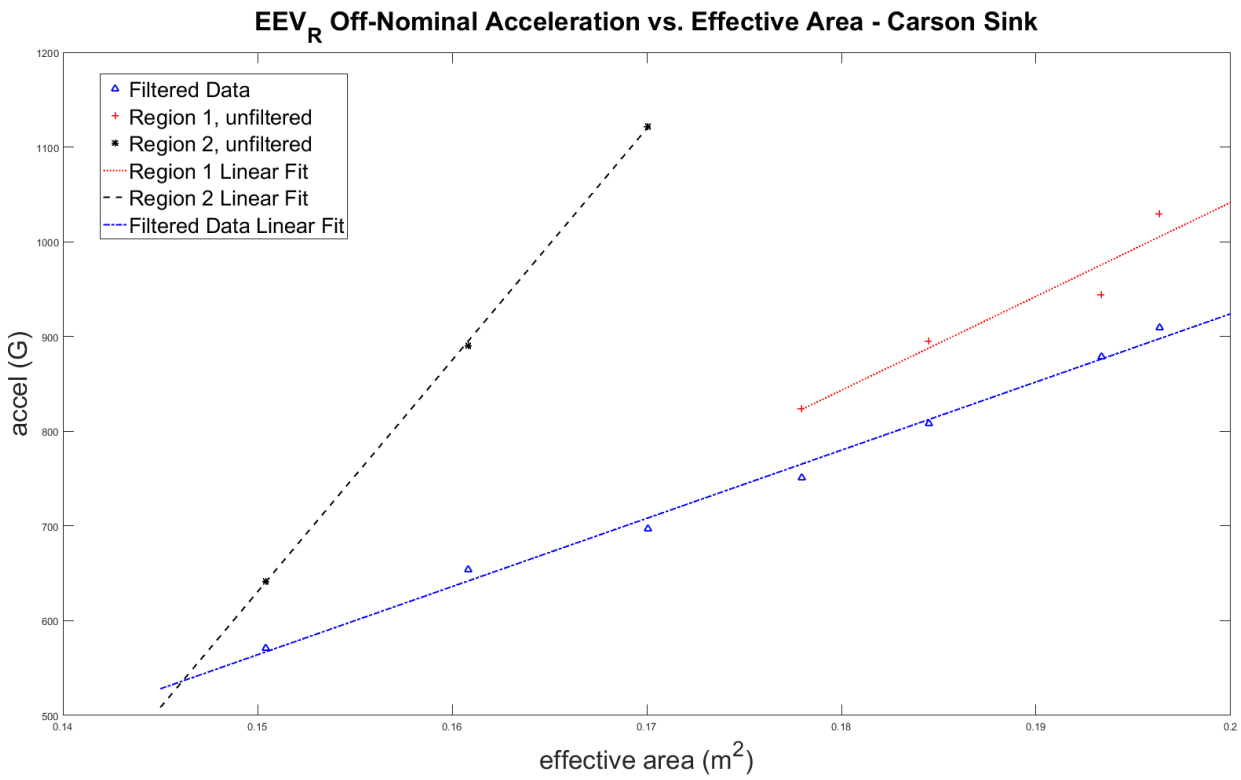

Figure 62. EEV-R effective acceleration as a function of effective area during off-nominal impact

Based on the data shown in Fig. 62, the large disparity between filtered and unfiltered data can be seen, in addition to the behavior of the two regions in the unfiltered data. These two regions, consisting of region 1, showing the behavior at smaller effective areas, and region 2, encompassing the nominal case, to the critical case. These two regions obey significantly different linear fits which can be modified to be dependent on the EEV total radius, r, and inclination angle, θ, can be seen in the equations below.

$$\begin{Bmatrix} \text{Region } 1 - \text{for } \theta < 30^0, & A_{peak} = 9913(\pi r^2)\cos(\theta) - 941.1 \\ \text{Region } 2 - \text{ for } \theta \geq 30^0, & A_{peak} = 24450(\pi r^2)\cos(\theta) - 3037 \end{Bmatrix}$$

where the effective area, a_{eff}, is,

$$a_{eff} = (\pi r^2)\cos(\theta)$$

This relationship shows how the behavior of the peak acceleration drastically changes after passing the critical case. This is largely due to the ability of the EEV to roll after impact at the larger inclination angles. Rolling allows for the distribution of impact energy over a larger area of the EEV, over a longer amount of time, resulting in lower peak accelerations. This rapid decrease in peak acceleration with larger angle can be seen in region 2. Before the critical angle, there is a much less rapid decrease in peak acceleration with changing effective area because during this time the initial impact of the EEV with the soil occurs around the curved nose of the EEV, only allowing for this small area to contribute the rolling behavior. During this time, the EEV can roll a maximum of 60^0 before crossing the vertical axis. It is after the critical inclination that almost the entire front surface of the EEV is allowed to come into contact with the soil during rolling, greatly increasing the rolling time, and maximum rolling angle before crossing the vertical axis, to 90^0. There is a limit to this relationship however which is dictated by the geometry of the EEV. As the inclination angle of the EEV is increased, there is more peak initial load applied to the outer edge of the EEV, which is applying a force for which this section of the EEV is not designed to absorb. Additionally, there exists yet another critical angle, most likely around 90^0 at which the EEV will no longer roll across only its front area after initial impact, but would possibly roll onto its back, resulting in unintended loading of the EEV rear. This is therefore important to recognize that these equations are only valid for orientation angles less than 90^0.

In all cases except for nominal impact and values around a $30^{\mathbf{o}}$ impact, the peak acceleration is lower because the EEV is allowed to roll as it impacts, distributing and slowing the rate of loading. There exists some orientation angle between nominal and $30^{\mathbf{o}}$, at approximately $29^{\mathbf{o}}$, such that the EEV will experience the lowest amount of acceleration, as the

maximum amount of rolling can occur, and a minimal amount of EEV surface area will initially impact the soil. While the passive descent design of the EEV does not allow for the active control of the EEV orientation during freefall through Earth atmosphere, the design can be optimized such that impact will occur within some orientation window with confidence. Based on the data collected, it would be advisable to design the vehicle to maintain a window of 15^{0} from nominal for impact in order to to maintain a factor of safety of 2.

8.3 Testing of EEV-CP300

8.3.1 JPL Penetrometer Test Validation

The main objective of this section is to not only show the behavior of a much larger EEV than that of the EEV-R, but also to recreate EEV accelerometer data recorded during impact testing performed at JPL. An accurate estimate of this test further validates the methodology used for previous simulations. The data recorded at JPL was taken during the impact of a 141 *kg* EEV with approximate dimensions of the CP-300. The EEV impact velocity was estimated to be 44.6 *m/s*. Surface soil and sub-surface soil density was measured to be 1321.5 kg/m^3 and 1662 kg/m^3 respectively where the soil saturation was 31 % saturated. In order to create the most accurate approximate soil parameter estimate, the Rosamond 25% soil parameters were used as these parameters are the closest set of inputs available for a 31 % saturated soil. The densities of both surface and sub-surface soil were altered to match the exact experimental setup.

Lagrangian

Initially a Lagrangian element formulation was used for the soil elements, but as with the simulations ran for previous scenarios using Lagrangian elements, the hourglassing of the elements was found to cause an unrealistic acceleration curve, seen in Fig. 63.

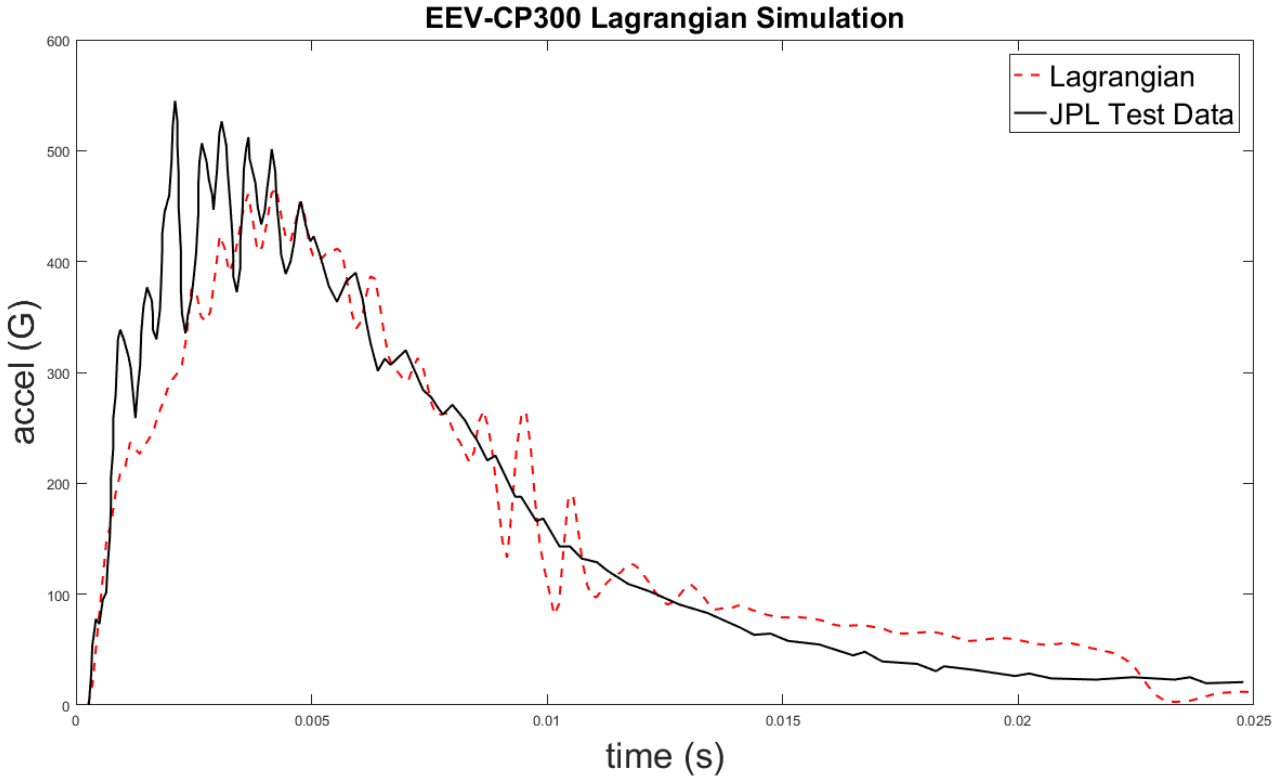

Figure 63. Lagrangian simulation CP-300 z-acceleration (dotted red) compared to JPL test data (solid black)

There is a 14.5 % error between the two peak accelerations. The simulation measures a maximum value of 466.27 *G* whereas the physical test measured 544.9 *G*. This underestimation of experimental data, if found to be a pattern across all physical test cases, would be detrimental to the design process of the EEV by providing a lower peak load prediction than is physically present, opening an opportunity for EEV failure. Additionally, the initial loading curve of the Lagrangian simulation is clearly not steep enough to match the test data, and the over estimation of late impact loading due to element hourglassing is still present. Due to these defects in the simulation results, and the previously seen stability of MMALE elements, further simulations were preformed using MMALE.

MMALE

In order to compare the qualitative success of MMALE, a frame by frame of the high speed impact video of the test can be seen in Fig. 64 and Fig.65.

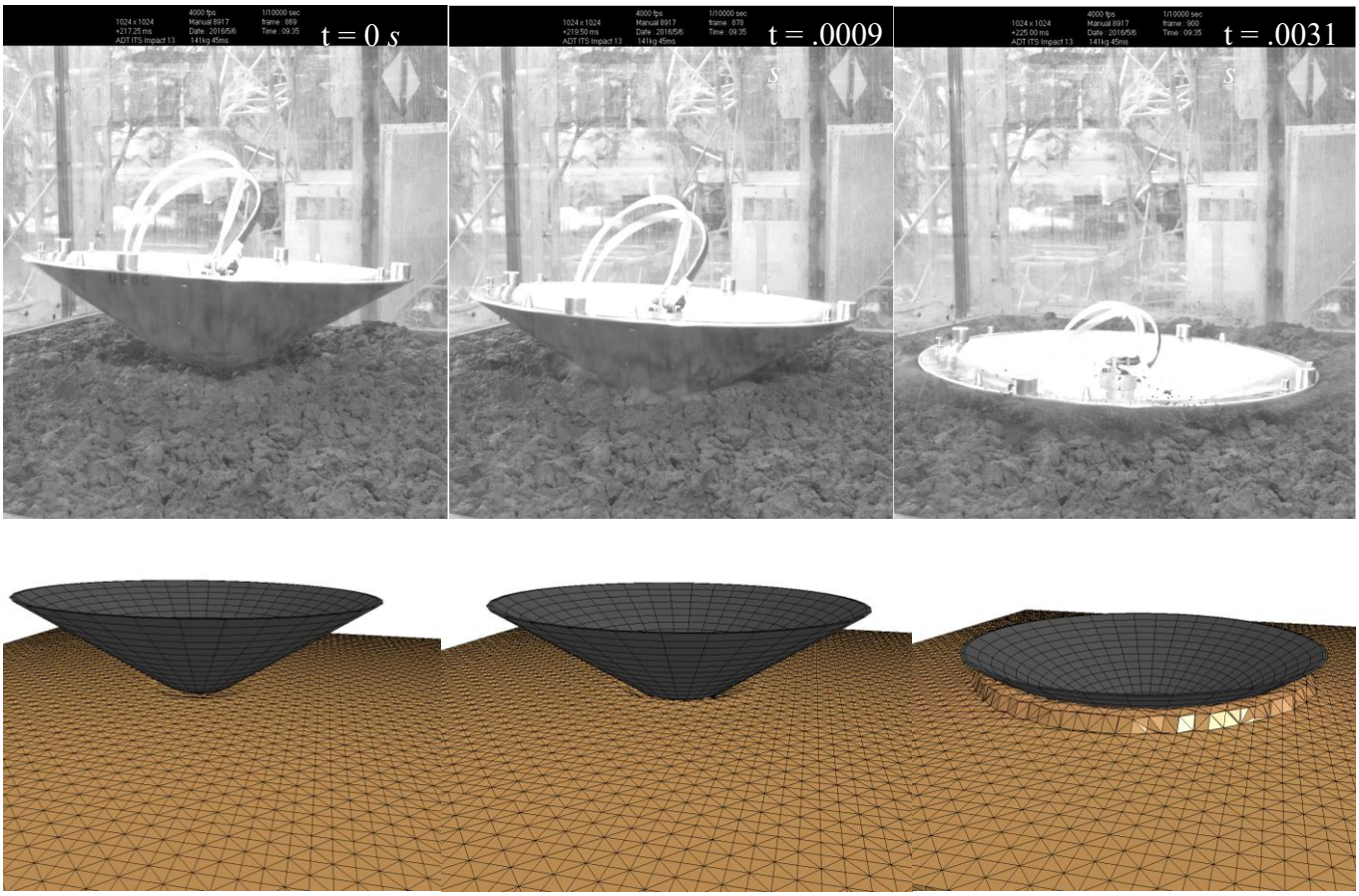

Figure 64. Time-lapse of CP-300 impact test into Rosamond soil, courtesy of JPL, compared with MMALE simulation. Part 1

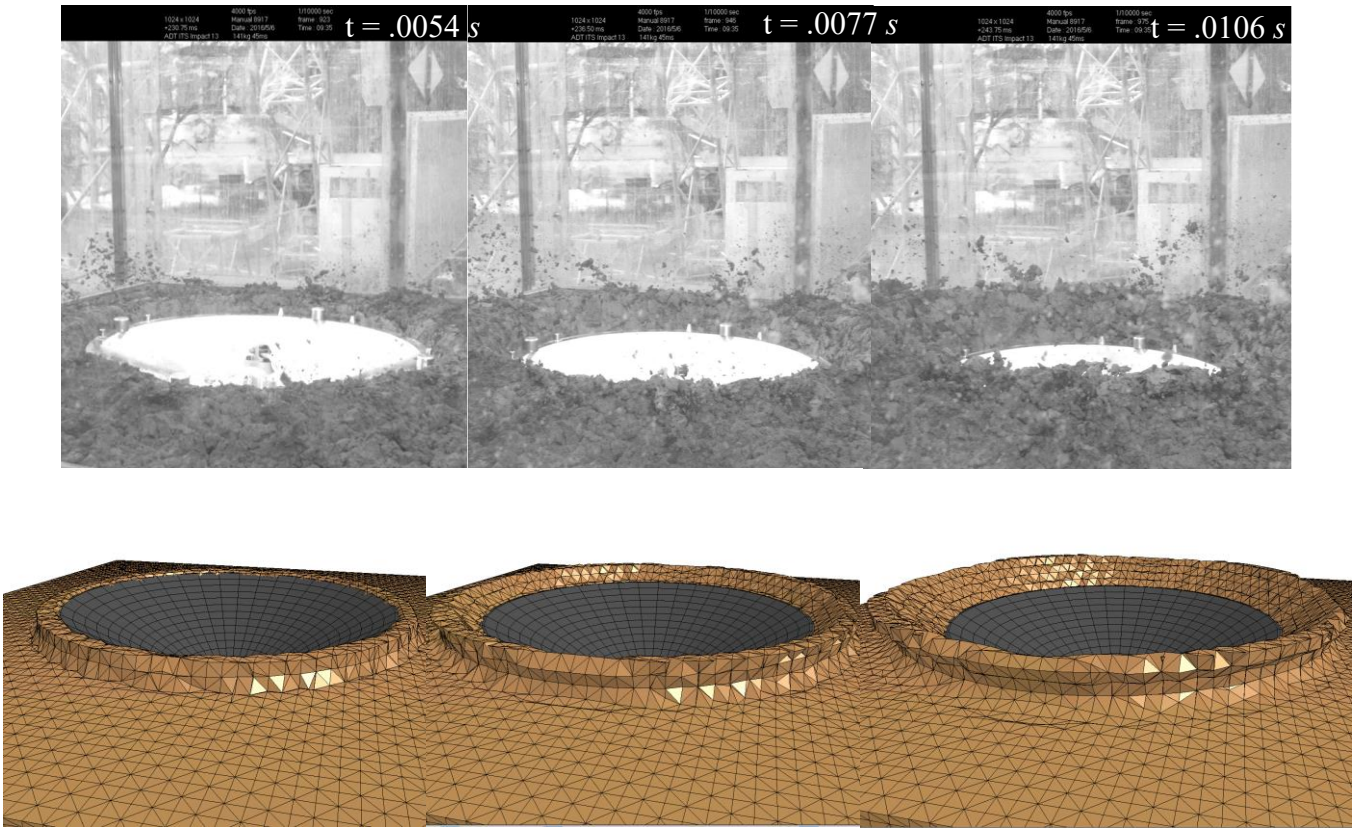

Figure 65. Time-lapse of CP-300 impact test into Rosamond soil, courtesy of JPL, compared with MMALE simulation. Part 2

The time-lapses of the actual impact test and the MMALE simulation show similar soil deformation despite the limitations of MMALE in modeling particulates due to its connected elements. Soil deformation in the simulation, while not as granular as the true test, shows the general path of deformed soil, radially outward from the impact zone. The connected elements of MMALE prevent the ejection of particles seen in the high speed images, yet the MMALE encompasses an approximate area of the ejecta as they propagate outwards.

The acceleration over time from the MMALE simulation overlaid with JPL provided data can be seen in Fig. 66.

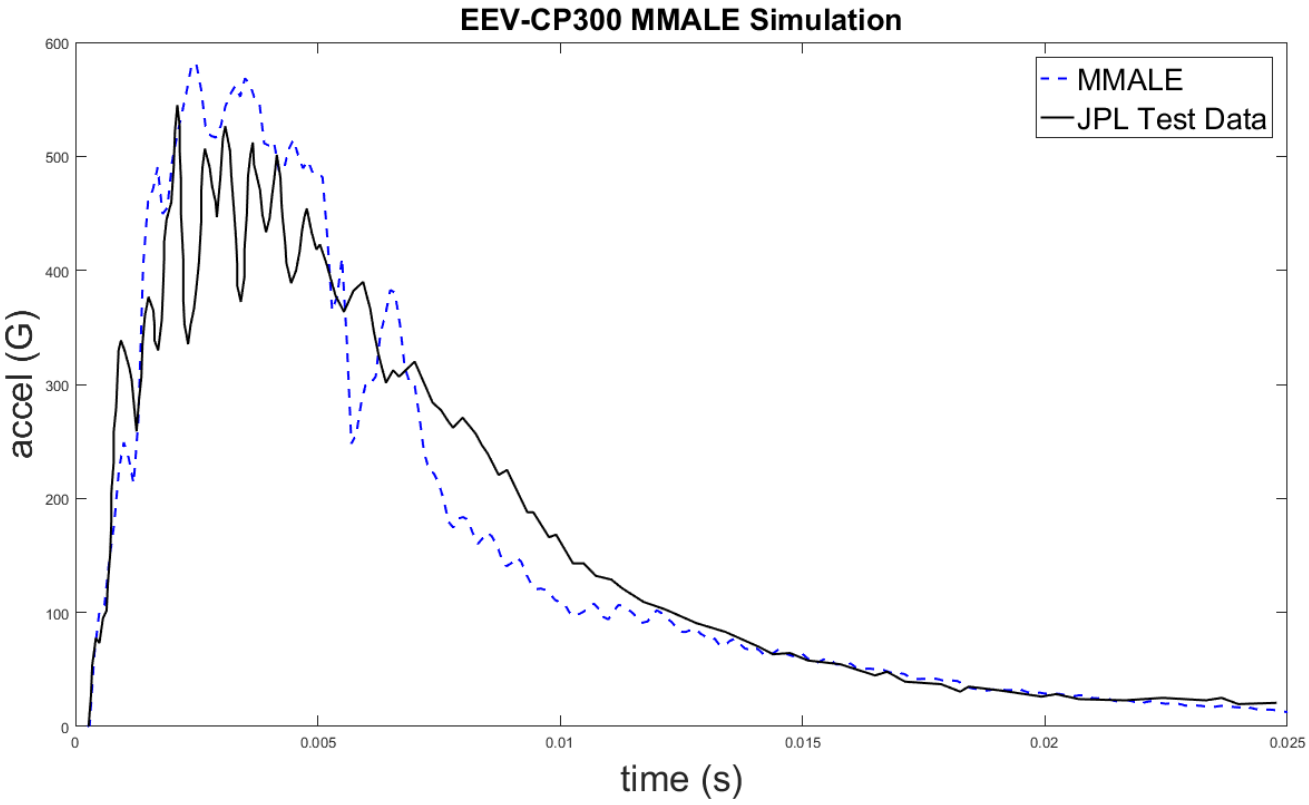

Figure 66. LS-Dyna MMALE simulation z-acceleration (dotted blue) compared to JPL test data (solid black)

The peak CP-300 acceleration during JPL testing is approximately 544.9 *G*. The measured peak load during the MMALE simulation of this event was 580.72 *G*, resulting in a 6.5 % error. Similar to other MMALE cases, there appears to be a large secondary acceleration spike at approximately .007 *s* which represents a critical penetration depth at which point there is significant acceleration influence by the sub-surface soil. This large and sudden increase in soil density is non-physical, since during the imperial test, the soil density had a continuous gradient. Due to the limitations of the measuring devices and time allocation for performing pre-test measurements, only two values of the density are recorded for each test. This results in the inability to accurately model the soil density gradient. Regardless of this limitation and the

disparities that it causes, the post peak acceleration behavior is not as crucial as the peak acceleration, and duration of peak acceleration approximation. It was confirmed that such estimates made though the finite element simulation are reasonably accurate. Based on the low percent error of the two peak accelerations, qualitative similarities between the test and simulation, and general behavior of the CP-300 acceleration curves, the MMALE methodology is partially validated.

SPH

SPH shows a strong modeling potential in terms of showing the behavior of the ejected soil particles, however less so in terms of its accuracy against the JPL proved data. The difficulty in prescribing accurate boundary conditions to the SPH particles and the computational cost required to increase particle density proved to be large negatives of using SPH. The fit of the SPH simulation to the JPL provided test data can be seen in Fig.67.

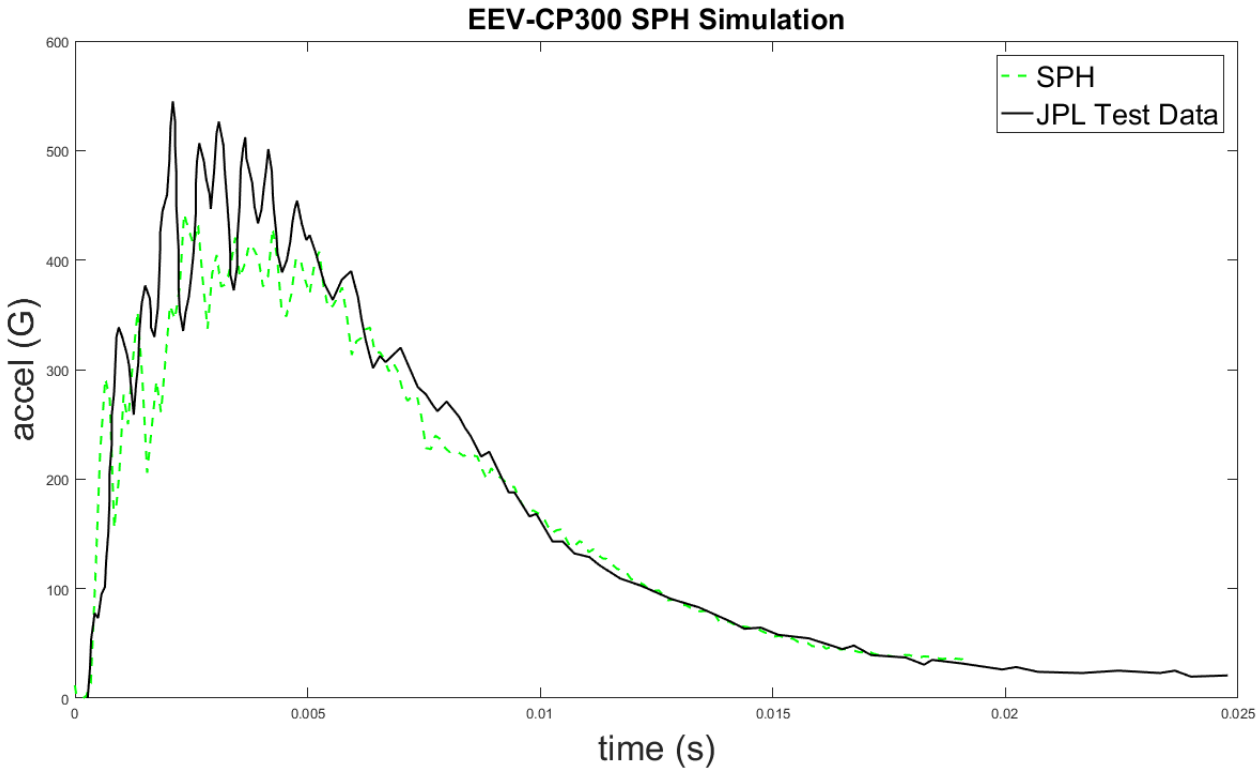

Figure 67. LS-Dyna SPH simulation z-acceleration (dotted green) compared to JPL test data (solid black)

The only large discrepancy between the SPH fit and the JPL test data is the maximum acceleration values. The loading and unloading of the soil appear to match with relative accuracy. Regardless, the peak acceleration is the most important component of the impact to match with reliable accuracy, and based on these results, SPH would not fit that requirement.

The unique ability of SPH to model ejected particles can be visualized in Fig.68

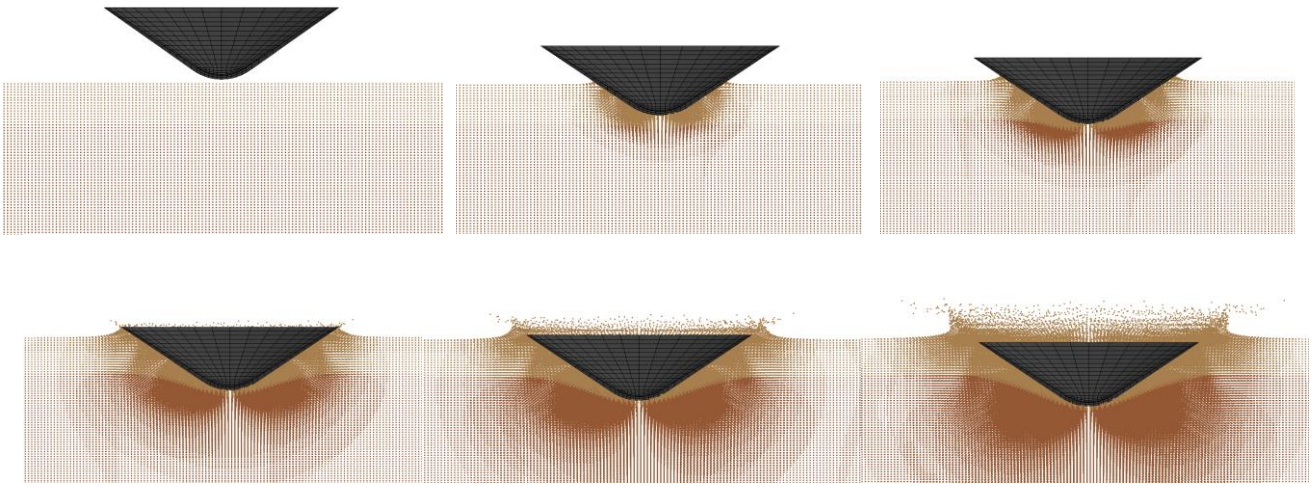

Figure 68. LS-Dyna SPH simulation of JPL test scenario using EEV CP-300

In Fig.68 the soil can be seen to eject from the impact area as the EEV penetrates the soil. The ability to model this behavior is significant because it allows for a better prediction of the soil response to impact than with alternative methods. Additionally, a qualitatively more realistic, granular response is observed, which would be useful in later development stages when more complex geometries are used as the EEV. When using more complex geometries, a granular element formulation would achieve a more lifelike interaction between the impact and soil, allowing particulates to enter otherwise unaffected areas when using connected element formulations. It should also be noted that the peak acceleration could be measuring lower than the empirical test due to the lack of soil parameter information. Simulations are limited to modeling 25% and 45% saturated soil, meaning that if parameters for the exact test case of 31% saturated were available, the accuracy of the measured peak acceleration could be improved.

Data Summary

A summary of the JPL data fitting can be seen in Table 24.

Table 24. Summary of simulation results, comparison with JPL test data

	JPL Measured CP-300 Data	Lagrangian	MMALE	SPH
Peak Acceleration (g)	544.9	466.27	580.72	442.0
Percent Error	n/a	-14.5 %	+6.5 %	-18.89 %

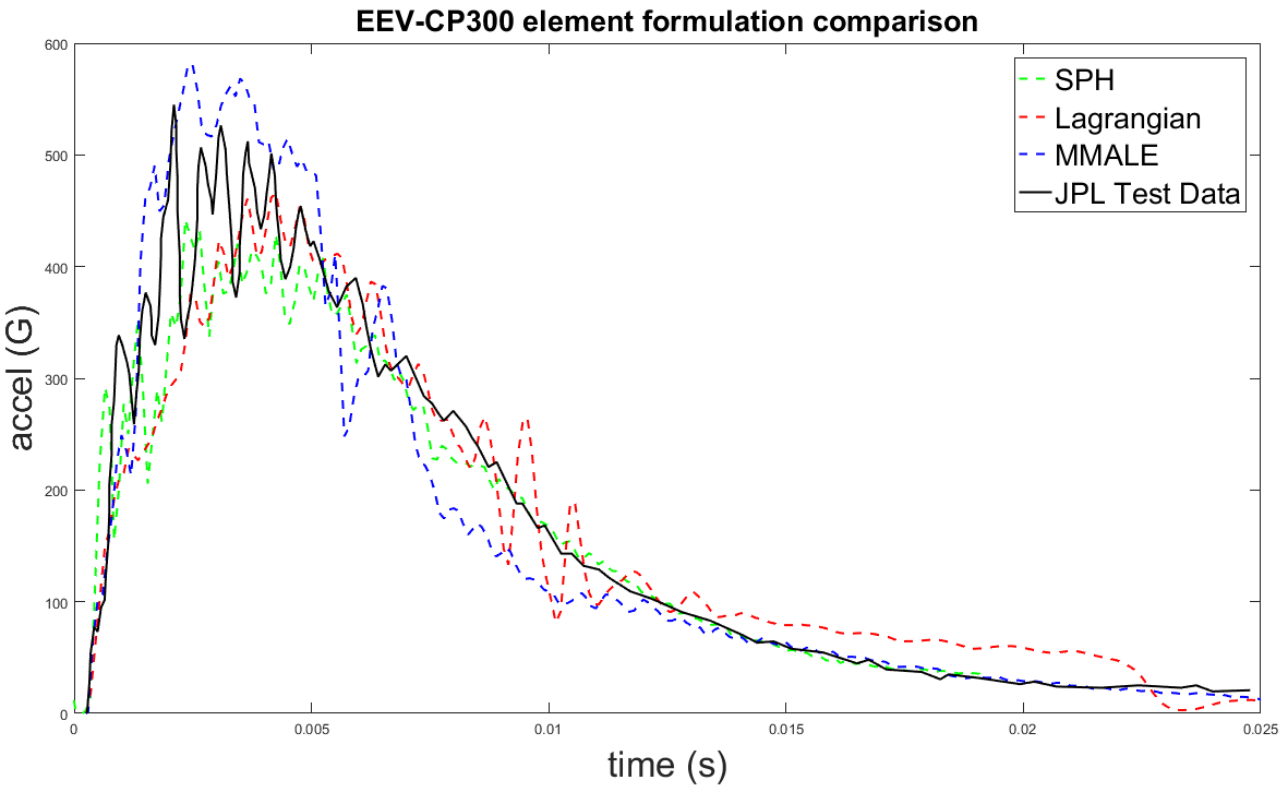

Figure 69. LS-Dyna simulation z-accelerations using varying element formulation (dotted) compared to JPL test data (solid black)

Based on the accuracy of each element formulation in its prediction of peak acceleration of the JPL empirical test, and the general ability of each to match the acceleration of the EEV over time, the most effective element formulation was shown to be MMALE, despite the

potential of SPH in modeling the loading and unloading curves. MMALE is able to show the loading and peak acceleration behaviors with close similarity to the test data, and models the unloading with reasonable accuracy. Additionally, it proved to be more viable for rapid model creation due to its simplicity when establishing initial and boundary conditions as well as its stability when modeling large deformations. Despite the relatively large error in the cases of Lagrange and SPH formulations, their errors must be considered in the context of the available validation techniques, meaning that their legitimacy cannot be negated by their error in modeling a single trial of test data. Optimally, these formulations would be used to reproduce a large range of different scenarios, and the resulting errors compared across numerous trials. Given the limited available test data, alternate methods were used to build further confidence in the legitimacy of the numerical results. This was done through the use of each numerical formulation in a larger number of trials and the results compared for percent difference in measure peak acceleration. This was performed in section 8.1 and successfully showed the potential of each formulation to show comparable peak acceleration data.

8.3.2 Prediction of EEV-CP300 Acceleration Window in Rosamond Soil

As previously performed using the EEV-R for impact with the Carson Sink soil, the available soil parameters over varying soil content for the Rosamond soil are used to create a loading window for the CP-300 over varying payload mass. Impact simulations were executed for five different payload masses of the CP-300 using two different Rosamond soil models, 25% and 45% water saturated. Using this data, an estimate for possible loading on the CP-300 during impact in the general Rosamond area can be determined. The acceleration's dependence on mass when impacting the two soil variations can be seen in Fig.70 and in Table 25.

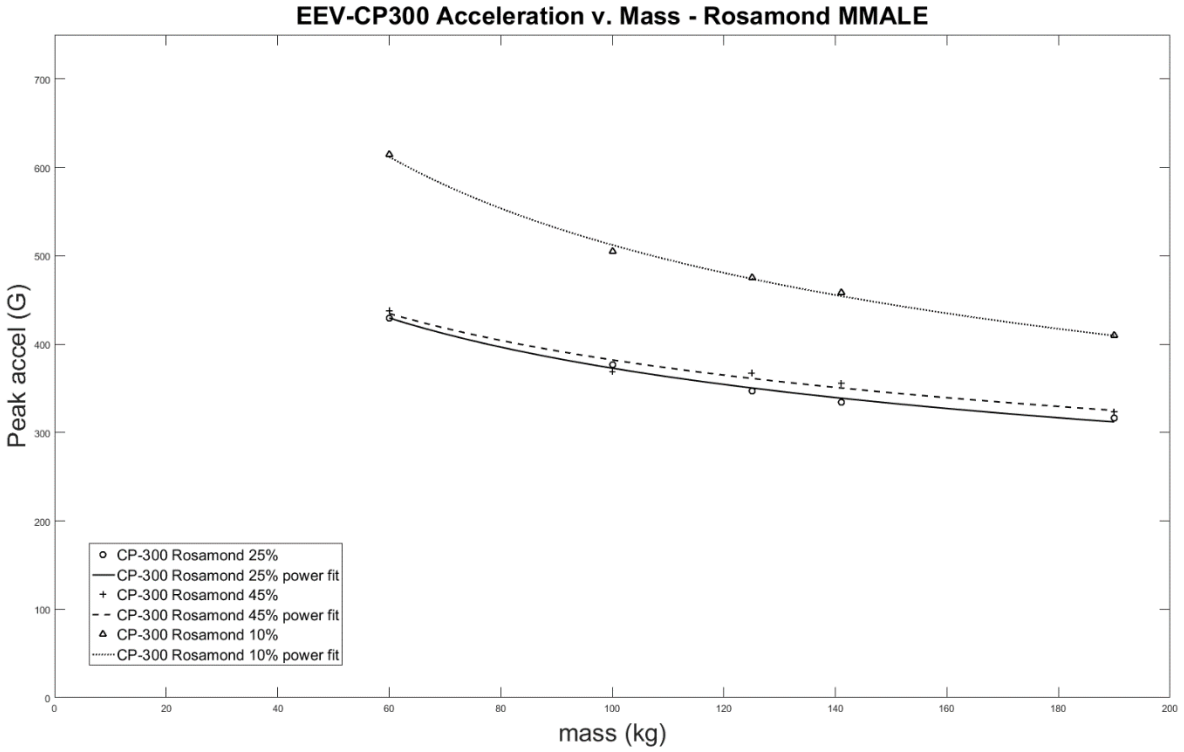

Figure 70. CP-300 z-acceleration range for Rosamond soil

Table 25. CP-300 impact acceleration and penetration in MMALE Rosamond Soil

CP-300 Mass (*kg*)	10% Sat. Soil Peak Accel (*G*)	25% Sat. Soil Peak Accel (*G*)	45% Sat. Soil Peak Accel (*G*)	25% Sat. Soil Max. Penetration Depth (*m*)	45% Sat. Soil Max Penetration Depth (*m*)
60	614.25	429.63	437.90	.39	.39
100	504.83	376.75	369.31	.46	.47
125	475.17	347.10	367.55	.48	.50
141	458.30	334.07	355.63	.50	.52
190	409.49	316.08	323.01	.55	.57

Based on Fig. 70, it can be observed that the larger water concentration resulted in an overall increase in peak acceleration during impact. Since the Rosamond area consists of soils of varying water concentration, not just 10%, 45% and 25%, estimates for loading in alternate soil water percentages can be made based on these curves.

As discussed previously, the smaller massed EEV's show a much larger acceleration upon impact due to the very rapid deceleration caused by the soil. Using a similar estimation method, the depth of each penetrometer over the two soil types can be seen in Fig.71.

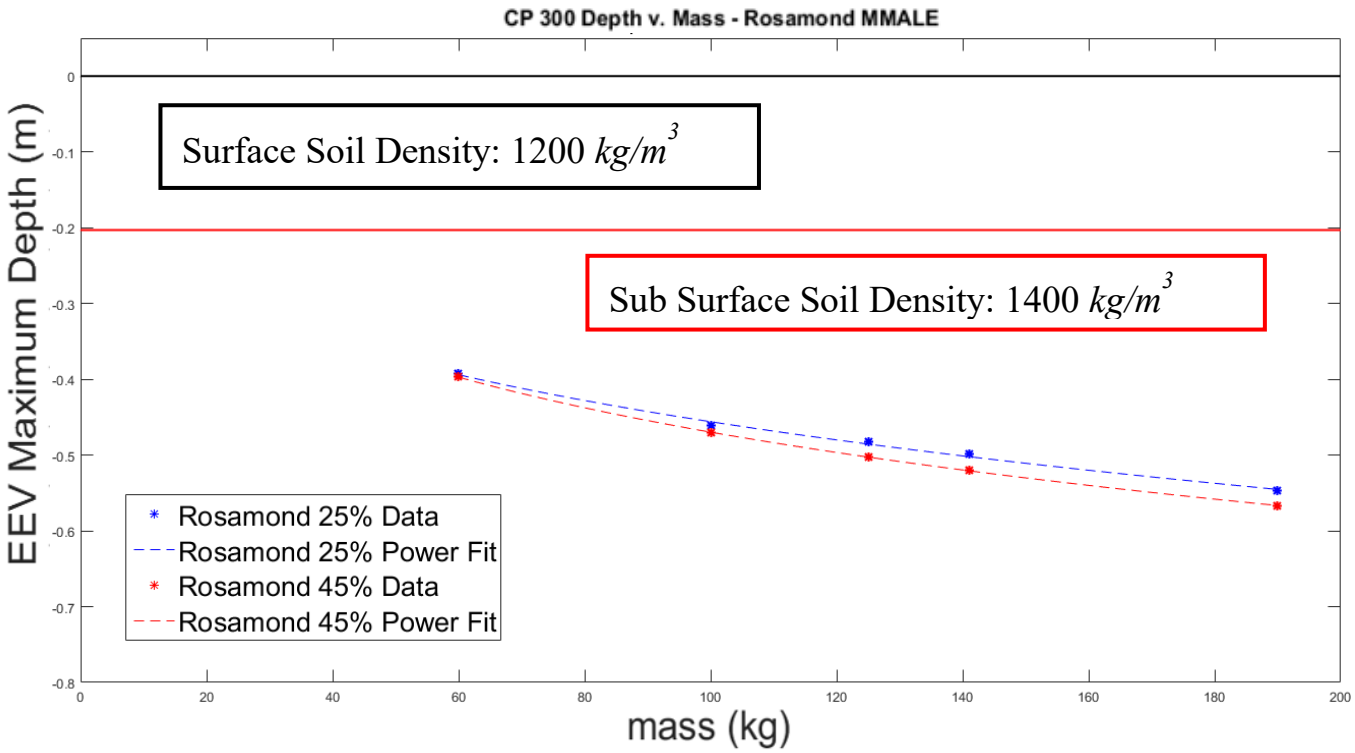

Figure 71. CP-300 penetration depth for Rosamond soil

As was the case with the Carson Sink soil, the penetration depth is correlated with the magnitude of the impact acceleration and mass such that the less massive EEV will penetrated less into the soil, and will experience a much larger impact acceleration than more massive EEVs. A large difference seen between the two soils' behavior is that despite showing lower overall peak acceleration values when impacting with the Rosamond 25% soil, the penetrometer penetrates less into the Rosamond 25% than it does into the 45%. This response should be attributed to the more fluidic response of the more watery soil, and the ability of drier soils to act like 'sponges' and compress and absorb impact energy. It is important to note that these

prediction windows assume a perfectly nominal impact with the soil surface, and are unique to the initial velocity and geometry of the CP-300.

8.4 EEV Curvature Comparison

8.4.1 EEV-R and CP-300 Comparison

In order to gain a perspective on the effects of changing EEV geometry, the acceleration results for the EEV-R, with a nose diameter of 42 *mm*, were compared with those of the CP-300, nose diameter of 300 *mm*. The predicted acceleration window during impact with the validated Rosamond soil can be seen in Fig. 72.

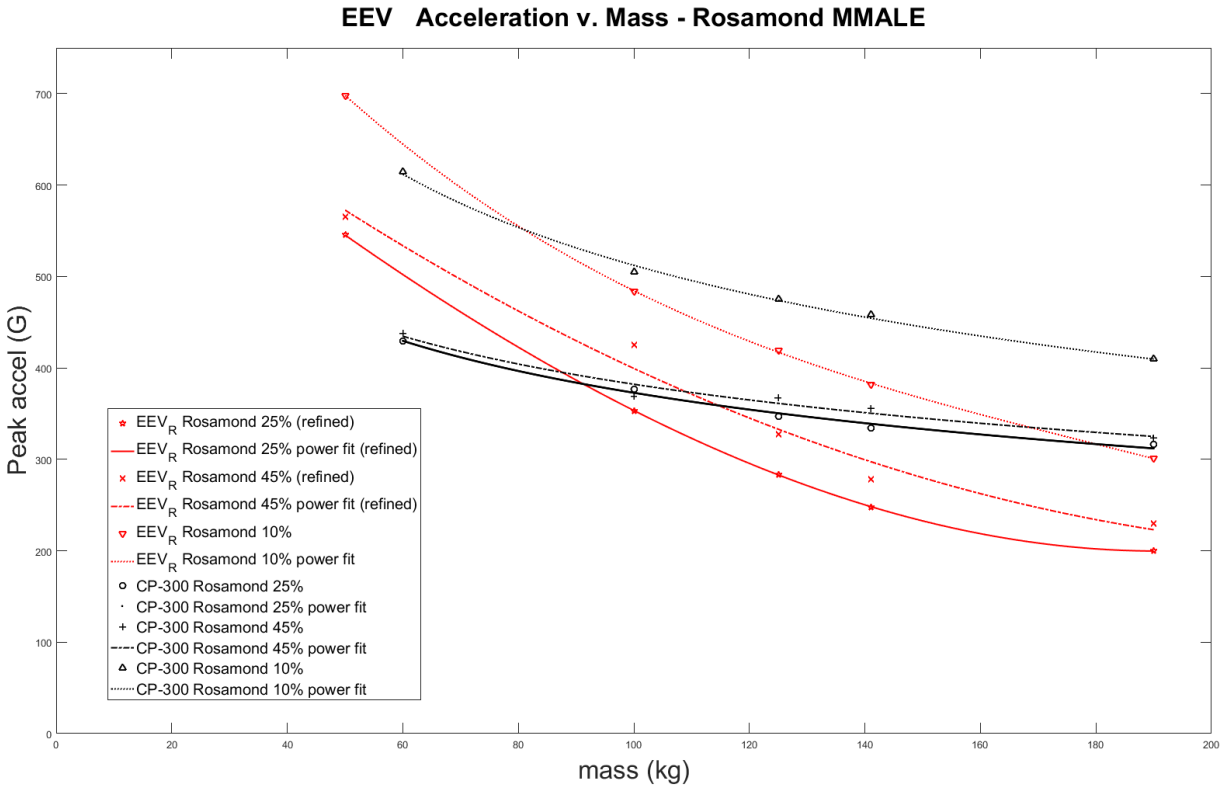

Figure 72. EEV z-acceleration comparison in Rosamond soil

Based on the acceleration curves plotted in Fig. 72, it is clear that there is a large distinction between how the two EEVs behave in the three different soil saturations. The smaller, and more pointed nose geometry of the two EEVs, the EEV-R, shows a much larger overall acceleration window than the CP-300 between the 25% and 45% saturated soils. The "refined" curves show the trend as it relates to the modified 190*kg* case where the mesh was refined to more accurately capture the large deformation of the soil. This behavior of the EEV-R acceleration window is mostly due to its smaller size, and less circular nose, which prompts a more rapid dispersal of the soil over a smaller amount of time upon initial impact, resulting in its larger acceleration. The non-linearity of acceleration over changing mass is due to the non-linear loading characteristics of the Rosamond soils, such that the applied pressure required to displace the soil increases non-linearly as the displacement increases. The peak acceleration change as it relates to mass and soil saturation can largely be attributed to the non-linearity of the soil's volumetric strain as a function of applied pressure, seen in Fig. 73.

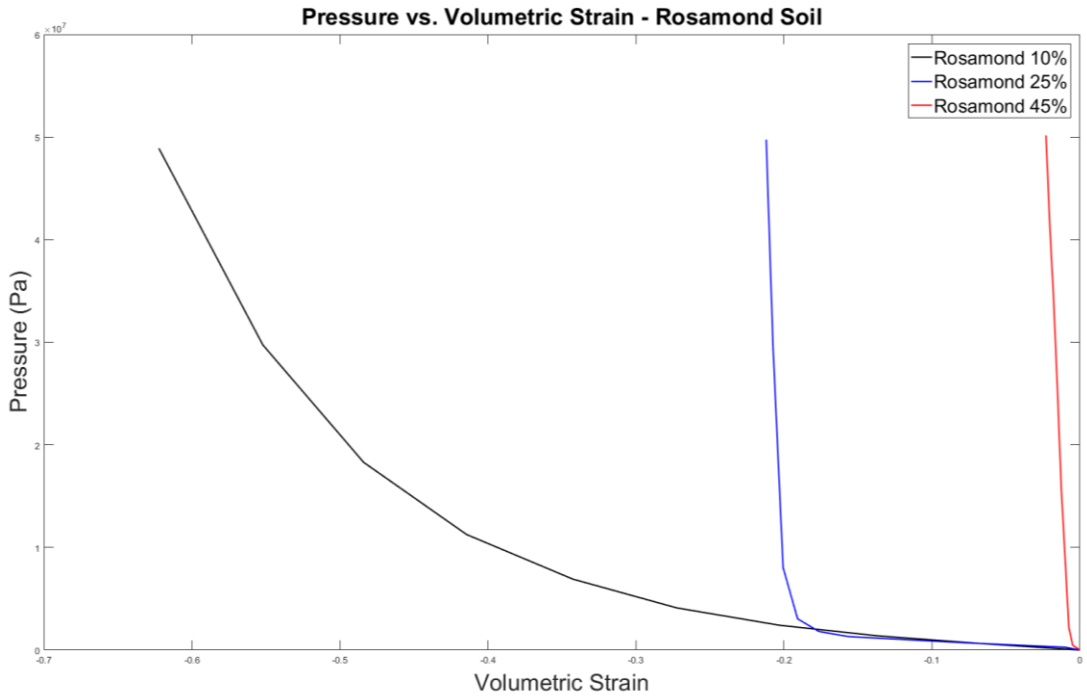

Figure 73. Pressure as a function of volumetric strain for Rosamond soil (Courtesy of JPL)

Since the Rosamond 45% soil has a much steeper pressure versus volumetric strain curve than that of Rosamond 25% and 10%, it requires much larger pressures to undergo much less strain than Rosamond 25%. This means that as the EEV penetrates the Rosamond 45%, the strain experienced by the soil is much less than that experienced by the Rosamond 25% soil, meaning a larger peak EEV acceleration. Based on this information, it would be advisable to land at a lower water content area in order to avoid the larger loading effects shown by Rosamond 45%. With this relationship considered however, there appears to be a large increase in peak acceleration when the water content is significantly reduced, as in the case of in Rosamond 10%. The large difference in the pressure versus volumetric strain curves of Rosamond 25% and 45% when compared to Rosamond 10% is the more quadratic increase of pressure with increased negative strain. This means that the drier soil will behave much different under compression than the more

saturated soils, requiring more pressure to achieve small volumetric strains during the early stages of loading. Additionally, the shear strength of the drier soil is an order of magnitude higher than the other two more saturated soils, see Table 4, meaning that the soil resists shear during impact significantly more. These two large differences in soil parameters between the 25% and 45% compared to the 10% soil are what result in the larger overall peak acceleration values during impact with Rosamond 10%, shown in Fig. 72.

Control during descent is unavailable after EEV separation with the Mars Orbiter, offering very little precision in the specific landing area. Therefore, the loading window predicted by these simulations must be used to plan accordingly in the EEV geometry and flight design. Also, comparing the accelerations of the two EEVs, clearly the larger, CP-300 offers a lower acceleration window for a larger mass range. However, there does appear to be a trend such that at very large EEV mass, the smaller, EEV-R may be a more viable choice. This is because the larger mass decelerates much slower, and show a lower peak acceleration when they are able to deeply penetrate the soil, increasing the impact time. The smaller size of the EEV-R allows its outer edges to move past the horizontal plane of the surface of the soil much sooner than those the CP-300, which never becomes fully submerged underneath the surface of the soil. Therefore, the smaller diameter means that the EEV can more quickly pass the surface plane of

the soil. This allows for deeper penetration and as a result a longer acceleration impulse. Compare the examples in Fig.74 and Fig.75.

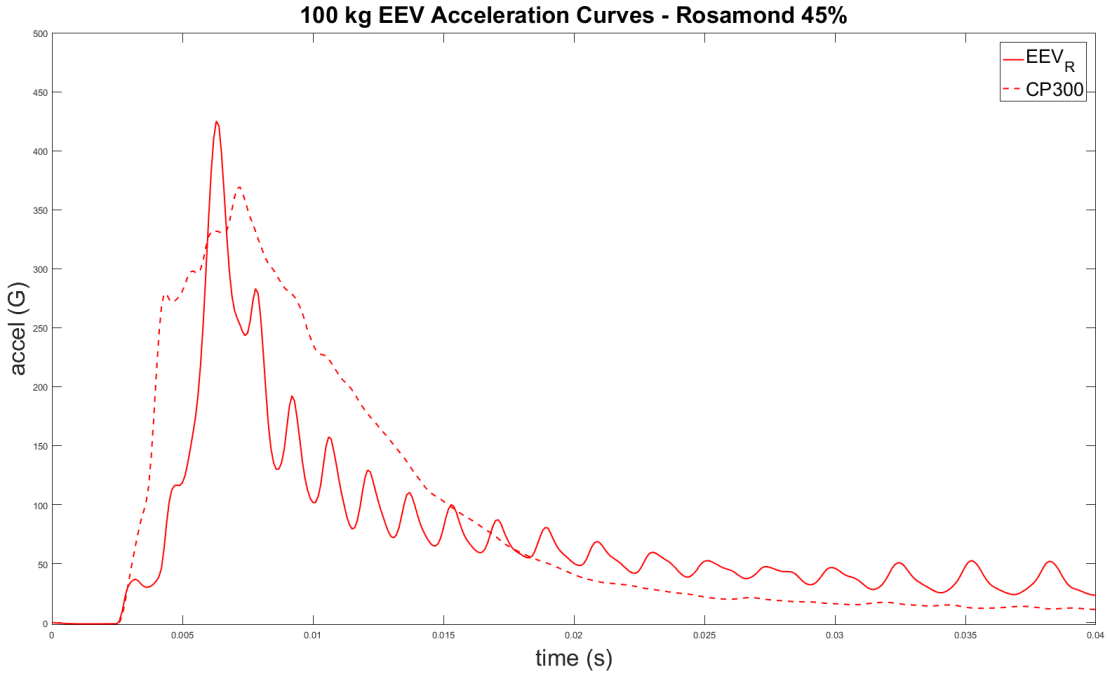

Figure 74. 100 kg EEV z-acceleration curve comparison - Rosamond 45%

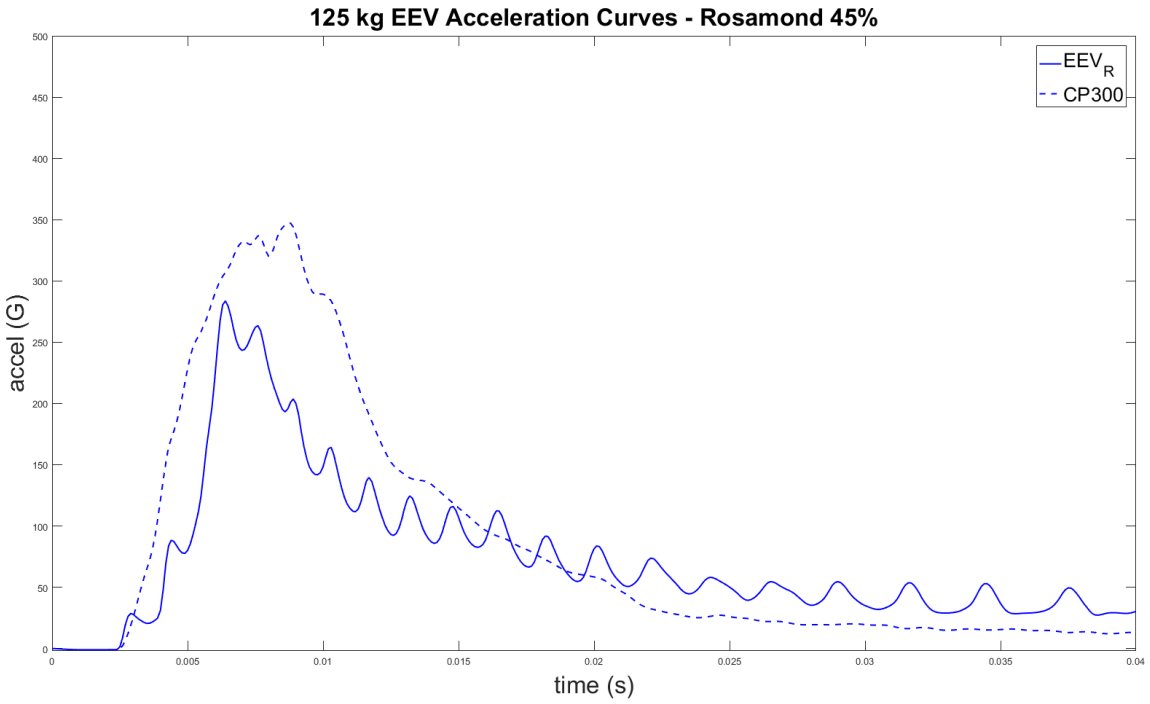

Figure 75. 125 kg EEV z-acceleration curve comparison - Rosamond 45%

Comparing the two figures above, the peak acceleration of the EEV-R is larger when each EEV is 100 *kg*, and smaller when they are each 125 *kg*. While the loading on the CP-300 does appear to be more gradual in both loading and unloading, the peak acceleration is the main design determining factor. Therefore, there exists some critical mass at, approximately 120 *kg*, when comparing these two EEV geometries at which the EEV-R, the smaller and less rounded nosed geometry, is more effective at maintaining a lower peak acceleration. A relationship between mass and EEV diameter can be seen such that larger massed, smaller diameter EEVs shows a lower peak acceleration than smaller massed, larger diameter EEVs.

8.4.2 Effects of Soil Saturation

In order to better understand the effects of soil saturation on peak acceleration, the peak acceleration of each CP-300 mass was plotted and fit over the three available soil saturations. See Fig. 76.

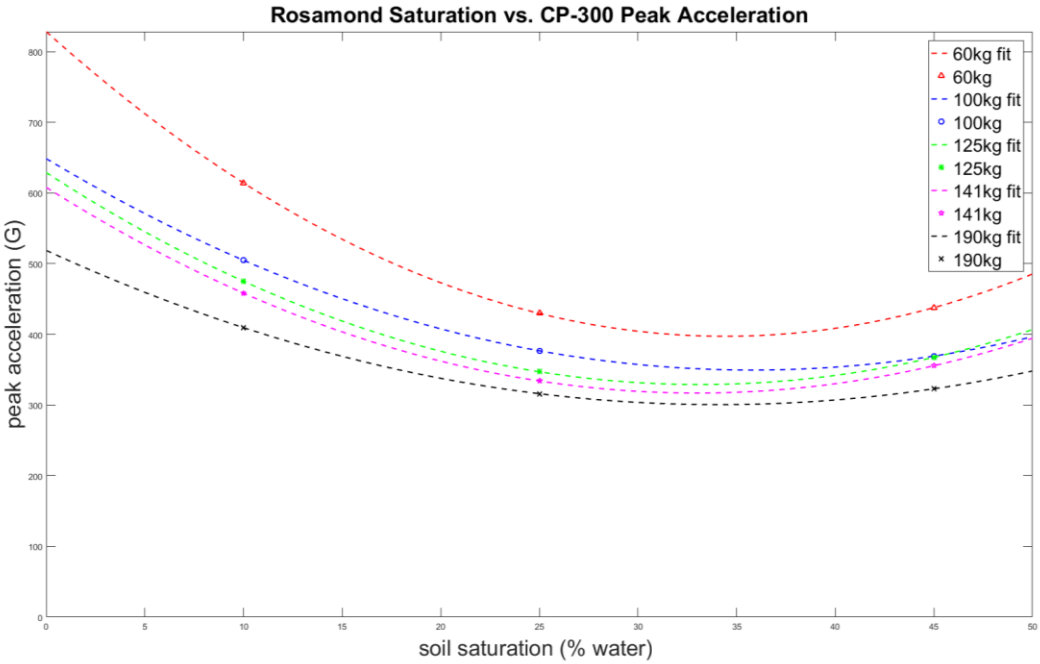

Figure 76. Peak CP-300 acceleration over varying soil saturation and EEV mass

A similar trend is seen in the behavior of the EEV-R peak acceleration over varying soil saturation, as seen in Fig. 77.

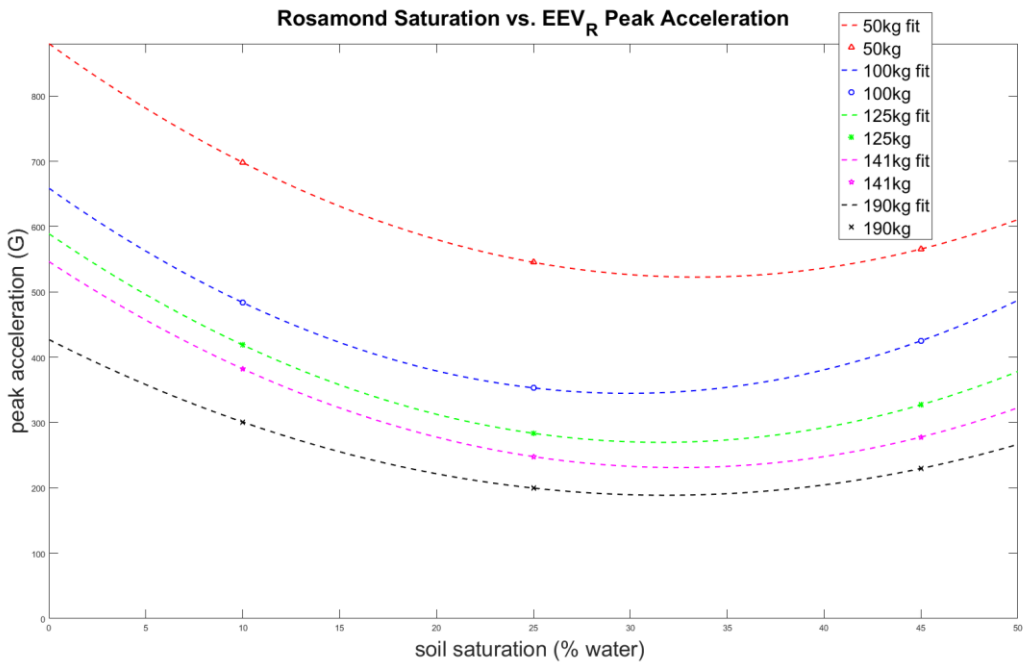

Figure 77. Peak EEV-R z-acceleration versus Rosamond soil saturation

Due to the limited material data available for soil over various moisture contents, the three available materials, and their corresponding acceleration results are the most accurate representation of the relationship between soil moisture and peak acceleration. As previously shown, the lower mass EEV, in this case 60*kg*, shows the largest overall peak acceleration at each moisture content, such that

$$A \propto \frac{1}{mass}$$

(this relation discussed in more depth in 8.4.3)

The trend in the case of both the CP-300 and EEV-R shows a second order polynomial relation such that there is a soil saturation at which the peak acceleration is minimized. The equation of fit for each mass is listed below, where β is percentage of water in the soil.

Table 26. Fit equations for CP-300 peak acceleration across Rosamond soil water content

Mass (kg)	Peak Acceleration Equation	Predicted optimal water content	Minimized Accel (G)
60	$A_{peak} = .3625\beta^2 - 25.03\beta + 828.2$	34.43%	397.30
100	$A_{peak} = .2333\beta^2 - 16.71\beta + 648.6$	35.79%	349.55
125	$A_{peak} = .2731\beta^2 - 18.1\beta + 628.8$	33.13%	329.05
141	$A_{peak} = .2674\beta^2 - 17.64\beta + 608$	32.98%	317.02
190	$A_{peak} = .1878\beta^2 - 12.8\beta + 518.7$	34.08%	300.60

Table 27. Fit equations for EEV-R peak z-acceleration through Rosamond soil water content

Mass (kg)	Peak Acceleration Equation	Predicted optimal water content	Minimized Accel (G)
50	$A_{peak} = .32\beta^2 - 21.28\beta + 879.9$	33.43%	522.69
100	$A_{peak} = .352\beta^2 - 21.01\beta + 658.7$	29.88%	344.73
125	$A_{peak} = .319\beta^2 - 20.21\beta + 588.9$	31.58%	269.72
141	$A_{peak} = .299\beta^2 - 19.4\beta + 546.4$	32.48%	231.11
190	$A_{peak} = .235\beta^2 - 14.98\beta + 427$	31.83%	188.77

Based on the information in Table 26 and

Table ***27***, the optimal soil saturation for the CP-300 geometry, and for its given impact velocity of 40 *m/s*, is approximately 34.08% water content and 31.84% for the EEV-R. It is important to recognize when analyzing this data that it is based on the limited soil parameters available, and derived through simulation, meaning that its only validation comes from the previous validations conducted and the accuracy of the soil material generation process.The above equations also only apply to an impact velocity of 40 *m/s.* It is reasoned that large peak accelerations are able to occur at both ends of the soil saturation spectrum where the least saturated soil, at 0%, would show a peak acceleration equal to the y-intercept of the above equations. Due to the large shear strength of the drier soils, their hardness is increased at low water content, increasing peak acceleration. Conversely, under larger water contents the soil is

less compressible, show more surface tension effects, and must be accelerated from the impact area, rather than compressed. Using this logic, it can be estimated that there is an optimal water content such that there is a compromise between these factors which minimizes the negative effects associate with each extreme of soil saturation. In order to validate this prediction, additional soil models must be simulated, in addition to more validation cases being performed for all soil saturations used.

8.4.3 Relating Results to M-SAPE

As previously discussed, the hemispherical penetrometer testing performed by LaRC resulting in the generation relation of peak acceleration to penetrometer parameters such that:

$$A_{peak} = \alpha \frac{DV^2}{M}$$

where D is the diameter of the hemisphere, V is impact velocity, M is the total mass, and α is a constant of proportionality; 30 in the case of UTTR. This relation was applied to the results of this study such that the diameter, D, was approximated to be the diameter of the sphere cone of each EEV. By plotting

$$\frac{DV^2}{M}$$

against the measured peak acceleration in each case, a value of α was determined for each EEV geometry and each soil moisture content by generating a linear fit of the data. The data, and the resulting fitting equations are shown below, in Fig. 78 and Table 28.

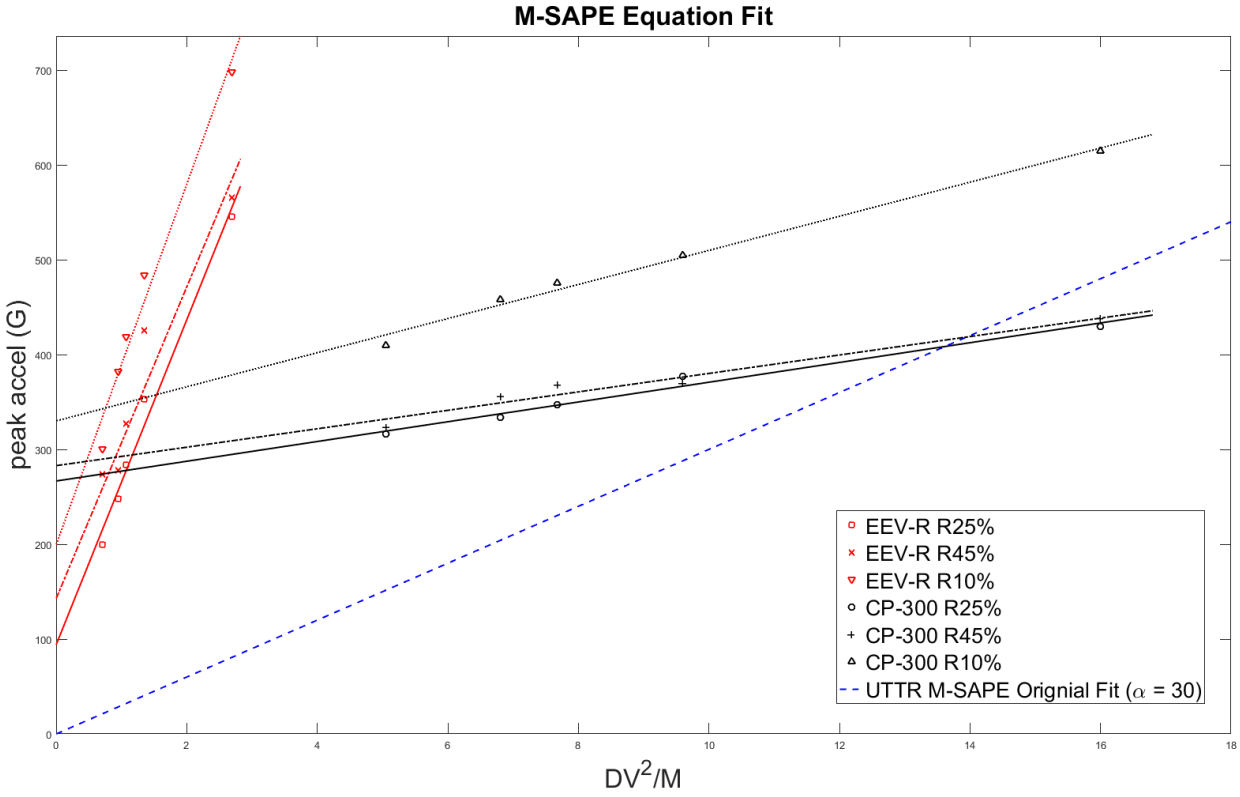

Figure 78. EEV-R and CP-300 data for Rosamond Soil related to M-SAPE original fit, with corresponding linear fits

Table 28. M-SAPE linear fit coefficients for EEV-R and CP-300 in Rosamond Soil

$A_{peak} = \alpha \frac{DV^2}{M} + C$		
EEV and Soil	α ($G*kg*s/m^3$)	C (G)
EEV-R (red)	-	-
Rosamond 10%	190	199.48
Rosamond 25%	171.2	94.18
Rosamond 45%	164.21	142.8
CP-300 (black)	-	-
Rosamond 10%	17.98	330.1
Rosamond 25%	10.41	266.7
Rosamond 45%	9.723	282.9

An immediately noticeable limitation of the equations listed is that they are non-physical as the value of $\frac{DV^2}{M}$ approaches zero, since the fits have a non-zero y-intercept. This means that in a scenario when impact velocity is zero, that the equations would indicate that there is still a non-zero impact acceleration. This means that this perfectly linear relationship cannot apply for all ranges of the $\frac{DV^2}{M}$ relation. Additionally, when applying the M-SAPE equation to non-hemispherical penetrometers, the D value must be approximated, which greatly limits the accuracy of the relation. Below, in Fig. 79, are frames of both the CP-300 and EEV-R impacting Rosamond 25% at the time of their peak acceleration.

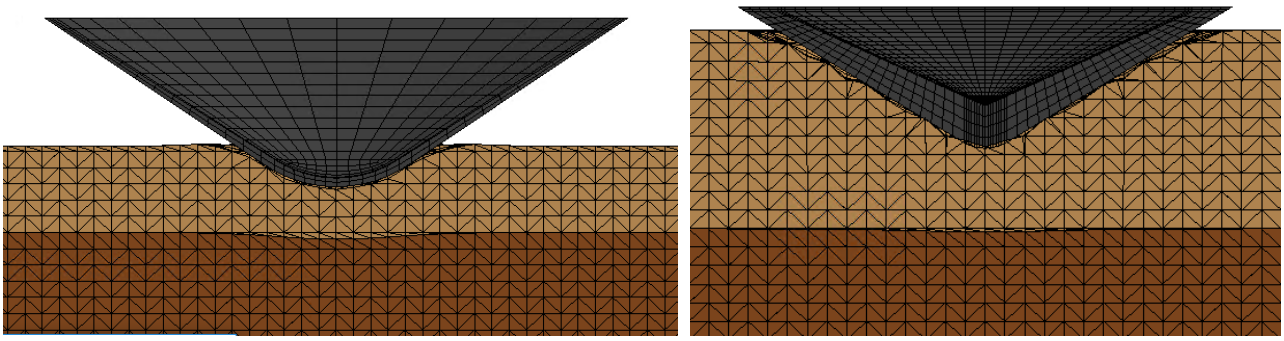

Figure 79. CP-300 (left) and EEV-R (right) at time of peak acceleration in Rosamond 25% soil (frames are not scaled to each other)

It is clear in both frames of Fig. 79 that the peak acceleration occurs at a time when the linearly sloped sides of the EEV are in contact with the soil, not just the spherical nose. This means that the peak acceleration should behave differently than that of a perfectly hemispherical penetrometer, especially in the case of sharper nosed EEV, such as the EEV-R, which penetrates significantly into the soil before peak acceleration occurs. In lower velocity or lower mass cases, where the EEV penetration is low, and limited to a depth such that the only the EEV spherical nose is able to interact with the soil, then it would be more appropriate to describe the peak

acceleration with the M-SAPE relation. However given the limitations of the derived equations, and correlation of EEV penetration with peak acceleration, the M-SAPE relation appears to not be a universal law which applied to all EEV conical geometries.

8.5 Concrete Impact

In the event that the EEV impacts with one of the many hard surfaces in the UTTR, including rock or concrete, the containment of the soil samples must be maintained. It is therefore advantageous to have the ability to predict loading to the EEV under such off-nominal scenarios. A series of impact simulations were created using all Lagrangian elements which modeled the impact of the EEV-R of nominal, 12.5 *kg*, mass at initial velocity of 40 *m/s*, with a .5 *m* deep concrete slab. In order to more accurately model the deformation of the EEV, three different material models were tested for the EEV-R: *Mat_Elastic, *Mat_Piecewise_Linear_Plasticity and *Mat_Plastic_Kinematic. The advantages and disadvantages of each has been discussed in section 6.4. Using each deformable EEV aluminum material card, the concrete mesh was progressively refined in order to determine the convergence of each subsequent mesh refinement, and the dependence of mesh density on results. Since the concrete material model used relies on element deletion to model the failure of the material, the visual component of these simulation does not necessary match real life scenarios. Additionally, a series of acceleration peaks, rather than one single large spike occur in some simulations due to element deletion. As the elements reach their ultimate yield strength, they are deleted, and the EEV is then allowed to penetrate the concrete a distance of approximately the size of the deleted element, before coming into contact again with the concrete. This results in multiple acceleration spikes, and was found to be counteracted with further mesh refinements. A control impact of the

nominal EEV-R of mass 12.5 *kg* impacting Carson Sink dry soil was also performed to give a sense of scale to the concrete impact acceleration. The measured peak acceleration of this trial for each tested material was 1029.6 *G* (The material does not yield during soil impact, and shows the same peak acceleration across all the different materials). Peak EEV acceleration organized by material and concrete mesh refinement level is shown in Table 29.

Table 29. Peak acceleration results for EEV material and concrete mesh density

EEV Material	Number of Concrete Elements	Peak Accel (G)	Percent Convergence	Percent Larger Than Carson Dry Impact
Elastic	299,820	7604.5	-	738.58 %
Elastic	1,199,280	6860.3	9.79 %	666.31 %
Elastic	2,398,560	6411.8	6.54 %	622.75 %
Plastic Kinematic	299,820	9989.8	-	970.26 %
Plastic Kinematic	1,199,280	6258.9	37.35 %	607.89 %
Plastic Kinematic	2,398,560	6432.2	2.77 %	624.73 %
Piecewise Linear Plasticity	299,820	4923.5	-	478.19 %
Piecewise Linear Plasticity	1,199,280	3445.5	30.02 %	334.64 %
Piecewise Linear Plasticity	2,398,560	5331.3	54.73 %	517.80 %

The converged results of Table 29 are shown in Fig.80.

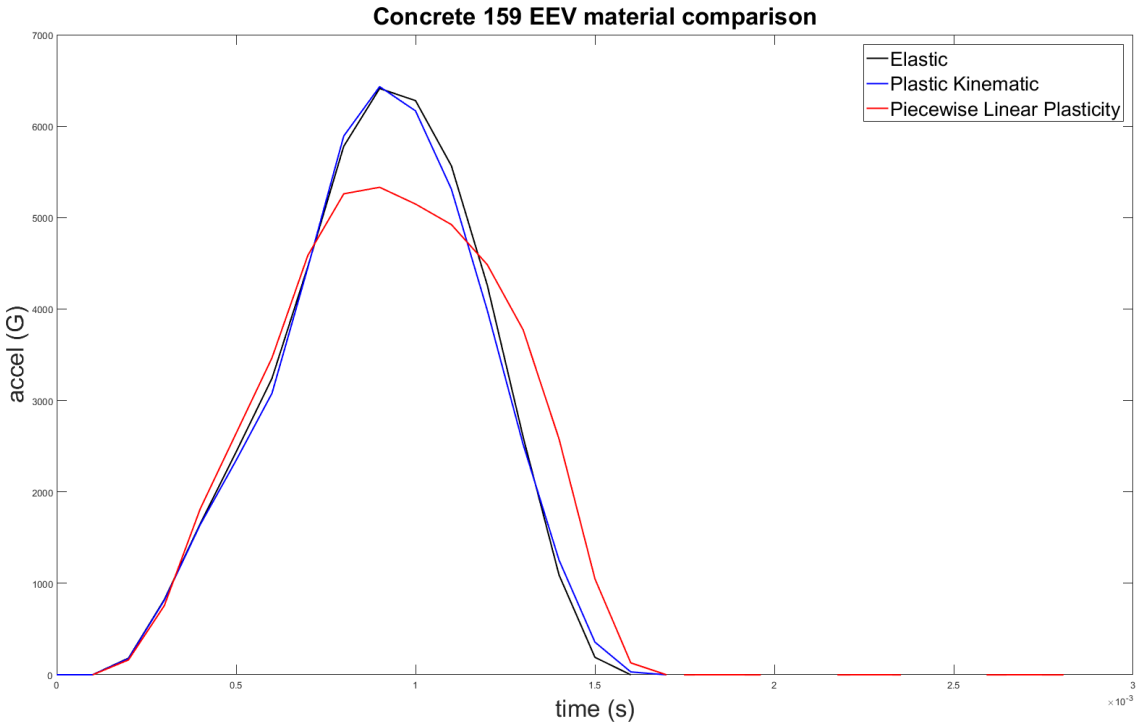

Figure 80. EEV-R z-acceleration vs time behavior for various materials during impact with converged refined concrete mesh

During the refinement of the concrete mesh for impact with a piecewise linear plastic EEV-R, it was determined that the mesh density of the concrete had the most significant effect on the EEV acceleration than any other EEV material test. This is because the deletion of concrete and EEV elements resulted in a series of acceleration spikes, rather than a single peak as was prevalent in other scenarios. This issue was fixed through the refinement of the concrete mesh. The EEV acceleration curves during the mesh refinement process are shown in Fig.81.

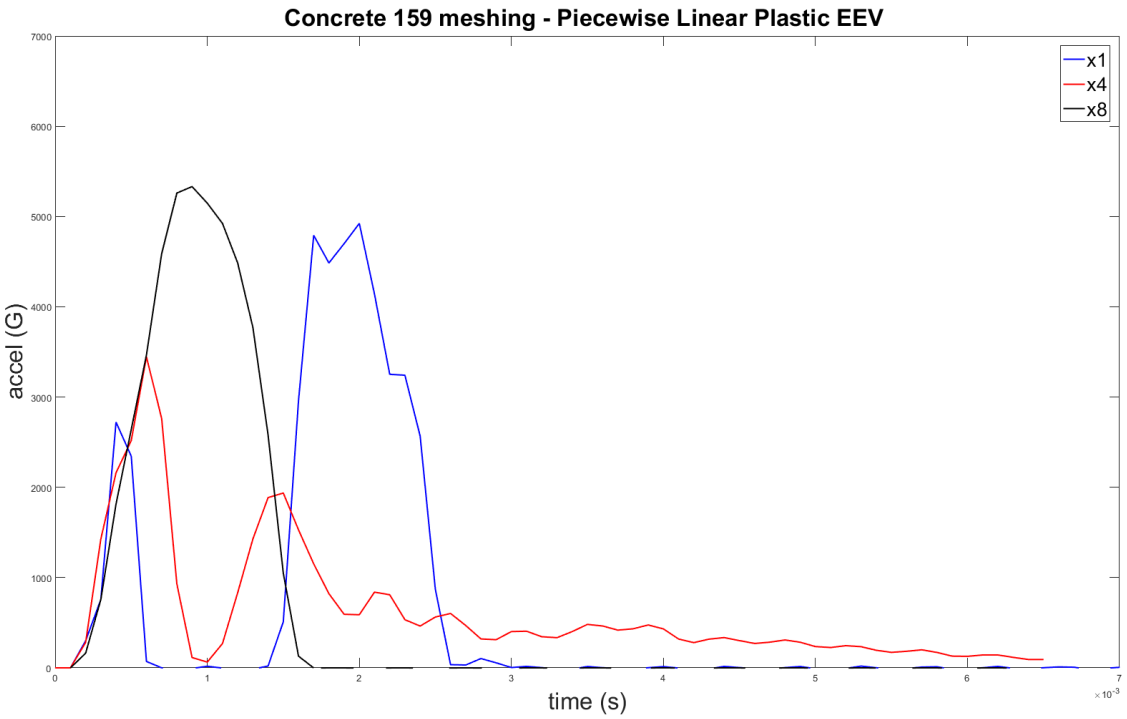

Figure 81. Piecewise linear plastic EEV-R z-acceleration during impact with concrete

Note how the blue and red curves (original and once refined meshes) show two acceleration peaks whereas the most refined simulation shows a single peak. This is because the element size allows for a much smoother transition of impact between elements as they fail and are deleted.

Based on these simulations, the loading of the EEV-R impacting with non-reinforced concrete can be predicted to be between 6500 *G* and 5000 *G*. As the concrete meshes were refined in each simulation, their results began to converge to this window, with piecewise linear plasticity showing the lowest acceleration value. As discussed previously, this is expected as this material is the only one where ultimate damage can occur, and therefore the only simulation where EEV elements are able to be deleted. The EEV materials where ultimate failure is not a possibility show an increased, and non-physical stiffness during large loading, that is not present in the piecewise linear plastic material model. It is advisable therefore to use each formulation

progressively, as was done here, in order to gain a perspective to the extent of the loading and whether failure should occur or not. During small loading, and low strain scenarios, an elastic model would be preferable, as it is easier to create, and requires few input parameters. As loading is increased, and failure is expected, plastic kinematic and piecewise linear plastic materials should be used in order to show the plastic region of deformation and eventually ultimate failure.

In addition to testing a concrete model, a short study was performed in an effort to further simplify the simulation of hard surface impact. A series of impacts were simulated using all three deformable EEV materials during impact with a perfectly rigid surface. The acceleration curves of each simulation (dotted), compared with their corresponding concrete impact acceleration (solid) are shown in Fig. 82.

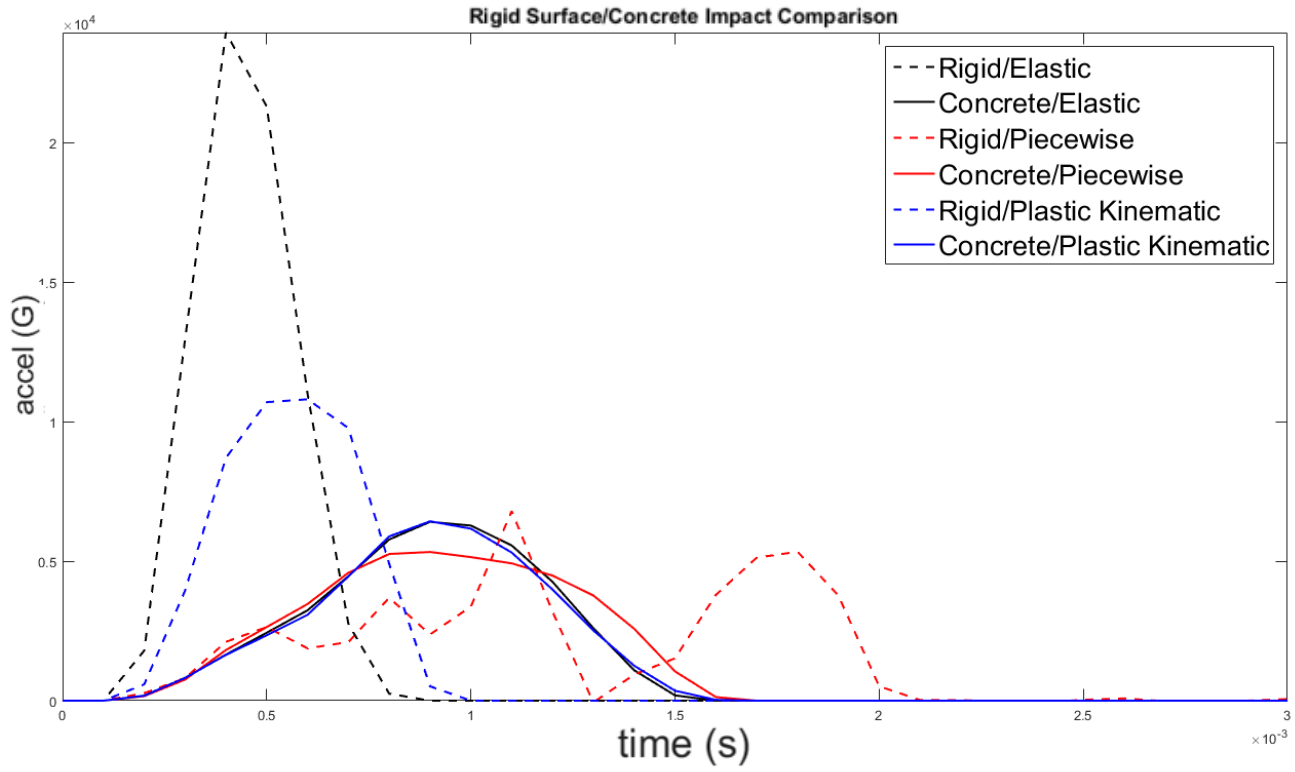

Figure 82. Deformable EEV z-acceleration during impact with rigid surface

The peak acceleration of each EEV material during impact with the rigid surface is summarized in Table 30.

Table 30. Summary of z-acceleration during rigid surface impact

EEV Material	Converged Concrete impact peak accel (*G*)	Peak acceleration for rigid surface impact (*G*)	Percent Increase in acceleration
Elastic	6411.8	23955.0	273.61%
Plastic Kinematic	6432.2	10805.0	67.99%
Piecewise Linear Plastic	5331.3	6799.2	27.53%

Based on the results of Table 30 and Fig. 82, there is a significant increase in peak acceleration experienced by the EEV during impact with a rigid surface. The magnitude of this change is dependent upon the material card used to model the EEV, such that the elastic EEV shows the largest percent increase of acceleration, 273%, compared to the piecewise linear plastic EEV which shows the lowest percent increase, 27%. This is the predicted pattern due to the limitations of each material discussed previously. Under large deformation, the elastic material is overly stiff due to its inability to model plastic deformation and show yield. Conversely, plastic kinematic and piecewise linear plastic materials have the ability to model plastic yield, plastic deformation, and in the case of piecewise linear plastic, ultimate failure. Therefore, under large stress application, such as during impact with a rigid surface, the plastically deformable materials show a lower peak acceleration due to their ability to more accurately model the deformation of the EEV as it absorbs its impact energy through plastic deformation. It is thus advisable to avoid approximating concrete as perfectly rigid, unless the materials which are impacting it are able to more accurately show failure, and absorb the impact energy. If the impact velocity were to be dropped significantly, the differences in peak acceleration between the two impact scenarios of

the elastic EEV would be much more similar, since the predicted loading on the EEV would be much less in each case.

In the case of the piecewise linear plastic material, the process of element deletion is seen during loading. The two large acceleration spikes show the loading and deletion of elements and the subsequent reloading of the elements behind the deleted elements. While this process is not physically accurate, it does allow for the modeling of ultimate failure, and in this case, for a much more similar behavior of the material over the two impact surfaces.

Based on these results, it must be advised that the used of perfectly rigid impact surface in the approximation of concrete must be done in a case by case basis, with careful consideration for the materials used in the EEV as well as the predicted strain rate and deformation extent in the EEV. As seen in this case, because the impact speed is large, and plastic deformation occurs, only an EEV material capable of modeling this behavior shows peak acceleration at all comparable to acceleration during concrete impact cases.

9. Summarizing Remarks

9.1 Element Formulations

After modeling the two soils and their wet and dry states, a general pattern is seen that is common through both EEV designs. The peak EEV acceleration is generally larger in more water saturated soils. Changes in payload mass show that the loading characteristics of saturated soils shows a much more non-linear dependence on payload mass than does the drier soils. This occurs because the more saturated soil behaves much more as a viscous fluid in its response. For this reason, an ideal landing area would be on the lower spectrum of water saturation, offering a more easily compressible impact absorbing material. Further reasoning from this logic is that the more saturated soils are not able to compress as easily as the drier, spongier soils, meaning that

as the EEV impacts, the soil must move from the impact area rather than compress. Conversely, in the case of impact with drier soils, the EEV is able to compress the soil more easily, and is not required to accelerate soil from the impact area.

A major focus of this paper is to determine the most effective method for modeling impact tests and predict EEV loading upon impact. While effective at modeling stiff materials with low deformation, the Lagrangian formulation does not effectively capture the physical response of the soil and also results in an unrealistic energy distribution in the simulations conducted. Large element distortion as a result of the soft soil material resulted in hourglassing effects in the energy, and non-physical soil interaction with the EEV geometry. While the SPH method did prove to be relatively effective at both matching the provided JPL test data, and was consistent with the results of other validated MMALE simulations, it showed numerous limitations which could hinder its effectiveness in the later life of the EEV design process. It required a large amount of computational time and was difficult to adapt to work with different Lagrange element sizes. The density of SPH particles is significantly influential in both the computational expense of the simulation as well as the ability to effectively enforce boundary conditions. The time required to execute what would otherwise be simple simulations when using other formulations was comparably high. This would limit the efficiency of the parametric studies desired for EEV design by drastically increasing computational time. Additionally, the density of the SPH particle field must maintain a ratio with the Lagrangian elements with which it is impacting in order to prevent penetration of the solid elements by the SPH particles. Therefore, when conducting trials using high fidelity EEV designs which require a refined mesh to accurately capture geometry, the SPH field must be increased in density to maintain an effective SPH-Lagrangian element ratio. SPH did prove to have capability in the modeling of the

ejected soil particles, and if a study focused on such occurrences were to take place, then SPH should be considered for that application. It is the only formulation used in this study with has the capability to model the ejecta with any form of effective fidelity.

The MMALE formulation was utilized the most for this work because it was found to be not only accurate during its validation, but also easy to apply to numerous scenarios without a need to drastically alter its initial conditions. It was resilient to the large deformation experienced by the different soils, and was able to capture the aesthetics of the soil deformation with relative accuracy. While somewhat dependent upon mesh density, the MMALE results were able to be determined with an efficient computational time when compared to the other formulations studied. MMALE mesh must be adapted to the elements with which it is interacting, but not to the specificity that is required with SPH, and not at the same large detriment to computational time. MMALE computes interaction forces based on element penetration, and as such does show larger penetrations depending on the material being used, however various mitigation options are available in the *Constained_Lagrange_in_solid card which can be used to control the over penetration. It is therefore recommended, based on these results and the experience gained in working with this element formulation that the future parametric studies and experimental replications be performed using the MMALE formulation, especially when dealing with soils or fluids.

9.2 Parametric Studies and Optimizing EEV Design for Nominal Impact

Based on the mass variation studies conducted in this work, there is a clear dependency of peak EEV acceleration on the total mass of the EEV. Larger massed EEVs of the same geometry were shown to experience lower peak acceleration upon impact than lighter EEVs

through all trials of both EEV designs. This is because the more massive EEVs are able to decelerate slower, penetrating the soil more, and allow for a longer impulse applied by the soil. Light EEVs impact with less momentum, and therefore decelerate much quicker, resulting in a significantly higher impact acceleration. In terms of actual mission applicability, there exists a ratio between the mass and EEV diameter which will slightly change the trend seen in this work, as the changes in geometry associated with changes in mass were not considered. However, despite this, the general relationship remains the same, more massive EEVs show lower peak acceleration.

Changes in the EEV geometry were not extensively investigated in this work, however based on the two EEV designs observed, there are clear behavior differences between different EEV geometries. Based off of a JPL test EEV, the CP-300 has a larger diameter and larger nose radius of curvature, meaning that the nose is less sharp a point, than the EEV-R. The EEV-R is a small EEV with a smaller radius of nose curvature than the CP-300. It was shown that at larger mass, the EEV-R was more effective than the CP-300 at reducing impact acceleration. This is because the shaper nose and smaller diameter allow the EEV-R to quickly penetrate the surface of the soil and move deep into the soil. The larger diameter of the CP-300 prevents it from quickly displacing the soil beneath it to allow the entire front surface to interact with the soil, and for the EEV to move through the soil. The longer the EEV is allowed to remain moving through the soil, the longer the impulse applied, and the lower the peak acceleration. Conversely, at smaller EEV masses, the CP-300 is more effective at reducing the peak acceleration. Additionally, because the lower massed EEVs tend to not fully penetrate the surface soil regardless of geometry, the diameter of the outer edge played less of a role in these scenarios. It

is therefore advised that more massive payloads be used in smaller diameter EEVs, with a lower radius of nose curvature, and less massive payloads be using in the larger EEV designs.

9.3 Soil Characterization and Impact Loading Window

Both validated Rosamond soil models and the available Carson Sink material data came in saturated (wet) and less saturated (dry) types, and was used to gain a perspective on the relative behavior of each under EEV impact.

In the case of both the EEV-R and CP-300, the Rosamond soil caused an overall larger peak acceleration value at each mass under less saturated soil conditions. Also, the trend of peak acceleration as a function of mass was similar between all Rosamond saturations for each respective EEV design, meaning that the general effects of the soils on the EEV are similar with changing EEV mass, with the exception of the overall induced impact acceleration. This soil behavior allows for the creation of a peak acceleration window for each EEV for a given initial velocity and variable mass. This information can be easily used to predict possible loading on an EEV of constant geometry and impact velocity upon impact with Rosamond soil ranging from 10% to 45% water saturated. This information would greatly benefit from additional soil saturation test results in order to add additional curves to more accurately map a predicted acceleration. There appears to be significant differences in the peak acceleration behavior of the two tested EEVs, showing the possible large acceleration disparities between changes in the EEV geometry. Additionally, the EEV-R shows a much larger acceleration window than the CP-300, and the changes in peak acceleration change much more in magnitude between changes in mass and soil saturation. While the results only show prediction for two different geometries, it could be estimated from these disparities in the two EEV designs, that smaller, more sharply pointed

EEVs will show a more volatile peak acceleration value change over changing mass and soil saturation. This also means that larger EEVs with larger nose radius of curvature show a more similar behavior between soil saturation and mass, and would be preferable, as their behavior could be more easily predicted.

9.4 Off-Nominal Angle Impacts

Of two scenarios for off-nominal angle impact which were tested, the cases done with constant vertical velocity through trials show the most probable case. Once within the atmosphere, the EEV, will begin to accelerate normal to the Earth's surface, and will reorient such that the nose of the EEV is towards the Earth, but will likely be reoriented due to winds above the impact area. Non-vertical velocities components were found to decreases the resultant acceleration of the EEV by reducing the interaction of the EEV with the deeper, denser soil. Nominal impacts, which penetrate the soil much more dramatically, are decelerated much faster as a result of not only impacting with the surface soil, but the subsurface soil as well. Regardless of these results, there is no control given to the EEV as to its impact orientation, and the data generated during this scenario serves only for the planning of sample containment and possible impact loads, not reduction of impact acceleration.

The case of EEV off-nominal angle impact is a scenario where the EEV is tilted off the vertical axis, but maintaining only a vertical component of velocity. This is because after Earth atmosphere entry, the geometry of the EEV, and the gravitational force of the Earth will align the EEV such that it is moving in the vertical direction, at an orientation where the normal axis of the surface of the earth is parallel, or close to parallel with the vertical axis of the EEV. Based on the parametric studies conducted for this case, an optimal off nominal impact would be such that

the EEV is oriented less than 30º from vertical, but not at nominal impact orientation. There exists some critical EEV orientation angle such that the EEV is allowed to roll slightly through the surface soil, and distribute the impact energy over the surface of the EEV, without impacting a large surface area at one instant. Orientation angles approaching 30º result in a spike in impact loading. This occurs because at a 30º off-nominal impact, the EEV impacts the soil with the largest possible surface area, and least amount of rolling, resulting in a sudden impulse of force applied. At angles larger than 30º, this effect is lessened and a decrease in impact acceleration is continued. Such large impact angles are not advised however due to other design specifications. Large impact angles could result in the tumbling of the EEV, or impact of and damage to the outer edge, which could result in another peak acceleration spike and damage to the internal components of the OS. Therefore, in order to reduce the peak acceleration, an impact orientation window of 15º from vertical should be designed for, allowing a factor of safety of 2 for impact orientation, where an impact of 30º or larger is considered failure. This window will allow for the predicted gyration of the EEV during descent due to aerodynamic forces to occur as well as limit the peak acceleration to the lowest possible values.

9.5 Concrete Impact

The case of EEV impact with concrete (or rock), a small possibility associated with landing in the UTTR was tested using a series of EEV material models to gain a perspective of its behavior during impact with a hard, brittle material. It was determined that the concrete material used was highly mesh dependent in its response due to its reliance on element deletion to model failure of the material. Similarly, the piecewise linear plastic aluminum model used for the EEV is reliant on a similar technique of element deletion to show failure, meaning that

simulation in which it is used are that much more dependent on mesh density. The most refined mesh case used with this material was shown to be less reliant in behavior on the deletion of elements, and to be more comparable to other cases. During the concrete mesh refinement process it was determined that the acceleration curves of the EEV were converging to a peak value between 5000 *G* to 6500 *G*, a window approximately 480% to 630% larger in magnitude that the control EEV impact with Carson Sink dry soil. As would be expected, this impact case would drastically increase the peak acceleration felt by the EEV. The probability this kind of an impact must be analyzed prior mission start in order to effectively anticipate the extremely large loading induced by concrete or rock impact. Such an occurrence has the largest capability of compromising the sample containment of the OS and must not be overlooked by the various concerns of analyzing and simulating soil impacts.

10. Conclusion

10.1 Numerical Modeling

The objective of this work was to generate finite element models of EEV impact with various soils of differing moisture content for the purpose of estimating peak acceleration of the EEV. Models were constructed using three element formulations, Lagrange, MMALE, and SPH, to explore the advantages and disadvantages of each. All were able to accurately match the provided JPL EEV impact data, and were able to show consistent results across most other studies performed. Of these element formulations, MMALE proved to show the best combination of qualitatively accurate soil deformation, ability to reliably and accurately predict EEV impact loading, ease of model creation for large parametric studies, and simulation stability and robustness. Lagrange formulation, despite its accuracy in estimating peak loading in the cases simulated, was consistently subject to large hourglassing energies and element distortions

during the large and fluidic soil deformations. SPH, while comparably as accurate as MMALE, and uniquely able to model the granular response of the soil, was found to be much more computationally expensive than other formulations, and much more difficult in enforcing the experimental boundary conditions due to the lack of connectivity between elements. In studies when the modeling of the ejected soil, or extremely large deformation is expected, the use of SPH is advisable. Based on these conclusions, MMALE soil models should be used in the future when attempting to recreate test data, and predict EEV loading.

10.2 EEV Design for Nominal and Off-Nominal Impacts

The off-nominal angle impact of the EEV has a high likelihood of occurring, as a result of the oscillation of the EEV due to aerodynamic forces during descent. Based on the results of testing both the scenario when the velocity and orientation of the EEV are changed, and when just the EEV orientation is changed velocity kept in the vertical direction, an ideal EEV orientation is a rotation less than 30º from the vertical axis. Assuming an EEV with 60º sloping sides, impacting at an angle of 30º with velocity normal to the impact surface results in the complete loading of the maximum surface area of the EEV at a single instant, resulting in a large, rapid acceleration of the entire EEV body. Due to the passive nature of the EEV descent and deceleration, there is no way to actively control the EEV orientation prior to impact, and it is therefore advisable to design the EEV geometry to maintain orientation angle less than 30º, preferably 15º to maintain a high factor of safety. Impact scenarios when the velocity vector has both vertical and horizontal components is highly unlikely due to the nature of the expected descent path, but if this were to occur, an ideal case would be such that the EEV would approach

at steep enough angle as to prevent any likelihood of tumbling or secondary impact, yet shallow enough to allow for the maximum interaction of the EEV with the less dense surface soil.

Comparing and analyzing the two EEV geometries impacting the four soil variations used in this work show that the loading on the EEV is dependent upon both its geometry and mass, as well as the soil saturation at the impact area. Overall, the more saturated soil tended to produce a larger overall peak acceleration across EEV geometries and masses. The smaller EEV-R geometry shows larger acceleration at small mass, and smaller acceleration at large mass than the CP-300. The larger diameter of the CP-300 allows less disparity between the loading magnitudes of different massed payloads, as well as a smaller loading window between different soil saturations. It is therefore recommended that when the mass of the EEV alone is in question, that a smaller, more pointed EEV geometry be used for large mass, and a larger EEV, with a larger radius of nose curvature be used for a light payload.

Finally, impact with a concrete slab was simulated to gain perspective of the possible loading of the EEV. It was determined, through extensive material testing and mesh refinement that EEV impact with the chosen non-reinforced concrete would result in peak accelerations over 600% larger than during soil impact. This particular scenario is currently only tested through simulation, and no empirical test data exists for this specific scenario for its validation. It should therefore only be used in the argument for said empirical testing, and the importance of planning for EEV impact with concrete or other hard objects in the UTTR.

10.3. Future Work and Exploratory Programs

The limitation of this work is that the dependence of mass on EEV diameter was not considered when performing the mass variation studies of the two EEVs. The goal of the mass

variation simulations was to gain a perspective on the effects of an increase in EEV payload, internal component mass or material density. Additionally, the impact velocity of the two EEVs through changing mass was kept constant. This assumption does not account for the changes in terminal velocity associated with changes in mass and effective diameter. Furthermore, the comparison of the two EEV designs cannot be used to made conclusive assumptions about the effects of changes in EEV geometry as this would require a larger number of varying geometry EEVs to be tested. This section was included as a matter of course after the separate analysis of each geometry had taken place, and to make the distinction that large differences in behavior exists as a result of changes in geometry, and that further investigation should be made.

Regardless of their limitations, the results of each numerical method were still comparable to one another and the provided experimental data, and a conclusion on the appropriate element formulation for soil modeling was made. Future finite element parametric studies of EEV impact should focus more on the optimization of EEV design through the input of more realistic EEV initial conditions, and less on the qualification and selection of simulation methodology, as was done here.

While more difficult to achieve, off-nominal angle empirical tests should be performed to validate the results proposed in this work, as their integrity is based only on the predetermined material and element formulation validity, and logical reasoning behind their behavior. Since it is a likely occurrence, off-nominal angle impact tests would allow for the expansion of current finite element simulations available and allow for the validation of the reasoning proposed in this work as the cause of large accelerations during a critical EEV orientation. Similarly, empirical test data must be gathered of EEV impact with off-nominal impact materials, particularly with materials or object geometries which pose the largest threat to loss of sample containment.

Impact with rock or concrete was considered in this work, as it would be one of the likely off-nominal cases, and the validation of the created models would serve to aid in the containment system design process.

10.4 Contributions

The results of this work prove the validity of utilizing finite element simulations for the purpose of recreating both the behavior of the EEV, and of the soil, during impact. The conclusions drawn on the advantages of using MMALE and SPH formulations will aid in the advancement of the limited published work on EEV impact modeling, giving insight into the situations in which each method excels. Future work in this area will be able to focus more on design of the EEV when performing simulations, than on the selection and validation of modeling techniques. Therefore, future work will be able to implement higher fidelity EEV/OS models, and be used with mission specific EEV designs to show mission scenario loading across various soil conditions.

The methodology of acceleration window estimation as a function of soil saturation and varying EEV design parameters can be used to map out possible loading behavior on the EEV using limited empirical test results, and a validated simulation technique. A set of equations used for the estimation of peak acceleration as a function of EEV design parameters, as well as for soil moisture content was proposed and defended. What was unable to be accomplished during impact testing of years past, the validation of finite element models using collected empirical test data, was achieved. Additionally, a foundation in the use of finite element models for EEV impact testing has been created through the various soils, off-nominal orientations, EEV geometries and masses that were tested. The relationships between all of these variables has been

predicted using validated formulations and material models, serving as a basis for choosing what impact scenarios should be empirically tested in the future, and what EEV designs and orientations show optimal behavior in various soil conditions. Once applied to ongoing sample return missions currently in design, the results of this work will enable for a more efficient and timely design process and give engineers a reliable EEV acceleration prediction method.

References

1. Alexander, E., Carey, B., DiNardo, M., Gill, H., Gonzalez, J., Harry, M., Isidro, A., Judge, S., Puckett, K., Schoepfer, G., Song, Y., Tilghman, M., Siddens, A., Satterwhite, M., Bayandor, J. (2012) 'Validated Aerospace Soft Impact Modeling Platform'. *ASME 2012 Fluids Engineering Division Summer Meeting*, p. 789. doi: 10.1115/FEDSM2012-72459. [3 May 2017]

2. Billings, M. D. (2002) 'Analytical Simulations of Energy-Absorbing Impact Spheres for a Mars Sample Return Earth Entry Vehicle' *NASA/CR-2002-211671*. [4 May 2017]

3. Burnett, D. S., Barraclough, B. L., Bennett, R., Neugebauer, M., Oldham, L. P., Sasaki, C. N., Sevilla, D., Smith, N., Stansbery, E., Sweetnam, D., Wiens, R. C. (2003) 'The Genesis Discovery mission: Return of solar matter to earth', *Space Science Reviews*, 105(3–4), pp. 509–534. doi: 10.1023/A:1024425810605. [3 May 2017]

4. Do, I. and Day, J. (2005) 'Overview of Ale Method in Ls - Dyna', *Livermore Software Technology Corp*, pp. 1–48. [7 May 2017]

5. Gretsch, J., Henry, M., Jivani, M., Liwanag, M., Rogers, A., Smisko, A., Wolf, D., Siddens, A., Satterwhite, M., Bayandor, J., (2012) 'A Virtual Aerospace Crashworthiness Modeling Platform: Part I, Substantiation Water Ditching Trials', *50th AIAA Aerospace Sciences Meeting including the New Horizons Forum and Aerospace Exposition*, (January), pp. 1–9. doi: 10.2514/6.2012-688. [6 May 2017]

6. Guo, Y. (2010) 'Meshless Methods in LS-DYNA : An Overview of EFG and SPH', *Seminar, Stugartt, Germany*. Available from: Resarch Gate [10 May 2017]

7. Hallquist, J. (2006) 'LS-DYNA® theory manual', *Livermore Software Technology Corporation.* Retrieved from: http://www.dynasupport.com/manuals/additional/ls-dyna-theory-manual-2005-beta/at_download/file. [1 May 2017]

8. Horton, B., Song, Y., Feaster, J., Bayandor, J., (2017) 'Benchmarking of Computational Fluid Methodologies in Resolving Shear-Driven Flow Fields', *Journal of Fluids Engineering*, 0(0), p. 13. doi: 10.1115/1.4036590. [3 May 2017]

9. JPL Failure Review Board and Sub-team. (2005) 'Genesis Failure Investigation Report', *NASA Jet Propulsion Laboratory*. [3 May 2017]

10. Kellas, S. (2002) 'Design , Fabrication and Testing of a Crushable Energy Absorber for a Passive Earth Entry Vehicle: NASA/CR-2002-211425', *Nasa Sti*, (211425), pp. 1–49. [3 May 2017]

11. Kellas, S. (2016) 'Passive Earth Entry Vehicle Landing Test'. [8 July 2017]

12. Kim, M., Zammit, A., Siddens, A., Bayandor, J., (2011) ‘An Extensive crashworthiness methodology for advanced propulsion systems, Part I: Soft impact damage assessment of composite fan stage assemblies’, *49th AIAA Aerospace Sciences Meeting Including the New Horizons Forum and Aerospace Exposition*, (January), pp. 1–16. doi: 10.2514/6.2011-980. [3 June 2017]

13. LS-Dyna Keywork Manual. U. S. (2007) *Keyword User Manual*. Livermore Software Technology Corporation [7 May 2017]

14. Mattingly, R. and May, L. (2011) ‘Mars Sample Return as a campaign’, *2011 Aerospace Conference*, pp. 1–13. doi: 10.1109/AERO.2011.5747287. [17 May 2017]

15. Murray, Y., Abu-Odeh, A. and Bligh, R. (2007) ‘Evaluation of LS-DYNA Concrete Material Model 159’, *U.S. Department of Transportation Federal Highway Administration* (May), p. 206. [23 April 2017]

16. Perino, S., Bayandor, J., Samareh, J., Armand, S.(2014) ‘A Structural Concept Study for Planetary Probes and Sample Return Vehicles’, *International Planetary Probe Workshop*, (July 2015). doi: 10.2514/1.A33050. [2 May 2017]

17. Perino, S., Bayandor, J. and Siddens, A. (2012) ‘A Comprehensive Structural Dynamic Analysis Approach for Multi Mission Earth Entry Vehicle (MMEEV) Development’. *NASA/CR-2013-218003* [9 May 2017]

18. Samareh, J.,Glaab, L., Winski, R., Maddock, R., Emmett, A., Munk, M.M., Agrawal, P., Sepka, S., Aliaga, J., Perino, S., Bayandor, J., Liles, C., (2014) ‘Multi-Mission System Analysis for Planetary Entry (M-SAPE) Version 1’, *NASA/TM-2014-218507* (January). [20 May 2017]

19. Samareh, J., Maddock, R. W. and Winski, R. G. (2012) ‘An integrated tool for system analysis of sample return vehicles’, *2012 IEEE Aerospace Conference*, pp. 1–8. doi: 10.1109/AERO.2012.6187294. [23 May 2017]

20. Siddens, A.J. (2012) ‘A Predictive Methodology for Soft Impact Damage In Jet Engines Incorporating Hybrid Composite Structures’. *Master's Thesis. Virginia Tech.* [12 May 2017]

21. Squyres, S., Soderblom, L., Calvin, W., Cruikshank, D., Ehrenfreund, P., Hubbard, G., (2011) 'Vision and Voyages for Planetary Science in the Decade 2013–2022, Lpsc.' *National Academies Press*. doi: 10.17226/13117. [3 May 2017]

22. Thomas, M.A., Chitty, D.E., Gildea, M.I., T'Kindt, C.M.,(2008) ‘Constitutive Soil Properties for Unwashed Sand and Kennedy Space Center’, *NASA/CR-2008-215345* (August). [3 May 2017]

23. Vesenjak, M. and Ren, Z. (2009) ‘Application of Smoothed Particle Hydrodynamics Method in Engineering Problems’, pp. 273–290. [10 May 2017]

24. Wu, C. T., Hu, W. (2014) ‘An Introduction to the LS-DYNA® Smoothed Particle Galerkin Method for Severe Deformation and Failure Analyses in Solids’, *13th International LS-DYNA Users Conference*, pp. 1–20. [3 May 2017]

Appendix A

Empirical EEV impact test data ("Phase A, Test 13"), courtesy of JPL

Time (s)	Acceleration (g)
0	0
4.95E-05	27.30109
7.42E-05	53.51014
0.000124	68.79875
0.000148	77.5351
0.000223	73.16693
0.000297	95.0078
0.000371	101.5601
0.000396	124.493
0.000445	151.7941
0.00047	181.2793
0.00047	205.3042
0.000519	232.6053
0.000519	258.8144
0.000569	279.5632
0.000593	304.6802
0.000618	329.7972
0.000668	338.5335
0.000742	329.7972
0.000841	314.5086
0.00089	303.5881
0.00094	280.6552
0.000989	258.8144
0.001039	286.1154
0.001088	305.7722
0.001113	336.3495
0.001162	360.3744
0.001236	376.7551
0.001335	364.7426
0.00136	351.6381
0.00136	338.5335
0.001434	329.7972
0.001508	356.0062
0.001533	380.0312
0.001558	410.6084
0.001558	424.805

0.001607	444.4618
0.001706	459.7504
0.001756	490.3276
0.00178	520.9048
0.00183	544.9298
0.001879	526.3651
0.001879	504.5242
0.001904	480.4992
0.001904	451.014
0.001954	409.5164
0.001954	374.571
0.001978	352.7301
0.002052	335.2574
0.002102	351.6381
0.002176	366.9267
0.002226	385.4914
0.002275	406.2402
0.002324	443.3697
0.002324	469.5788
0.002349	490.3276
0.002399	506.7083
0.002498	490.3276
0.002547	473.947
0.002621	459.7504
0.002646	446.6459
0.00272	482.6833
0.00277	515.4446
0.002819	526.3651
0.002918	504.5242
0.002943	483.7754
0.002992	456.4743
0.003042	426.9891
0.003066	404.0562
0.003066	386.5835
0.00314	372.3869
0.003215	394.2278
0.003215	418.2527
0.003264	448.83
0.003289	482.6833
0.003338	501.248
0.003388	512.1685

0.003412	492.5117
0.003536	470.6708
0.003586	448.83
0.00366	433.5413
0.003734	445.5538
0.003783	465.2106
0.003833	481.5913
0.003882	501.248
0.003956	481.5913
0.003981	457.5663
0.004006	444.4618
0.004055	423.7129
0.00408	406.2402
0.004179	388.7676
0.004278	399.688
0.004352	416.0686
0.004402	434.6334
0.004451	446.6459
0.0045	454.2902
0.004599	433.5413
0.004698	418.2527
0.004773	422.6209
0.004896	407.3323
0.005094	377.8471
0.005267	363.6505
0.005465	382.2153
0.005663	389.8596
0.005811	365.8346
0.005885	346.1778
0.005984	325.429
0.006133	301.4041
0.006281	312.3245
0.006405	306.8643
0.006726	319.9688
0.007097	283.9314
0.00727	277.3791
0.007418	267.5507
0.007517	262.0905
0.007715	270.8268
0.007987	256.6303
0.008111	246.8019

0.008234	239.1576
0.008457	220.5928
0.00863	224.961
0.00905	187.8315
0.009174	187.8315
0.009496	165.9906
0.009644	168.1747
0.00999	143.0577
0.010213	143.0577
0.01046	132.1373
0.010781	128.8612
0.011004	121.2168
0.011449	109.2044
0.011894	102.6521
0.012537	90.63963
0.013131	82.99532
0.013823	69.8908
0.01412	63.33853
0.014466	64.43058
0.014837	57.87832
0.015504	54.60218
0.016222	44.77379
0.016469	48.04992
0.01684	39.31357
0.017582	37.12949
0.017977	30.57722
0.01815	34.9454
0.018793	31.66927
0.019659	26.20905
0.019955	28.39314
0.020425	24.02496
0.021365	22.93292
0.022156	25.117
0.023046	22.93292
0.023368	25.117
0.023714	19.65679
0.024505	20.74883